Universidade de Brasília
Instituto de Geociências
Programa de Pós-graduação em Geologia

Caracterização e evolução metalogenética das mineralizações auríferas nos prospectos Rosa de Maio, Bandeirantes e Maués, Província Mineral do Tapajós, sudeste do estado do Amazonas

Characterization and metallogenetic evolution of gold mineralization in the Rosa de Maio, Bandeirantes, and Maués prospects, Tapajós Mineral Province, southeastern Amazonas State

PEDRO VICTOR FREIRE DE SOUZA ALVES

TESE DE DOUTORADO Nº 220

Orientador: Prof. Dr. Nilson Francisquini Botelho

Brasília, 18 de julho de 2025

Universidade de Brasília
Instituto de Geociências
Programa de Pós-graduação em Geologia

Caracterização e evolução metalogenética das mineralizações auríferas nos prospectos Rosa de Maio, Bandeirantes e Maués, Província Mineral do Tapajós, sudeste do estado do Amazonas

Characterization and metallogenetic evolution of gold mineralization in the Rosa de Maio, Bandeirantes, and Maués prospects, Tapajós Mineral Province, southeastern Amazonas State

PEDRO VICTOR FREIRE DE SOUZA ALVES

Tese apresentada ao Programa de Pós-Graduação em Geologia – Instituto de Geociências – IG da Universidade de Brasília – UnB como requisito parcial obrigatório para a obtenção do título de Doutor em Geologia.

Área de concentração: Prospecção e Geologia Econômica

Orientador: Prof. Dr. Nilson Francisquini Botelho

Comissão Examinadora:

Prof. Dr. Claudinei Gouveia de Oliveira (IG/UnB)

Prof. Dr. Caetano Juliani (IGC/USP)

Prof. Dr. José Carlos Frantz (IG/UFRGS)

Profa. Dra. Catarina Labouré Bemfica Toledo (Suplente IG/UnB)

Ficha catalográfica elaborada automaticamente,
com os dados fornecidos pelo autor

Freire de Souza Alves, Pedro Victor
FA474c Caracterização e evolução metalogenética das mineralizações auríferas nos prospectos Rosa de Maio, Bandeirantes e Maués, Província Mineral do Tapajós, sudeste do estado do Amazonas / Pedro Victor Freire de Souza Alves; orientador Nilson Francisquini Botelho. Brasília, 2025.
146 p.

Tese(Doutorado em Geologia) Universidade de Brasília, 2025.

1. Cráton Amazônico. 2. Província Mineral do Tapajós. 3. Petrogênese de granitos. 4. Depósito aurífero hospedado em granito. 5. Depósito aurífero magmático-hidrotermal. I. Francisquini Botelho, Nilson, orient. II. Título.

AGRADECIMENTOS

Agradeço aos meus pais e irmãos por todo suporte e incentivo para terminar esta tese. Agradeço também a todos os amigos que, há um tempo, me ouvem com paciência dizer que vou acabar este doutorado. Agradeço ainda mais ao Caio por todo amor, companheirismo diário e apoio incondicional que me fizeram terminar este projeto. Agradeço ao professor Nilson pela orientação e aprendizado nesses longos anos de UnB. Agradeço a todos os amigos de mestrado e doutorado pelos bons momentos compartilhados, principalmente à Isabela, pelas discussões das mais variadas no Laboratório de Microssonda, além das festas que, nem sempre, precisavam de um motivo.

O presente trabalho foi realizado com apoio da Coordenação de Aperfeiçoamento de Pessoal de Nível Superior-Brasil (CAPES) – Código de Financiamento 001.

RESUMO

A Província Mineral do Tapajós (PMT) hospeda diversos depósitos de Au(-Cu-Mo) na porção centro-sul do Cráton Amazônico (norte do Brasil), alguns dos quais são reconhecidos como parte de sistemas do tipo pórfiro-epitermal, associados tanto ao magmatismo de arco da sequência magmática mais antiga (*older magmatic sequence*, 2,0–1,95 Ga) quanto ao magmatismo pós-colisional a anorogênico da sequência magmática mais jovem (*younger magmatic sequence*, 1,90–1,86 Ga), que inclui a Suíte Parauari (PAR, 1,89–1,87 Ga). Os depósitos auríferos Rosa de Maio, Bandeirantes e Maués, que são associados à PAR, possuem evolução magmático-hidrotermal e fertilidade em ouro ainda pouco estudadas. Neste estudo, investigamos esse magmatismo fértil e apresentamos novos dados de litogeoquímica, química mineral, espectroscopia Mössbauer em biotita, geocronologia U-Pb em zircão e monazita, geocronologia Ar-Ar em muscovita, além de dados isotópicos de Sm-Nd e enxofre de minérios e rochas hospedeiras. Cristalização fracionada teve papel fundamental na evolução magmática das rochas hospedeiras, que se diferenciaram de magmas parentais tonalíticos/granodioríticos para magmas monzo-/sienograníticos com biotita e sienograníticos/álcali-feldspato graníticos com muscovita. As razões Fe^{3+}/Fe^{2+} estimadas por espectroscopia Mössbauer em biotita magmática indicam condições de fugacidade de oxigênio acima do buffer NNO. A intrusão dos plútons Bandeirantes e Rosa de Maio se deu por volta de 1907 Ma e 1890 Ma, respectivamente, em um contexto tardi- a pós-colisional, após um período de magmatismo de arco controlado por subducção. Dados isotópicos de neodímio revelam que as fontes do Granito Rosa de Maio (GRM) envolvem contribuições tanto de material juvenil quanto de rochas crustais do embasamento. Saturação magmática em sulfetos, um possível fator controlando as baixas razões Cu/Au, pode ter sido um controle de primeira ordem sobre a fertilidade aurífera do GRM. Foram reconhecidos dois sistemas hidrotermais distintos no depósito Rosa de Maio: um sistema mais profundo e outro mais raso, formado próximo à superfície. A evolução hidrotermal do sistema mais profundo é caracterizada por uma sequência de quatro alterações: alteração sódica, potássica, propilítica e sericítica. Esse sistema hidrotermal iniciou-se com a exsolução de fluidos aquosos alcalinos de alta temperatura durante os estágios

finais da evolução magmática nas zonas apicais do GRM. Esses fluidos desencadearam um metasomatismo sódico pervasivo, seguido por metasomatismo potássico no biotita granito hospedeiro. A alteração propilítica subsequente sobrepôs-se às alterações anteriores em zonas proximais do centro da intrusão, marcando o início da precipitação de sulfetos (pirrotita ± calcopirita) a partir de fluidos hidrotermais mais frios (~370–170 °C). Esse estágio foi seguido por alteração sericítica fissural a pervasiva, caracterizada por pirita, quartzo e sericita, formados também a partir de fluidos de baixa temperatura (~325–160 °C). As zonas de alteração sericítica são caracterizadas pela abundante precipitação de sulfetos, incluindo pirita, calcopirita e galena, além de bismuto nativo subordinado. O sistema hidrotermal mais raso, geneticamente relacionado ao mais profundo, é caracterizado por alteração sericítica e silicificação, que por sua vez está associada ao desenvolvimento de um sistema *stockwork* composto por veios de quartzo e quartzo-pirita nas porções superiores e distais do centro da intrusão. A mineralização aurífera apresenta forte associação espacial com sulfetos, predominantemente pirita, e é caracterizada por baixos teores de Cu/Au. Ela ocorre em ambos os sistemas, hospedada nas zonas de alteração sericítica e em veios de quartzo ricos em sulfetos, presentes tanto como *infill* em veios quanto disseminados nas rochas encaixantes alteradas. Muscovita de um veio de quartzo do sistema mais raso forneceu uma idade de *plateau* $^{40}Ar/^{39}Ar$ de 1808,3 ± 7,1 Ma, interpretada como resultado de reequilíbrio isotópico durante um evento térmico mais jovem ou como evidência de um magmatismo mineralizante posterior ainda não identificado na área. As análises isotópicas de enxofre em pirita de ambos os sistemas forneceram valores de $\delta^{34}S$ entre +0,5 e +1,3‰, consistentes com uma fonte de enxofre predominantemente magmática. O sistema hidrotermal mais profundo do depósito Rosa de Maio compartilha diversas similaridades com depósitos do tipo pórfiro ricos em Au, enquanto o sistema mais raso provavelmente representa uma mineralização epitermal superposta, já em grande parte erodida.

Palavras-chave: Cráton Amazônico; Província Mineral Tapajós; Petrogênese de granitos; Orosiriano; Depósito aurífero hospedado em granito

ABSTRACT

The Tapajós Mineral Province (TMP) hosts multiple Au(-Cu-Mo) deposits in the southern-central Amazonian Craton (northern Brazil), some recognized as part of porphyry-epithermal systems, associated with either the arc magmatism of the older magmatic sequence (2.0-1.95 Ga) or the post-collisional to early-anorogenic magmatism of the younger magmatic sequence (1.90-1.86 Ga), which includes the Parauari Suite (PAR, 1.89-1.87 Ga). The Rosa de Maio, Bandeirantes, and Maués are gold deposits associated with the PAR, whose magmatic-hydrothermal evolution and Au fertility remain poorly constrained. In this study, we investigate this fertile magmatism and present new lithogeochemistry, mineral chemistry, Mössbauer spectroscopy on biotite, zircon and monazite U-Pb dating, muscovite Ar-Ar dating, as well as Sm-Nd and sulfur isotope data of both the ore and host rocks. Fractional crystallization played a major role in the magmatic evolution of host rocks, differentiating from tonalitic/granodioritic parental magmas to biotite monzo-/syenogranitic and muscovite syeno-/alkali feldspar granitic magmas. Ferric/ferrous iron ratios estimated by Mössbauer spectroscopy on magmatic biotite indicate oxygen fugacity conditions above the NNO buffer. The Bandeirantes intrusion and the Rosa de Maio Granite (RMG) were emplaced at ca. 1907 Ma and 1890 Ma, respectively, in a late- to post-collisional setting, following a period of subduction-controlled arc magmatism. Neodymium isotope data reveal that the sources of the RMG involve contributions from both juvenile material and crustal rocks from the basement. Magmatic sulfide saturation, a potential factor controlling low Cu/Au ratios, may have been a first-order control on the Au fertility of the RMG. Two distinct hydrothermal systems are recognized in the Rosa de Maio deposit: a deeper system and a shallower, near-surface system. The hydrothermal evolution of the deeper system is characterized by a sequence of four alteration types: sodic, potassic, propylitic, and sericitic alteration. Hydrothermal activity initiated with the exsolution of high-temperature, alkaline aqueous fluids during the late stages of magmatic evolution in the apical zones of the RMG. These fluids promoted pervasive Na metasomatism, followed by K metasomatism of the host biotite granite. Propylitic alteration subsequently overprinted previously formed hydrothermal assemblages in proximal zones of the intrusion center,

marking the onset of sulfide precipitation (pyrrhotite ± chalcopyrite) from cooler hydrothermal fluids (~370-170 °C). This stage was followed by fissural to pervasive sericitic alteration, characterized by pyrite, quartz, and sericite formed from similarly low-temperature fluids (~325-160 °C). Sericitic alteration zones are marked by abundant sulfide precipitation, including pyrite, chalcopyrite, and galena, as well as minor native bismuth. The shallower hydrothermal system, genetically linked to the deeper one, is characterized by sericitic alteration and silicification, associated with the development of a stockwork system composed of quartz and pyrite-quartz veins in the upper, distal portions of the intrusion center. Gold mineralization shows a strong spatial association with sulfides, predominantly pyrite, and is characterized by low Cu/Au ratios. It occurs in both systems within sericitic alteration zones and sulfide-rich quartz veins, present both as vein infill and disseminated in altered wallrock. Muscovite from a quartz vein in the shallower system yielded a $^{40}Ar/^{39}Ar$ plateau age of 1808.3 ± 7.1 Ma, interpreted either as the result of isotopic resetting during a younger thermal event or as evidence of a younger mineralizing magmatism not yet identified in the area. Sulfur isotope analyses of pyrite from both systems yielded $\delta^{34}S$ values between +0.5 and +1.3‰, consistent with a dominantly magmatic sulfur source. Overall, the deeper system of the Rosa de Maio deposit shares several similarities with Au-rich porphyry-style deposits, whereas the shallower system likely represents a superimposed epithermal mineralization, now largely eroded.

Keywords: Amazonian Craton; Tapajós Mineral Province; Granite petrogenesis; Orosirian; Granite-hosted gold deposit

LISTA DE FIGURAS

LISTA DE TABELAS

SUMÁRIO

CAPÍTULO 1
INTRODUÇÃO

1 INTRODUÇÃO

A produção de ouro por garimpeiros na Província Mineral do Tapajós (PMT) e, mais especificamente, na bacia do rio Tapajós, remonta aos anos 1950. Antes disso, desde a descoberta da foz do rio Amazonas por Vicente Yáñez Pinzón em 1500 até o fim do Ciclo da Borracha em 1912 com uma breve ressurgência entre 1942-1945, não houve nessa região atividade garimpeira significativa documentada. Durante esse período houveram expedições espanholas por toda a extensão do rio Amazonas, a passagem do bandeirante Antônio Raposo Tavares e o estabelecimento de missionários ao longo de rios importantes do Amazonas. Nada disso, no entanto, consolidou uma cultura mineira na região. Foi somente a partir dos anos 1950 que se iniciou a extração de ouro aluvionar no Rio das Tropas, com posterior abertura de pistas de pouso em 1962 (Rodrigues et al., 1994). Entre 1958-1979, a PMT produziu cerca de 23 toneladas de ouro por meios rudimentares, praticamente utilizando pá e picareta (Araújo Neto 1996, Rodrigues et al., 1994). Durante a década de 1980, já com a abertura da rodovia Transamazônica desde 1972, a extração passou a utilizar motobombas de alta pressão e até mesmo dragas rudimentares (Rodrigues et al., 1994), elevando a produção entre os anos 1980-1996 para quase 200 toneladas (Araújo Neto 1996). Durante o período de 1958-1971, a PMT representou aproximadamente 54% da produção de ouro nacional. No período seguinte, até o final dos anos 1980, a produção com relação ao total nacional teve várias oscilações, com o auge em 1982 (40% da produção total). Já nos anos seguintes, durante a década de 1990, houve um declínio na produtividade da PMT, atingindo valores próximos de 20% em relação à média nacional (Faraco et al., 1997).

Os primeiros trabalhos de reconhecimento geológico da Província Mineral do Tapajós foram realizados no final dos anos 1950 (e.g., Almeida e Nogueira Filho, 1959). Durante os anos 1960, foram publicados os primeiros trabalhos de mapeamento geológico em escala 1.500.000 na região do rio Tapajós pelo Departamento Nacional de Produção Mineral (DNPM). Já na década de 1970, através do Projeto RADAM (Santos et al., 1975), a cartografia geológica foi detalhada na escala de 1.250.000, abrangendo as bacias dos rios Tapajós, Maués e Jamanxim. No início da década de 1980, a cartografia geológica é ainda

mais refinada (na escala de 1.100.000) através de levantamento realizado pela Companhia de Pesquisa de Recursos Minerais (CPRM) e o DNPM (Bizinella et al., 1980). A partir de 1995, foi implementado o Projeto PROMIN-Tapajós pela CPRM. Esse projeto tinha o objetivo de elaborar mapas geológicos regionais, estudar os controles geológicos da mineralização de ouro e avaliar os possíveis impactos ambientais em uma área piloto (vila do Creporizão), culminando na publicação do livro "Geologia e Recursos Minerais da Província Mineral do Tapajós" (Klein et al., 2001). Em 2008, com o objetivo de apresentar uma visão integrada das mineralizações auríferas na PMT, a CPRM publicou o livro "Província Mineral do Tapajós: Geologia, Metalogenia e Mapa Previsional para Ouro em SIG" (Coutinho et al., 2008).

1.1 Justificativa e objetivo

Desde o início dos anos 2000 até hoje, as universidades realizaram estudos metalogenéticos em escala local, geralmente em garimpos, que resultaram na publicação de diversos artigos científicos em periódicos internacionais. Os prospectos Rosa de Maio, Bandeirantes e Maués, por outro lado, nunca foram estudados nesse nível de detalhe. Por esse motivo, esta tese de doutorado tem a intenção de investigar as condições geológicas responsáveis pela formação do ouro, como, por exemplo, entender o magmatismo relacionado à mineralização, a evolução hidrotermal e o evento mineralizador, a idade da mineralização e, finalmente, propor um modelo metalogenético.

1.2 Localização e acesso

Os prospectos Rosa de Maio, Bandeirantes e Maués estão localizados em plena Floresta Amazônica, no sudeste do estado do Amazonas, no município de Maués (Fig. 1). A região que os abrange está a 360 km de Manaus e 1.575 km de Brasília. As cidades mais próximas estão no estado do Pará, a sudeste e nordeste, respectivamente: Jacareacanga (67 km) e Itaituba (275 km). Os prospectos distam um do outro, em média, 20 km (Fig. 1). Outro prospecto importante na região é o Doze de Outubro, que está mais distante, a 48 km nordeste do prospecto Rosa de Maio. A rodovia mais próxima é a BR-230 (Rodovia Transamazônica) que, ainda assim, não dá acesso aos prospectos. O principal meio de acessar essas áreas é por via aérea, através de aviões de

pequeno porte, muito comuns na região. O embarque nesses aviões pode ser feito a partir das cidades de Manaus-AM e Itaituba-PA. Tomando como ponto de partida o Distrito Federal, um dos caminhos possíveis até a cidade de Itaituba se dá pela BR-080 até Uruaçu-GO, seguindo-se pela BR-153 (Rodovia Belém-Brasília) até Darcinópolis-TO e, finalmente, pela BR-134 até a BR-230 em Luzinópolis-TO. A partir de então, segue-se para oeste na rodovia BR-230 (Rodovia Transamazônica) até Itaituba-PA.

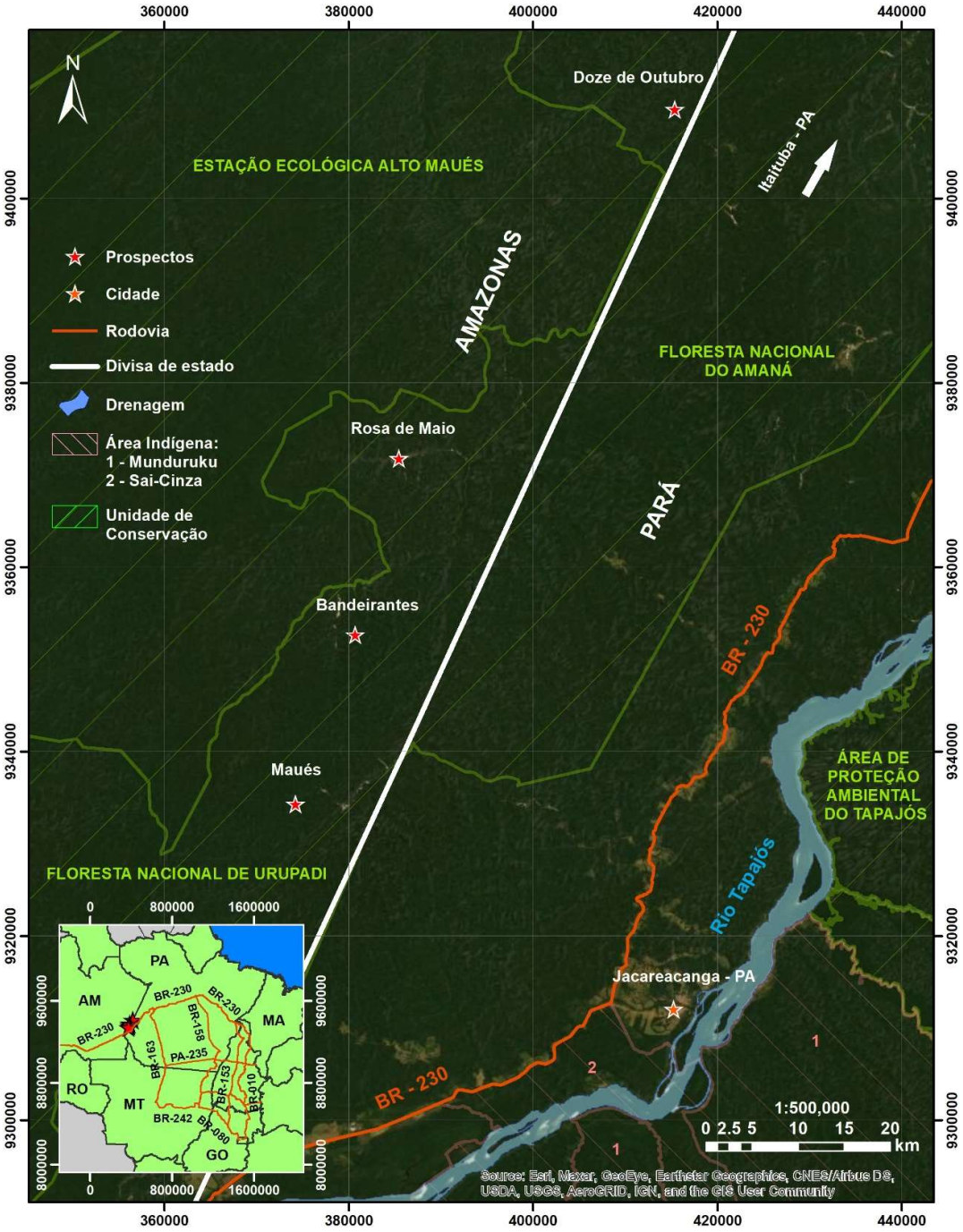

Figura 1 – Mapa de localização das áreas estudadas no sudeste do estado do Amazonas, indicando os prospectos Rosa de Maio, Bandeirantes e Maués, além de outro prospecto relevante na região, o Doze de Outubro.

CAPÍTULO 2
CONTEXTO GEOLÓGICO REGIONAL

2 CONTEXTO GEOLÓGICO REGIONAL

O Cráton Amazônico é uma das principais unidades geotectônicas no contexto da Plataforma Sul-Americana. Também representa uma das maiores áreas cratônicas do mundo, com aproximadamente 4,6 x 10^6 km^2 (Cordani, 2017). Está localizado no norte da América do Sul, com sua maior extensão no território brasileiro. É limitado a oeste pelos Andes, a leste pelo Cinturão Araguaia, a sudeste pelo Cinturão Paraguai e a sul pelo Cinturão Tucavaca (na Bolívia, Tassinari e Macambira, 2004). Além disso, é coberto por bacias fanerozoicas, se destacando a Bacia do Amazonas (paleozoica) na região central. O cráton iniciou sua história tectono-geológica no Mesoarqueano (rochas mais antigas datam de 3,05 Ga) e tornou-se tectonicamente estável em 1,0 Ga. Do ponto de vista metalogenético, o cráton é de grande importância, visto que nele estão hospedados depósitos das províncias auríferas Tapajós e Alta Floresta, além de depósitos polimetálicos da Província Mineral de Carajás, incluindo depósitos IOCG de classe mundial.

A Província Mineral do Tapajós (PMT), também conhecida como Província Aurífera do Tapajós, é uma província metalogenética composta principalmente por depósitos de Au(-Cu) na porção sul do Cráton Amazônico, no norte do Brasil (Fig. 2). Esses depósitos são hospedados por rochas vulcânicas e subvulcânicas paleoproterozoicas que fazem parte das províncias geocronológicas Amazônica Central e Ventuari-Tapajós, propostas por Tassinari e Macambira (1999), ou das províncias Amazônica Central e Tapajós-Parima, propostas por Santos et al. (2000). Segundo Santos et al. (2000, 2004), a Província Tapajós-Parima é um orógeno colisional orosiriano formado pela sutura de múltiplos arcos magmáticos com uma crosta continental arqueana-paleoproterozoica mais antiga, culminando em um segmento crustal lateralmente contínuo de direção NO-SE. Nesse modelo tectônico, o magmatismo granítico foi gerado em duas orogenias e evoluiu de magmatismo primitivo de arco de ilha para arco continental evoluído e magmatismo pós-orogênico. Carneiro et al. (2018) revisaram esse modelo e propuseram uma nova evolução tectônica. Com base em dados magnéticos, interpretam estruturas profundas de direção E-O sob a PMT (cerca de 15 km) como evidência da continuidade para oeste da Província Carajás. As estruturas NNO-SSE na superfície são consideradas resultado de regimes tectônicos mais

rasos. Nessa nova evolução, a PMT seria um orógeno acrecionário continental (semelhante à Cordilheira dos Andes) desenvolvido sobre um embasamento arqueano, e não uma amalgamação de múltiplos arcos magmáticos (por exemplo, Alves et al., 2020).

As suítes ígneas associadas à PMT são agrupadas na sequência magmática mais antiga (*older magmatic sequence,* OMS, 2,0–1,95 Ga) e na sequência magmática mais jovem (*younger magmatic sequence,* YMS, 1,90–1,86 Ga), sendo separadas por um hiato de aproximadamente 50 milhões de anos (Tabela 1, Cassini et al., 2020; Cassini et al., 2022). No modelo tectônico de Santos et al. (2004), a OMS e a YMS correspondem às unidades agrupadas nas orogenias Mundurucus e Tropas, respectivamente (Tabela 1). A OMS inclui o Grupo Jacareacanga (2,2–2,0 Ga, rochas metavulcânicas e metassedimentares de baixo grau), o Complexo Cuiú-Cuiú (2,04–1,99 Ga, tonalito e granodiorito), a Formação Vila Riozinho (2,0 Ga, andesito basáltico, traquito e riolito), o Suíte Jamanxim (2,0–1,98 Ga, monzogranito) e a Suíte Creporizão (1,99–1,95 Ga, rochas graníticas calco-alcalinas de alto K) (Santos et al., 2000, 2001, 2004; Lamarão et al., 2002). Segundo Santos et al. (2004), essas unidades ígneas representam a evolução do magmatismo de arco na transição de arco de ilha para arco continental do tipo andino (ver Tabela 1). Cassini et al. (2020) as interpretam como um estágio de arco magmático dominado por magmas anidros com forte componente crustal em ca. 2,0 Ga, seguido por magmatismo de arco entre 1,98–1,95 Ga com mínima contaminação crustal, formando magmas metaluminosos a levemente peraluminosos, hidratados e oxidados.

A YMS compreende a Suíte Tropas (1,90–1,88 Ga, tonalito e granodiorito), a Suíte Parauari (1,89–1,87 Ga, tonalito, granodiorito, monzo- e sienogranito) e o Grupo Iriri (1,89–1,87 Ga, rochas vulcânicas intermediárias a ácidas da série de alto K a shoshonítica; Santos et al., 2000, 2001, 2004). Esse grupo consiste nas formações Bom Jardim (1,89–1,88 Ga, andesito basáltico, andesito, traquito e ignimbritos), Salustiano (1,88–1,87 Ga, dacito, riodacito, riolito), Aruri (1,88–1,87 Ga, tufos ácidos, brechas vulcânicas e ignimbritos dacíticos) e Moraes Almeida (1,89–1,87 Ga, riolito, traquito e ignimbritos) (Santos et al., 2000, 2001, 2004; Lamarão et al., 2002; Tabela 1). Essas unidades

representam o magmatismo e vulcanismo de arco continental em um arco maduro do tipo andino a um ambiente pós-orogênico, após 50 milhões de anos de quiescência após a OMS (Dall'Agnol et al., 1999; Santos et al., 2000, 2001, 2004; Lamarão et al., 2002; Juliani et al., 2005; Cassini et al., 2020, 2022). A Suíte Maloquinha (1,87–1,86 Ga, sienogranito e granito de feldspato alcalino da série de alto K a shoshonítica; Santos et al., 2000, 2004) representa o último estágio do magmatismo granítico dentro da YMS em um ambiente pós-orogênico e início de anorogênico (Santos et al., 2000, 2001, 2004; Lamarão et al., 2002; Cassini et al., 2020, 2022). Um resumo dos principais tipos litológicos, ambientes geotectônicos correspondentes e depósitos minerais associados a essas unidades litoestratigráficas é apresentado na Tabela 1.

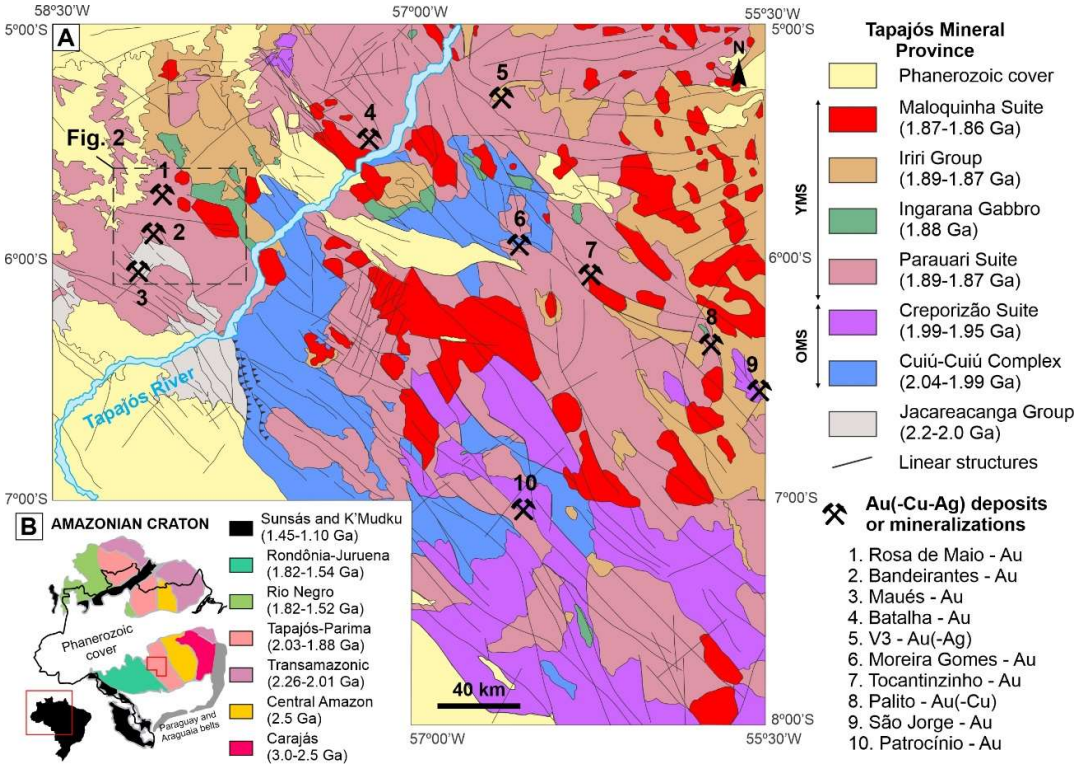

Figura 2 – A) Mapa geológico simplificado da Província Mineral do Tapajós (PMT) mostrando alguns dos principais depósitos de Au(-Cu-Ag). B) Localização da PMT dentro do Cráton Amazônico. Subdivisões tectônicas do cráton segundo Santos et al. (2000, 2006). Modificado de Klein et al. (2001). OMS = Sequência magmática mais antiga; YMS = Sequência magmática mais jovem.

A Suíte Parauari (PAR) possui vasta extensão na Província Mineral do Tapajós (PMT) (Fig. 2) e é composta por monzogranitos e sienogranitos com biotita e/ou hornblenda, com gabros subordinados (Santos et al., 2004). Essas rochas intrudiram o Complexo Cuiú-Cuiú e a Suíte Creporizão (Santos et al.,

2000, 2004). A PAR recebe esse nome devido à localização do Granito Rosa de Maio, mineralizado em ouro, na bacia do rio Parauari (Santos et al., 2000; Santos et al., 2004), que faz parte da bacia amazônica mais ampla. Grãos de zircão de um monzogranito do batólito Rosa de Maio foram datados por Santos et al. (2000) e produziram uma idade discordante de U-Pb TIMS com intercepto superior em 1879 ± 11 Ma, enquanto Santos et al. (2004) obtiveram uma idade concordante de U-Pb TIMS de 1879 ± 3 Ma da mesma amostra. Ambas as idades são interpretadas como idades de cristalização. Dados isotópicos de Sm-Nd obtidos por Santos et al. (2000) para a PAR apresentaram valores de εNd (1,89 Ga) entre -0,87 e +1,83 com idades modelo TDM em torno de 2,1 Ga, enquanto Echeverri Misas (2015) obteve valores de εNd (1,88 Ga) entre -3,2 e +0,3 com idades modelo TDM de 2,1 a 2,4 Ga para as rochas da PAR que hospedam o depósito de Au(-Cu) Palito no sul do Domínio Tapajós. O Gabro Ingarana (1881 ± 3 Ma; Santos et al., 2004) é composto por gabros cálcio-alcalinos de augita, os quais foram incluídos na evolução magmática da PAR por Santos et al. (2004). Sua composição máfica e intrusão contemporânea com a PAR levaram esses autores a interpretar a suíte como bimodal. Segundo o modelo tectônico de Santos et al. (2004), a PAR representa um terceiro arco continental formado após a fase de arco de ilha (Suíte Tropas, 1,90–1,88 Ga) da Orogênese Tropas no contexto da Orogênese Tapajós-Parima (2,0–1,87 Ga). Em um modelo recente proposto por Cassini et al. (2020), a PAR representa um magmatismo granítico cálcio-alcalino de alto K a shoshonítico, metaluminoso a fracamente peraluminoso, gerado por fusão parcial de cunha mantélica progressivamente metasomatizada acima de uma zona de subducção de longa duração em um orógeno de acreção continental. Nesse modelo, o magmatismo da PAR ocorreu em um contexto tardi- a pós-orogênico e marca o início da sequência magmática mais jovem (YMS).

Cassini et al. (2020, 2022) consideraram o magmatismo da PAR potencialmente fértil para a formação de depósitos magmático-hidrotermais ricos em ouro. Esses autores propuseram que a geração desse magmatismo de arco evoluído, impulsionado por fusão parcial de um manto litosférico subcontinental metasomatizado, pode ter desestabilizado sulfetos residuais ricos em ouro previamente formados no manto. Além disso, sugeriram que o magmatismo da

PAR pode ter remobilizado mineralizações auríferas mais antigas associadas à sequência magmática mais antiga (OMS). Alguns exemplos de depósitos magmático-hidrotermais ricos em ouro associados ao magmatismo granítico contemporâneo ao da PAR são os depósitos Batalha (Juliani et al., 2002), Palito (Echeverri Misas, 2010, 2015) e São Jorge (Lamarão et al., 2002) (ver também Juliani et al., 2021; Cassini et al., 2022).

Tabela 1 – Resumo das principais unidades litoestratigráficas da PMT. Modificado de Cassini et al. (2020, 2022).

	Tectonic subdivision	Lithostratigraphic unit		Description	Geotectonic context	Deposit/Mineral occurrence
Tapajós Mineral Province - TMP (closely correlates with the Tapajós-Parima Orogen[3])	Younger magmatic sequence (YMS)[6] or Tropas Orogeny[3]	Maloquinha Suite (1.87-1.86 Ga)[2, 3, 4]		Shoshonitic syeno- to alkali feldspar granite	Post-orogenic[1, 2, 3], Post-orogenic to early-anorogenic[6]	
		Iriri Group (1.89-1.87 Ga)[2, 3, 5]	Moraes Almeida	High-K calc-alkaline to shoshonitic intermediate to acidic volcanic rocks	Multiple interpretations including magmatic arc and post-orogenic to early-anorogenic[1, 2, 3, 4, 5, 6]	V3 (Au)[13]
			Aruri			
			Salustiano			
			Bom Jardim			
		Parauari Suite (1.89-1.87 Ga)[2, 3, 6]		High-K calc-alkaline to shoshonitic tonalitic to syenogranitic rocks	Magmatic arc[2, 3], Late- to post-orogenic[6]	Rosa de Maio (Au), Bandeirantes (Au), Batalha (Au)[12], Palito (Au-Cu)[13], São Jorge (Au)[4, 14]
		Tropas Suite (1.90-1.88 Ga)[2, 3]		Tonalite and granodiorite	Island arc[2, 3]	
	Older magmatic sequence (OMS)[6] or Mundurucus Orogeny[3]	Creporizão Suite (1.99-1.95 Ga)[2, 3, 6]		High-K calc-alkaline to shoshonitic tonalitic to syenogranitic rocks	Magmatic arc[2, 3, 6]	Tocantinzinho (Au)[7, 8, 9], Patrocínio (Au)[10], Moreira Gomes (Au)[11]
		Jamanxim Suite (2.0-1.98 Ga)[3]		Monzogranite		
		Vila Riozinho Formation (2.0 Ga)[4]		Calc-alkaline to shoshonitic intermediate to acidic volcanic rocks	Magmatic arc[4]	Coringa (Au-Ag)[15]
		Cuiú-Cuiú Complex (2.04-1.99 Ga)[1, 2, 3]		Calc-alkaline tonalite, diorite, granodiorite	Island arc[1, 2, 3], Magmatic arc[6]	
		Jacareacanga Group (2.2-2.0 Ga)[1, 2, 3]		Metavolcanic and metasedimentary rocks	Back-arc and trench sedimentation[1, 2, 3]	

Referências: 1 - Santos et al. (2000), 2 - Santos et al. (2001), 3 - Santos et al. (2004), 4 - Lamarão et al. (2002), 5 - Juliani et al. (2005), 6 - Cassini et al. (2020), 7 – Borgo et al. (2017), 8 – Biondi et al. (2018), 9 – Lopes and Moura (2019), 10 – Cassini (2016), 11 - Assunção and Klein (2014), 12 - Juliani et al. (2002), 13 - Echeverri Misas (2015), 14 – Borges et al. (2009) e 15 – Guimarães et al. (2021).

O depósito de ouro Batalha (Fig. 2; Juliani et al., 2002) é hospedado pela intrusão granítica homônima (1883 ± 4 Ma, Juliani et al., 2002), que consiste em

sieno- a monzogranitos metaluminosos a peraluminosos, cálcio-alcalinos de alto K, com hornblenda e/ou biotita, e afinidade tardi- a pós-orogênica. Durante o estágio hidrotermal (500–290 °C e 2,6–1,2 kbar), essas rochas passaram por metasomatismo sódico pervasivo e fissural, além de alterações potássica, propilítica e sericítica. A mineralização aurífera está majoritariamente associada à alteração sericítica e ocorre com associações de quartzo, sericita, pirita, calcopirita e galena, tanto em stockworks quanto disseminada ao redor de veios hidrotermais (Juliani et al., 2002, 2021). Juliani et al. (2002) reconheceram características tanto de depósitos do tipo pórfiro quanto de sistemas *intrusion-related* (*intrusion-related gold systems*, IRGS) no depósito Batalha.

O depósito Palito de Au(-Cu) (Fig. 2; Echeverri-Misas, 2010, 2015) é hospedado pelo Granito Palito (1883 ± 11 Ma, Aquino, 2013), composto por monzogranito a álcali-feldspato granito com biotita, metaluminoso a peraluminoso e alcalino-cálcico de alto K. Essa intrusão, incluída na suíte PAR, também foi alojada em um contexto tardi- a pós-orogênico (Cassini et al., 2020, 2022). O depósito possui reservas provadas e prováveis estimadas em 717.000 t @ 11,74 g/t Au (Juliani et al., 2021 e referências ali citadas). Essas rochas graníticas foram afetadas por alterações potássica, propilítica, sericítica e argílica/argílica avançada. A mineralização de Au(-Cu) ocorre em veios sulfetados quartzo e veios de sulfetos semi-maciços, stockworks, brechas hidrotermais e sulfetos disseminados (Echeverri-Misas, 2010; Juliani et al., 2021). Com base em valores de $\delta^{34}S$ entre +1,2 e +3,6‰ para pirita e calcopirita, Echeverri-Misas (2010) propôs uma fonte magmática de enxofre para os sulfetos precipitados durante o estágio hidrotermal. Essas características magmáticas e hidrotermais são compatíveis com depósitos do tipo pórfiro Au(-Cu) (Echeverri-Misas, 2010, 2015; Juliani et al., 2021; Cassini et al., 2020, 2022).

O depósito de ouro São Jorge (Fig. 2; Lamarão et al., 2002; Borges et al., 2009) é hospedado por duas intrusões distintas: os granitos São Jorge mais antigo (1,98 Ga) e mais jovem (1,89 Ga) (Lamarão et al., 2002). O Granito São Jorge mais jovem (1891 ± 3 Ma, Lamarão et al., 2002), mais estreitamente associado à mineralização aurífera, é composto por monzogranitos com hornblenda-biotita, metaluminosos a peraluminosos e alcalino-cálcicos de alto K (Borges et al., 2009; Cassini et al., 2022). Essas rochas foram afetadas por

alterações potássica, propilítica e sericítica, com a mineralização aurífera predominantemente associada à alteração sericítica e ocorrendo em stockworks, veios quartzosos-sulfetados em enxames e minério disseminado. A paragênese sericítica inclui sericita, pirita, carbonatos, calcopirita, esfalerita e galena (Borges et al., 2009; Juliani et al., 2021). Borges et al. (2009) reconheceram o depósito São Jorge como um depósito do tipo pórfiro ou IRGS, enquanto Juliani et al. (2021) o interpretaram como um depósito aurífero hospedado em granito, controlado por estruturas.

CAPÍTULO 3
MÉTODOS ANALÍTICOS

3 MÉTODOS ANALÍTICOS

3.1 Litogeoquímica

A preparação das amostras foi realizada no Laboratório de Preparação de Amostras do Instituto de Geociências da Universidade de Brasília e envolveu desagregação manual, britagem, pulverização em moinho de anel e quarteamento. As análises de elementos maiores, menores e traço em rocha total de 64 amostras foram realizadas no ACME Analytical Laboratories Ltd. (Vancouver, Canadá). O procedimento analítico padrão consiste em misturar os pós de rocha com tetraborato de lítio e fundir a mistura para produzir pastilhas de vidro fundido. As pastilhas fundidas são analisadas por espectroscopia de fluorescência de raios-X (XRF) para os elementos maiores e por espectrometria de massas com plasma acoplado indutivamente (ICP-MS) para os elementos menores e traço. Informações adicionais sobre os procedimentos analíticos estão disponíveis em acmelab.com.

3.2 Química mineral

As composições químicas de biotita, epidoto, clorita, muscovita, pirita e pirrotita foram obtidas utilizando uma microssonda eletrônica JEOL JXA-8230 no Instituto de Geociências da Universidade de Brasília. As análises de Si, Ti, Al, Fe, Mn, Mg, Ca, Ba, Na, K, F e Cl foram realizadas em lâminas delgadas polidas (com 30 µm de espessura), com uma voltagem de aceleração de 15 kV, corrente de feixe de 10 nA e diâmetro do ponto de 1 µm em silicatos. Os tempos de leitura para todos os elementos foram de 10 segundos no pico e 5 segundos no fundo. A linha Kα de raios X foi utilizada para todos os elementos. Os padrões utilizados foram os seguintes materiais de referência: microclínio (Si, Al e K), andradita (Fe e Ca), barita (Ba), albita (Na), forsterita (Mg), topázio (F), vanadinita (Cl) e pirofanita (Ti e Mn). Os elementos As, Zn, Se, Ga, S, Sb, Cd, Pb, Bi, Te, Fe, Co, Ni, Cu, Mo, Pd, Ag, Pt, Au e Hg foram analisados a uma voltagem de aceleração de 20 kV e corrente do feixe de 20 nA também em pontos de 1 µm de diâmetro em sulfetos. A redução dos dados foi realizada utilizando o pacote de software da microssonda. Lâminas delgadas e seções polidas confeccionadas para microscopia ótica de luz transmitida e refletida foram utilizadas também em microssonda eletrônica para microscopia eletrônica de varredura (imagens *BSE*

– *back-scattered electrons*) e análise qualitativa e semi-quantitativa (EDS – *energy-dispersive X-ray spectroscopy)*.

3.3 Espectroscopia Mössbauer

As análises de espectroscopia Mössbauer em biotita foram realizadas no Laboratório de Espectroscopia Mössbauer do Instituto de Física da Universidade de Brasília. Os concentrados de biotita foram obtidos por meio de procedimentos padrão de separação mineral, incluindo britagem da rocha, moagem, peneiramento e separação magnética. Os espectros Mössbauer foram obtidos à temperatura ambiente utilizando um espectrômetro convencional de aceleração constante com uma fonte radioativa de ^{57}Co/Rh e um analisador multicanal integrado com contador proporcional como detector, em geometria de transmissão. A calibração foi realizada utilizando uma folha de ferro natural. Os valores de deslocamento isomérico foram calculados em relação ao Fe-α à temperatura ambiente. As análises dos espectros foram feitas utilizando um procedimento de ajuste por mínimos quadrados com o software Normos, assumindo formas de pico Lorentzianas. As estimativas das razões Fe^{3+}/Fe^{2+} na biotita foram determinadas combinando as análises por EPMA (ferro total como FeO) com os resultados da espectroscopia Mössbauer.

3.4 Geocronologia U-Pb

Os dados isotópicos U-Pb de zircão e monazita foram obtidos no Laboratório de Estudos Geodinâmicos, Geocronológicos e Ambientais da Universidade de Brasília. As massas de interesse foram medidas em um espectrômetro de massas de campo setorial de alta resolução Thermo Finningan Element XR, com coletor único, acoplado a um sistema de ablação a laser Excimer Iridia (ArF) de 193 nm. O sistema de ablação a laser é equipado com uma câmara de duplo volume Cobalt. O espectrômetro de massas foi ajustado para melhorar a sensibilidade para U e Pb, ao mesmo tempo minimizando a produção de óxidos antes de cada sessão analítica. Cada análise consistiu em 10 segundos de medição de fundo seguidos por 20 segundos de aquisição da amostra. Cada massa (202, 204, 206–208, 232, 238) foi medida utilizando o modo de detecção tripla (SEM+Faraday), por varredura do setor eletrostático em cada massa. Cada varredura teve duração de 82 ms, resultando em mais de 800

varreduras por ablação. As condições do laser incluíram um diâmetro do feixe de 25 μm, frequência de 20 Hz e energia de 2,0 $J.cm^{-2}$. Parâmetros completos de aquisição podem ser consultados no Anexo A.

Os dados brutos foram processados no Iolite 4.0 (Paton et al., 2011) como sinal em tempo resolvido, e a inspeção individual dos sinais foi realizada com auxílio do VizualAge (Petrus e Kamber, 2012). A correção dos dados incluiu subtração de branco, correção LIEF utilizando um modelo exponencial mais linear, e normalização pelo padrão de zircão GJ-1 (Jackson et al., 2004). Os seguintes materiais de referência foram usados para controle de qualidade: zircão 91500 (Wiedenbeck et al., 1995), zircão Plešovice (Sláma et al., 2008), monazita Itambé (Gonçalves et al., 2016) e monazita STK (Fisher et al., 2020). A variância excedente no padrão primário foi propagada para cada ponto analítico. Uma incerteza sistemática de aproximadamente 1% foi propagada para cada idade final. Nenhuma correção para chumbo comum foi aplicada. As idades são apresentadas com incerteza de 2σ. Diagramas de Wetherill foram gerados utilizando a versão online do IsoplotR (Vermeesch, 2018).

3.5 Geocronologia Ar-Ar

As análises geocronológicas $^{40}Ar/^{39}Ar$ de muscovita foram realizadas na Queen's Facility for Isotope Research (QFIR), Departamento de Ciências Geológicas e Engenharia Geológica, Queen's University, Canadá. Separações minerais de alta pureza e sem alterações foram obtidas por britagem, peneiramento e seleção manual sob microscópio binocular. Os grãos selecionados foram ainda purificados por limpeza ultrassônica em etanol por 20 minutos, seguida de lavagem com água deionizada. Para a irradiação, 10 mg da separação de muscovita foram envoltos em folha de alumínio e empilhados verticalmente em um recipiente de alumínio junto ao padrão de irradiação hornblenda Hb3gr (idade K-Ar = 1072 ± 11, 1σ; Roddick, 1983; Turner et al., 1971). As amostras foram submetidas à irradiação por nêutrons durante 40 horas no Reator Nuclear McMaster em Hamilton, Ontário, Canadá.

Após a irradiação, as análises de aquecimento por etapas $^{40}Ar/^{39}Ar$ foram realizadas utilizando um espectrômetro de massas para gases nobres MAP 216 com fonte de íons Baur-Signer e multiplicador de elétrons. Amostras e padrões

foram carregados em pequenas cavidades (2 mm de diâmetro, 1,5 mm de profundidade) perfuradas em um suporte de amostra de cobre, posicionados sob uma janela de safira em uma câmara de aço inoxidável passível de aquecimento. O parâmetro de irradiação (valor J) foi determinado por interpolação polinomial de segunda ordem. O aquecimento por etapas foi realizado com um laser de íons Ar Lexel 3500 de 8 W desfocado. Cada etapa de aquecimento durou aproximadamente três minutos, com as etapas finais envolvendo a fusão completa da amostra. Os gases liberados foram purificados utilizando esponja de titânio e getters de Zr-Al antes da análise.

As razões isotópicas de argônio foram normalizadas para uma razão atmosférica $^{40}Ar/^{36}Ar$, e as idades foram calculadas utilizando constantes convencionais de decaimento do ^{40}K (Renne et al., 2011). As análises isotópicas foram corrigidas para brancos do sistema, contaminação atmosférica e interferências induzidas por nêutrons (por exemplo, decaimento radioativo do ^{37}Ar e ^{39}Ar, e reações menores de Ca, Cl e K). Para avaliar possível excesso de argônio devido a alteração ou inclusões minerais, as razões Ca/K e Cl/K foram determinadas a partir das razões $^{37}Ar/^{39}Ar$ e $^{38}Ar/^{39}Ar$ usando valores derivados do monitor de fluxo Hb3gr. A precisão analítica para os passos individuais usados nos cálculos da idade de plateau foi de 0,5% ao nível de confiança de 2σ. As idades foram calculadas utilizando a versão online do IsoplotR (Vermeesch, 2018).

3.6 Geoquímica isotópica de Sm-Nd

As análises isotópicas de Sm e Nd em pó de rocha total foram realizadas por espectroscopia de massa por ionização térmica (TIMS) no Laboratório de Estudos Geodinâmicos, Geocronológicos e Ambientais da Universidade de Brasília, seguindo os procedimentos analíticos descritos por Gioia e Pimentel (2000). Foi utilizado um espectrômetro Finnigan TRITON com sete coletores em modo estático. Soluções spike de ^{149}Sm e ^{150}Nd foram adicionadas às amostras de pó de rocha total. A separação de Sm de Nd foi realizada usando colunas de troca catiônica, seguida de evaporação com duas gotas de 0,025 NH_3PO_4. O resíduo foi então dissolvido em 1 µl de HNO_3 destilado a 5% e carregado em um conjunto de filamentos duplos de Re. O padrão internacional de rocha BHVO-2

foi utilizado, juntamente com uma constante de decaimento de 6,54 x 10^{-12} a^{-1} (Lugmair e Marti, 1978).

3.7 Geoquímica isotópica de enxofre

As composições isotópicas de enxofre (razões $^{34}S/^{32}S$) de pirita foram determinadas no Laboratório de Estudos Geodinâmicos, Geocronológicos e Ambientais da Universidade de Brasília, seguindo os procedimentos descritos por Bender et al. (2008). Grãos de pirita foram selecionados manualmente, montados em epóxi e polidos para vaporização em um sistema de ablação a laser com tamanho de spot de 65 µm. O material ablacionado foi conduzido a um ICP-MS multicoletor Thermo Finnigan Neptune. A frequência do laser foi de 10 Hz com 60% de energia. O padrão interno utilizado foi o Py-BSB. As razões isotópicas ($^{34}S/^{32}S$) são expressas na notação δ (‰) em relação ao Vienna-Canyon Diablo Troilite (V-CDT). A precisão analítica interna está entre ±0,1–0,2 ‰ (2σ).

CAPÍTULO 4

GEOCHEMISTRY, U-Pb GEOCHRONOLOGY, AND Sm-Nd ISOTOPES OF THE GRANITIC ROCKS ASSOCIATED WITH THE ROSA DE MAIO GOLD DEPOSIT IN THE TAPAJÓS MINERAL PROVINCE, BRAZIL: MAGMATIC EVOLUTION, SOURCE CHARACTERIZATION, AND IMPLICATIONS FOR MAGMA FERTILITY

4 GEOCHEMISTRY, U-Pb GEOCHRONOLOGY, AND Sm-Nd ISOTOPES OF THE GRANITIC ROCKS ASSOCIATED WITH THE ROSA DE MAIO GOLD DEPOSIT IN THE TAPAJÓS MINERAL PROVINCE, BRAZIL: MAGMATIC EVOLUTION, SOURCE CHARACTERIZATION, AND IMPLICATIONS FOR MAGMA FERTILITY

Abstract

Porphyry Cu-Au deposits form a continuous spectrum from Cu-rich to Au-rich types. Although they share many common features, Au-rich porphyry deposits are more closely associated with high-K calc-alkaline to alkaline intrusions emplaced at shallow depths in thin continental crust, with associated magmatic rocks displaying lower Sr/Y and La/Yb ratios. The magmatic and hydrothermal factors controlling Cu/Au endowments remain debated and include timing of magmatic sulfide saturation and remobilization of metals during the hydrothermal stage. The Tapajós Mineral Province (TMP) hosts multiple Au(-Cu-Mo) deposits in the southern-central Amazonian Craton (northern Brazil), some recognized as part of porphyry-epithermal systems, associated with either the arc magmatism of the older magmatic sequence (2.0-1.95 Ga) or the post-collisional to early-anorogenic magmatism of the younger magmatic sequence (1.90-1.86 Ga), which includes the Parauari Suite (PAR, 1.89-1.87 Ga). The Rosa de Maio, Bandeirantes, and Maués are magmatic-hydrothermal Au deposits associated with the PAR, with features comparable to those of Au-rich porphyry systems, and whose magmatic evolution and Au fertility remain poorly constrained. In this study, we investigate the fertile magmatism and present new lithogeochemistry, mineral chemistry, Mössbauer spectroscopy on biotite, zircon and monazite U-Pb dating, and Sm-Nd isotope data of the host rocks. Fractional crystallization played a major role in their magmatic evolution, differentiating from tonalitic/granodioritic parental magmas to biotite monzo-/syenogranitic and muscovite syeno-/alkali feldspar granitic magmas. Ferric/ferrous iron ratios estimated by Mössbauer spectroscopy on magmatic biotite indicate oxygen fugacity conditions above the NNO buffer. The Bandeirantes intrusion and the Rosa de Maio Granite (RMG) were emplaced at *ca.* 1907 Ma and 1890 Ma, respectively, in a late- to post-collisional setting, following a period of subduction-controlled arc magmatism. Neodymium isotope data reveal that the sources of

the RMG involve contributions from both juvenile material and crustal rocks from the basement. The RMG shares some similarities with Au-rich porphyry-style deposits, including low Cu/Au ratios, low Sr/Y and La/Yb values of associated magmatic rocks, and relatively oxidized high-K calc-alkaline magmatism in a post-collisional setting. Magmatic sulfide saturation, a potential factor controlling low Cu/Au ratios, may have been a first-order control on the Au fertility of the RMG.

4.1 Introduction

Porphyry Cu-Au deposits are formed at convergent margins, in subduction-related to post-subduction settings, and are typically associated with intermediate to felsic magmatism. They comprise a spectrum of deposits, from Cu-rich to Au-rich and Au-only types (Sillitoe, 2000, 2010). Sillitoe (2000) defined Au-rich porphyry deposits as those with average Au contents ≥0.4 g/metric ton (t), whereas Kesler et al. (2002) proposed a Cu/Au ratio threshold of <40,000, and Chiaradia (2021) suggested a more restrictive Cu/Au ratio of <12,500 to classify such deposits as Au-rich.

Although broadly similar, Cu-rich and Au-rich porphyry deposits exhibit key differences. Cu-rich deposits are strongly linked to calc-alkaline magmas generated during subduction in Andean-type arc settings, while Au-rich porphyry deposits are associated not only with calc-alkaline magmas but also with high-K calc-alkaline to alkaline magmas formed in post-collisional to extensional tectonic settings (Chiaradia, 2020, 2021, 2022; Park et al., 2021). Crustal thickness and the emplacement depth of intrusions also correlate with Cu/Au ratios: Cu-rich porphyry deposits are generally associated with deep-seated intrusions emplaced in thick continental crust, whereas Au-rich porphyry deposits are linked to shallower intrusions within thinner crust (Murakami et al., 2010; Park et al., 2021; Chiaradia, 2022; Hao et al., 2022). Cu-rich systems are long-lived, water-rich, and associated with large volumes of magma undergoing amphibole-dominant fractionation in the lower crust, resulting in high Sr/Y ratios. In contrast, short-lived Au-rich porphyry systems with lower water contents are commonly linked to less voluminous magma batches dominated by plagioclase

fractionation, producing lower Sr/Y ratios (Chiaradia et al., 2012; Chiaradia, 2015, 2021; Park et al., 2021).

A key factor affecting Cu/Au partitioning is the timing of magmatic sulfide saturation (Park et al., 2019, 2021; Hao et al., 2022). Early sulfide saturation in Cu-rich systems formed at deep crustal levels depletes the residual magma in Au relative to Cu, resulting in higher Cu/Au ratios in the exsolving hydrothermal fluids. Conversely, Au-rich porphyry systems emplaced at shallower depths tend to experience late sulfide saturation, allowing magmas to retain higher Au concentrations available to fluids (Park et al., 2021; Hao et al., 2022; Chiaradia, 2022). Since sulfide saturation likely occurs during the evolution of most arc magmas – regardless of composition or geodynamic setting (Georgatou and Chiaradia, 2020) – it may represent a critical control on Cu/Au endowment in porphyry deposits.

The Tapajós Mineral Province (TMP), located in the southern Amazonian Craton in northern Brazil (Fig. 4.1), hosts several Au(-Cu) deposits included in porphyry-epithermal systems (Juliani et al., 2005; Echeverri Misas, 2015; Cassini, 2016; Borgo et al., 2017; Lopes and Moura, 2019; Juliani et al., 2021; Cassini et al., 2022), intrusion-related-gold-systems (IRGS, Santos et al., 2001; Villas et al., 2013), and hybrid systems combining IRGS and Au-rich porphyry features (Juliani et al., 2002; Borges et al., 2009; Biondi et al., 2018).

In this study, we investigate the Rosa de Maio, Bandeirantes, and Maués magmatic-hydrothermal Au deposits, which are hosted in the TMP and display features similar to those of Au-rich porphyry-style deposits, but for which the controls on Au fertility remain poorly constrained. These deposits are hosted by high-K calc-alkaline to shoshonitic granitic rocks of the Parauari Suite (PAR, 1.89-1.87 Ga; Santos et al., 2000, 2004), emplaced after a period of subduction-controlled arc magmatism in the late stages of the tectonic evolution of the TMP (Cassini et al., 2020).

This contribution aims to fill a gap in the basic petrological knowledge of the Rosa de Maio, Bandeirantes, and Maués intrusions, which host these magmatic-hydrothermal gold deposits in a still barely known area of the northwestern TMP. With a focus on the Rosa de Maio intrusion, we present new

lithogeochemical data of the unaltered host rocks, mineral chemistry, Mössbauer spectroscopy on biotite, zircon and monazite U-Pb dating, and Sm-Nd isotope data. Coupled with classical petrography, these data allow us to discuss the magmatic system, oxygen fugacity conditions, crystallization ages, and source rocks. Finally, we discuss the similarities between the Rosa de Maio deposit and Au-rich porphyry deposits and explore the potential role of magmatic sulfide saturation as a first-order control on its low Cu/Au ratios.

4.2 Geological framework

The TMP is a metallogenic province composed mostly of Au(-Cu) deposits in the southern portion of the Amazonian Craton in northern Brazil (Fig. 4.1). These deposits are hosted by Paleoproterozoic volcanic and plutonic rocks which are part of the Central Amazonian and Ventuari-Tapajós geochronological provinces proposed by Tassinari and Macambira (1999) or the Central Amazon and Tapajós-Parima provinces proposed by Santos *et al.* (2000). According to Santos *et al.* (2000, 2004), the Tapajós-Parima Province is an Orosirian collisional orogen formed by the suture of multiple magmatic arcs with an older Archean-Paleoproterozoic continental crust, culminating in a NW-SE laterally continuous crustal segment. In this tectonic model, granitic magmatism was generated in two orogenies and evolved from primitive island arc magmatism to mature continental arc and post-orogenic magmatism. Carneiro *et al.* (2018) revised this model and proposed a new tectonic evolution. Based on magnetic data, they interpret deep E-W trending structures under the TMP (*ca.* 15 km) as evidence of westward continuity of the Carajás Province. The NNW-SSE structures at the surface are considered the result of shallower tectonic regimes. In this new evolution, the TMP is rather a continental accretionary orogen (similar to the Andean Cordillera) developed on an Archean basement than an amalgamation of multiple magmatic arcs (*e.g.*, Alves et al., 2020).

The igneous suites associated with the TMP are grouped into the older magmatic sequence (OMS, 2.0-1.95 Ga) and the younger magmatic sequence (YMS, 1.90-1.86 Ga), being separated by a hiatus of approximately 50 million years (Table 4.1, Cassini *et al.*, 2020; Cassini *et al.* 2022). In the tectonic model of Santos *et al.* (2004), the OMS and YMS correspond to units grouped into the

Mundurucus and Tropas orogenies, respectively (Table 4.1). The OMS includes the Jacareacanga Group (2.2-2.0 Ga, low-grade metavolcanic and metasedimentary rocks), the Cuiú-Cuiú Complex (2.04-1.99 Ga, tonalite and granodiorite), the Vila Riozinho Formation (2.0 Ga, basaltic-andesite, trachyte, and rhyolite), the Jamanxim Suite (2.0-1.98 Ga, monzogranite), and the Creporizão Suite (1.99-1.95 Ga, high-K calc-alkaline granitic rocks) (Santos *et al.*, 2000, 2001, 2004; Lamarão *et al.*, 2002). According to Santos *et al.* (2004), these igneous units virtually represent the evolution of arc magmatism in the transition from island arc to Andean-type continental arc (see Table 4.1). Cassini *et al.* (2020) interpret them as a magmatic arc stage dominated by anhydrous magmas with a strong crustal component at *ca.* 2.0 Ga, followed by arc magmatism between 1.98-1.95 Ga with minimal crustal contamination, forming metaluminous to mildly peraluminous, hydrous, and oxidized magmas.

The YMS comprises the Tropas Suite (1.90-1.88 Ga, tonalite and granodiorite), the Parauari Suite (1.89-1.87 Ga, tonalite, granodiorite, monzo- and syenogranite), and the Iriri Group (1.89-1.87 Ga, high-K to shoshonite series intermediate to acidic volcanic rocks; Santos *et al.*, 2000, 2001, 2004). This group consists of the Bom Jardim (1.89-1.88 Ga, basaltic-andesite, andesite, trachyte, and ignimbrites), Salustiano (1.88-1.87 Ga, dacite, rhyodacite, rhyolite), Aruri (1.88-1.87 Ga, acidic tuffs, volcanic breccias, and dacitic ignimbrites), and Moraes Almeida (1.89-1.87 Ga, rhyolite, trachyte, and ignimbrites) formations (Santos *et al.*, 2000, 2001, 2004; Lamarão *et al.*, 2002; Table 4.1). These units represent continental arc magmatism and volcanism in a mature Andean-type arc to post-orogenic setting after 50 million years of quiescence following the OMS (Dall'Agnol *et al.*, 1999; Santos *et al*., 2000, 2001, 2004; Lamarão *et al.*, 2002; Juliani *et al.*, 2005; Cassini *et al.*, 2020, 2022). The Maloquinha Suite (1.87-1.86 Ga, high-K to shoshonite series syeno- and alkali feldspar granite; Santos *et al.*, 2000, 2004) represents the last stage of granitic magmatism within the YMS in a post-orogenic to early-anorogenic setting (Santos *et al*., 2000, 2001, 2004; Lamarão *et al.*, 2002; Cassini *et al.*, 2020, 2022). A summary of the main rock types, corresponding geotectonic settings, and associated mineral deposits for these lithostratigraphic units is presented in Table 4.1.

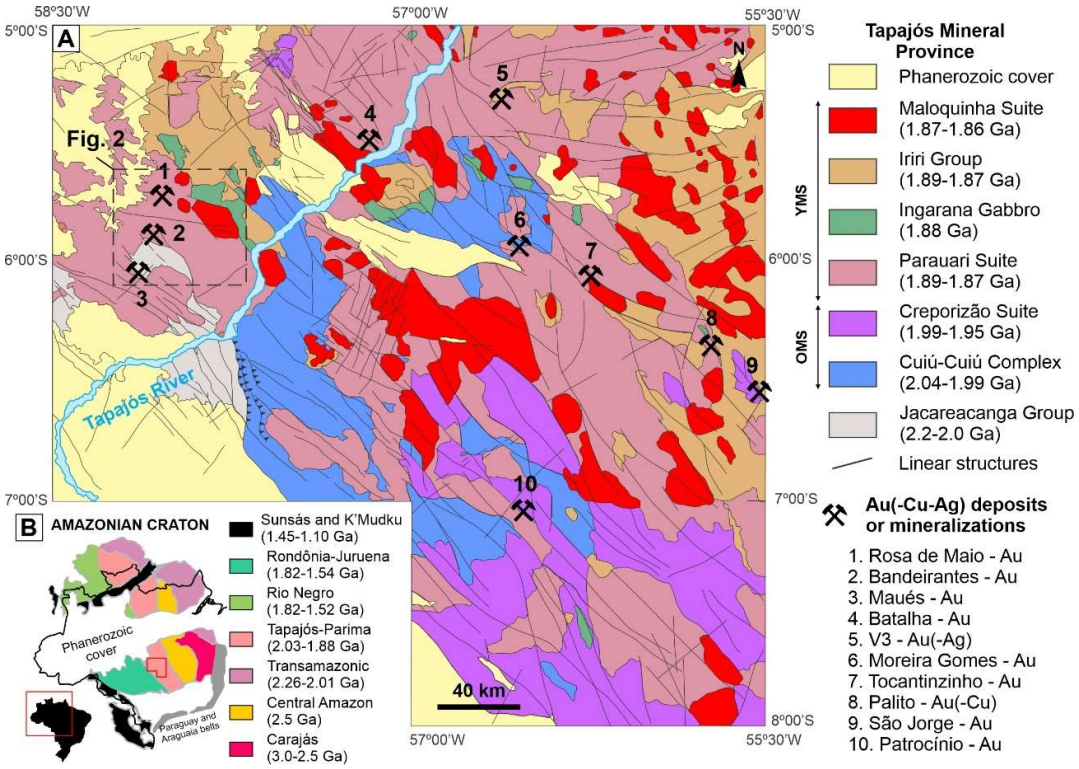

Figure 4.1 – A) Simplified geological map of the Tapajós Mineral Province (TMP) showing some of the main Au(-Cu-Ag) deposits. B) Location of the TMP within the Amazonian Craton. Tectonic subdivisions of the craton after Santos et al. (2000, 2006). Modified from Klein et al. (2001). OMS = Older magmatic sequence; YMS = Younger magmatic sequence.

The Parauari Suite (PAR) is ubiquitous in the TMP (Fig. 4.1) and comprises biotite and/or hornblende monzogranites and syenogranites, with minor gabbros (Santos *et al.*, 2004). These rocks intruded the Cuiú-Cuiú Complex and the Creporizão Suite (Santos *et al.*, 2000, 2004). The PAR is named after the localization of the Au-mineralized Rosa de Maio Granite (RMG) in the Parauari River basin (Santos *et al.*, 2000; Santos *et al.*, 2004), which is part of the much larger Amazon drainage basin. Zircon grains from a monzogranite of the Rosa de Maio batholith were dated by Santos *et al.* (2000) and yielded a U-Pb TIMS discordant date with an upper intercept at 1879 ± 11 Ma, whereas Santos *et al.* (2004) obtained a U-Pb TIMS zircon concordant date of 1879 ± 3 Ma from the same sample. Both dates are interpreted as crystallization ages. Sm-Nd isotope data obtained by Santos *et al.* (2000) from the PAR yielded εNd (1.89 Ga) values between -0.87 and +1.83 with T_{DM} model ages around 2.1 Ga, whereas Echeverri Misas (2015) obtained εNd (1.88 Ga) values between -3.2 and +0.3 with T_{DM} model ages from 2.1 to 2.4 Ga for the PAR rocks hosting the Palito Au(-Cu) deposit in the southern Tapajós Domain. The Ingarana Gabbro (1881 ± 3 Ma;

Santos *et al.*, 2004) comprises calc-alkaline augite gabbros, which were included in the magmatic evolution of the PAR by Santos *et al.* (2004). Its mafic composition and coeval emplacement with the PAR led these authors to interpret the suite as bimodal. According to the tectonic model of Santos *et al.* (2004), the PAR represents a third continental arc formed after the island arc phase (Tropas Suite, 1.90-1.88 Ga) of the Tropas Orogeny in the context of the Tapajós-Parima Orogen (2.0-1.87 Ga). In a recent model proposed by Cassini *et al.* (2020), the PAR represents a high-K calc-alkaline to shoshonitic, metaluminous to weakly peraluminous granitic magmatism generated by partial melting of a progressively metasomatized mantle wedge above a long-lived subduction zone within a continental accretionary orogen. In this model, the PAR magmatism took place in a late- to post-orogenic setting and represents the onset of the YMS.

The Batalha (Au-only, Juliani et al., 2002) and Palito (Au-Cu, Echeverri Misas, 2010, 2015) deposits are hosted in 1.88 Ga granitoid rocks associated with the PAR. The Batalha Granite (1883 ± 4 Ma) comprises hornblende and/or biotite syeno- to monzogranite linked to the post-collisional magmatism of the PAR (Juliani et al., 2002) in the northern portion of the TMP (*ca.* 100 km northeast of the RMG, Fig. 4.1). These granites are metaluminous to peraluminous, ferroan, high-K calc-alkalic to alkali-calcic, and were emplaced at shallow depths (Juliani et al., 2002). During the hydrothermal stage (*ca*. 500-290 °C and 2.6-1.2 kbar), they were affected by early Na metasomatism followed by pervasive to fissural potassic, propylitic, and sericitic alterations. Gold mineralization is associated with the latter two, particularly the sericitic alteration (Juliani et al., 2002). According to Juliani et al. (2002), the Batalha Au deposit display features indicative of both porphyry-like deposits and intrusion-related gold systems (IRGS), and share similar characteristics with gold-rich porphyry-like deposits of the YMS (*e.g.*, Palito and Rosa de Maio; see Echeverri Misas, 2015; Juliani et al., 2021; Cassini et al., 2022). These gold-rich porphyry-like deposits are deemed to be linked to high-sulfidation epithermal mineralization in the TMP (Juliani et al., 2005, 2021).

Table 4.1 – Summary of the main lithostratigraphic units of the TMP. Modified from Cassini et al. (2020, 2022).

	Tectonic subdivision	Lithostratigraphic unit		Description	Geotectonic context	Deposit/Mineral occurrence
Tapajós Mineral Province - TMP (closely correlates with the Tapajós-Parima Orogen[3])	Younger magmatic sequence (YMS)[6] or Tropas Orogeny[3]	Maloquinha Suite (1.87-1.86 Ga)[2, 3, 4]		Shoshonitic syeno- to alkali feldspar granite	Post-orogenic[1, 2, 3], Post-orogenic to early-anorogenic[6]	
		Iriri Group (1.89-1.87 Ga)[2, 3, 5]	Moraes Almeida	High-K calc-alkaline to shoshonitic intermediate to acidic volcanic rocks	Multiple interpretations including magmatic arc and post-orogenic to early-anorogenic[1, 2, 3, 4, 5, 6]	V3 (Au)[13]
			Aruri			
			Salustiano			
			Bom Jardim			
		Parauari Suite (1.89-1.87 Ga)[2, 3, 6]		High-K calc-alkaline to shoshonitic tonalitic to syenogranitic rocks	Magmatic arc[2, 3], Late- to post-orogenic[6]	Rosa de Maio (Au), Bandeirantes (Au), Batalha (Au)[12], Palito (Au-Cu)[13], São Jorge (Au)[4, 14]
		Tropas Suite (1.90-1.88 Ga)[2, 3]		Tonalite and granodiorite	Island arc[2, 3]	
	Older magmatic sequence (OMS)[6] or Mundurucus Orogeny[3]	Creporizão Suite (1.99-1.95 Ga)[2, 3, 6]		High-K calc-alkaline to shoshonitic tonalitic to syenogranitic rocks	Magmatic arc[2, 3, 6]	Tocantinzinho (Au)[7, 8, 9], Patrocínio (Au)[10], Moreira Gomes (Au)[11]
		Jamanxim Suite (2.0-1.98 Ga)[3]		Monzogranite		
		Vila Riozinho Formation (2.0 Ga)[4]		Calc-alkaline to shoshonitic intermediate to acidic volcanic rocks	Magmatic arc[4]	
		Cuiú-Cuiú Complex (2.04-1.99 Ga)[1, 2, 3]		Calc-alkaline tonalite, diorite, granodiorite	Island arc[1, 2, 3], Magmatic arc[6]	
		Jacareacanga Group (2.2-2.0 Ga)[1, 2, 3]		Metavolcanic and metasedimentary rocks	Back-arc and trench sedimentation[1, 2, 3]	

References: 1 - Santos et al. (2000), 2 - Santos et al. (2001), 3 - Santos et al. (2004), 4 - Lamarão et al. (2002), 5 - Juliani et al. (2005), 6 - Cassini et al. (2020), 7 – Borgo et al. (2017), 8 – Biondi et al. (2018), 9 – Lopes and Moura (2019), 10 – Cassini (2016), 11 - Assunção and Klein (2014), 12 - Juliani et al. (2002), 13 - Echeverri Misas (2015), and 14 – Borges et al. (2009).

The Palito Granite (1883 ± 11 Ma, Aquino et al., 2013) consists of metaluminous to peraluminous, ferroan, and high-K alkali-calcic biotite monzogranite to alkali feldspar granite (Echeverri Misas, 2010, 2015; Cassini et al., 2022). It was also emplaced in the context of the post-collisional magmatism of the YMS during flattening of the slab under an evolved continental arc represented by the OMS (Cassini et al., 2020, 2022). These granites were affected by pervasive potassic metasomatism, followed by pervasive and fissural propylitic and sericitic alterations (Echeverri Misas, 2010, 2015). The Au-(Cu) mineralization is mostly associated with the sericitic alteration and is represented

by quartz-sulfide and sulfide (*e.g.*, chalcopyrite, pyrite, galena) veins and veinlets (Echeverri Misas, 2015). The Palito deposit is interpreted by Echeverri Misas (2015) as a gold-rich (Au-Cu) porphyry deposit.

In addition, the São Jorge gold deposit is partially associated with granitoid rocks of the PAR (Cassini et al., 2022). The younger São Jorge Granite (1891 ± 3 Ma, Lamarão et al., 2002) hosts most of the gold mineralization and is composed of metaluminous to peraluminous, magnesian to ferroan, and high-K alkali-calcic hornblende-biotite monzogranite (Borges et al., 2009, Cassini et al., 2022). Gold mineralization is predominantly associated with propylitic and sericitic alterations. According to Borges et al. (2009), this deposit displays characteristics of both porphyry-like and IRGS deposits.

The PAR hosts all these deposits and represents a high-K calc-alkaline to shoshonitic post-orogenic magmatism (onset of the YMS at *ca.* 1.90 Ga) generated during flattening of the slab after progressive metasomatism of the mantle wedge under an evolved continental arc (*i.e.*, the OMS from 2.0 to 1.95 Ga, see Cassini et al., 2020). Cassini et al. (2022) consider the YMS (particularly the PAR) fertile for the formation of gold-rich magmatic-hydrothermal systems and propose remobilization of gold from residual sulfides previously formed within the metasomatized subcontinental lithospheric mantle (SCLM) and/or lower crust as a mechanism of gold enrichment in the granitic magmas of the PAR.

4.3 Analytical methods and procedures

4.3.1 Lithogeochemistry

Sample preparation was carried out in the Laboratório de Preparação de Amostras of the Instituto de Geociências of the University of Brasília (Brazil) and involved hand sample disaggregation, crushing, pulverization with a swing mill, and quartering. Major, minor, and trace element bulk rock analyses of 23 samples were conducted at ACME Analytical Laboratories Ltd. (Vancouver, Canada). The standard analytical procedure involves blending rock pulps with lithium tetraborate and then melting the mixture to produce fused glass beads. The fused beads undergo X-ray fluorescence spectroscopy (XRF) analysis for major elements and inductively coupled plasma mass spectrometry (ICP-MS) for minor

and trace elements. Further information on analytical procedures is available at acmelab.com.

4.3.2 Mineral chemistry

Chemical compositions of biotite were obtained using a JEOL JXA-8230 electron microprobe at the Instituto de Geociências of the University of Brasília (Brazil). Analyses of Si, Ti, Al, Fe, Mn, Mg, Ca, Ba, Na, K, F, and Cl were performed on polished thin sections (30 μm thick) at an accelerating voltage of 15 kV and a beam current of 10 nA with 1 μm spot diameter. Dwell times in all elements were 10 s at peak and 5 s in the background. The Kα X-ray line was used for all elements. Standards were the following reference materials: microcline (Si, Al, and K), andradite (Fe and Ca), barite (Ba), albite (Na), forsterite (Mg), topaz (F), vanadinite (Cl), and pyrophanite (Ti and Mn). Data reduction was carried out using the microprobe software package.

4.3.3 Mössbauer spectroscopy

Mössbauer spectroscopy analyses on biotite were conducted at the Laboratório de Espectroscopia Mössbauer of the University of Brasília, Brazil. Biotite concentrates were obtained through standard mineral separation procedures, including rock crushing, grinding, sieving, and magnetic separation. Mössbauer spectra were obtained at room temperature by using a conventional constant acceleration spectrometer with ^{57}Co/Rh as the radioactive source and an integrated multichannel analyzer and proportional counter as detector in the transmission geometry. The calibration was carried out by using a natural Fe foil. Isomer shift values are calculated with respect to Fe-α at room temperature. The spectra analyses were carried out using a least-square fitting routine using the Normos software and assuming Lorentzian peak shapes. Estimates of Fe^{3+}/Fe^{2+} ratios in biotite were determined by combining EPMA analyses (total Fe as FeO) with Mössbauer spectroscopy results.

4.3.4 U-Pb isotope systematics

U-Pb isotope data of zircon and monazite were obtained at the Laboratório de Estudos Geodinâmicos, Geocronológicos e Ambientais of the University of Brasília, Brazil. The masses of interest were measured on a Thermo Finningan

Element XR high-resolution single-collector sector field ICP-MS coupled to a 193 nm Iridia Excimer (ArF) laser ablation system. The laser ablation system is equipped with a Cobalt dual-volume chamber. The mass spectrometer was tuned to improve U and Pb sensitivity while minimizing oxide production prior to each analytical session. Each analysis consisted in 10 s of background measurement followed by 20 s of sample acquisition. Each mass (202, 204, 206-208, 232, 238) were measured using the triple detection mode (SEM+Faraday) by sweeping the electrostatic sector on each mass. Each sweep consisted in 82 ms, resulting in over 800 scans for each ablation. Laser conditions included a spot diameter of 25 μm, 20 Hz, and 2.0 $J.cm^{-2}$. Complete acquisition parameters can be found on Appendix A. Raw data was processed on Iolite 4.0 (Paton et al., 2011) as time-resolved signal and individual signal inspection was done with assistance of the VizualAge (Petrus and Kamber, 2012). Data correction included blank subtraction, LIEF correction using an exponential plus linear model and normalization by the GJ-1 zircon (Jackson et al., 2004). The following reference materials were used for quality control: 91500 zircon (Wiedenbeck et al., 1995), Plešovice zircon (Sláma et al., 2008), Itambé monazite (Gonçalves et al., 2016), and STK monazite (Fisher et al., 2020). Excess variance on the primary calibrant was propagated on each analytical point. Systematic uncertainty of ca. 1% is propagated on each final age. No common lead correction was applied. Ages are quoted at 2σ. Wetherill diagrams were generated using the online version of IsoplotR (Vermeesch, 2018).

4.3.5 Sm-Nd isotope systematics

Sm and Nd isotope analyses of whole-rock powder were carried out via TIMS at the Laboratório de Estudos Geodinâmicos, Geocronológicos e Ambientais of the University of Brasília (Brazil), following the analytical procedures described by Gioia and Pimentel (2000). A Finnigan TRITON spectrometer with seven collectors in static mode was employed. Spike solutions of ^{149}Sm and ^{150}Nd were added to the whole-rock powder samples. The separation of Sm from Nd was achieved using cation exchange columns, followed by evaporation with two drops of 0.025 NH_3PO_4. The residue was then dissolved in 1 μl of 5% distilled HNO_3, and loaded onto a double Re filament assembly. The

BHVO-2 international rock standard was used, along with a decay constant of 6.54×10^{-12} y^{-1} (Lugmair and Marti, 1978).

4.4 Results

4.4.1 Field relationships and petrography

The Rosa de Maio Granite (RMG) hosts primary gold mineralization and outcrops in an area of at least 200 km^2 within an 8 km radius from the Rosa de Maio *garimpo* (artisanal mining camp), where secondary gold is mined from a placer deposit (Fig. 4.2). In the vicinity of the *garimpo*, the RMG is undeformed and is intruded by the Maloquinha Suite (1.87-1.86 Ga, Santos et al., 2000, 2001, 2004). In addition, granitic rocks similar to the RMG also host primary gold mineralization in the vicinity of the Bandeirantes and Maués placer deposits (*i.e.*, *garimpos*), which are located at distances of 20 km and 40 km (Fig. 4.2), respectively, from the Rosa de Maio *garimpo*.

Unaltered rock types in the RMG are essentially biotite monzo- to syenogranite (Figs. 4.3A to C, G, and H) and muscovite-rich aplite of syenogranitic to alkali feldspar granitic composition (Figs. 4.3D, H, and I). The biotite monzo- to syenogranite is the main rock type in the RMG and is composed of quartz (~30-40%), plagioclase (An_{10-40} Ab_{57-88} $Or_{0.5-2.5}$; ~25-45%), microcline (perthitic, ~20-40%), biotite (~4-12%), and muscovite (~1%). Accessory phases are fluorapatite, zircon, monazite, xenotime, magnetite (up to 0.3 wt.% TiO_2), ilmenite (3-16 wt.% MnO), and pyrite (Figs. 4.4A to F). The muscovite-rich aplite occurs in a much lesser extent and is composed of quartz (~40-50%), microcline (~20-40%), plagioclase ($An_{0.5-6.5}$ Ab_{93-99} $Or_{0.4-0.8}$; ~15-20%), and muscovite (~3-15%). Accessory phases are fluorapatite, zircon, tourmaline, biotite, and ilmenite (~12 wt.% MnO, Figs. 4.4J to L).

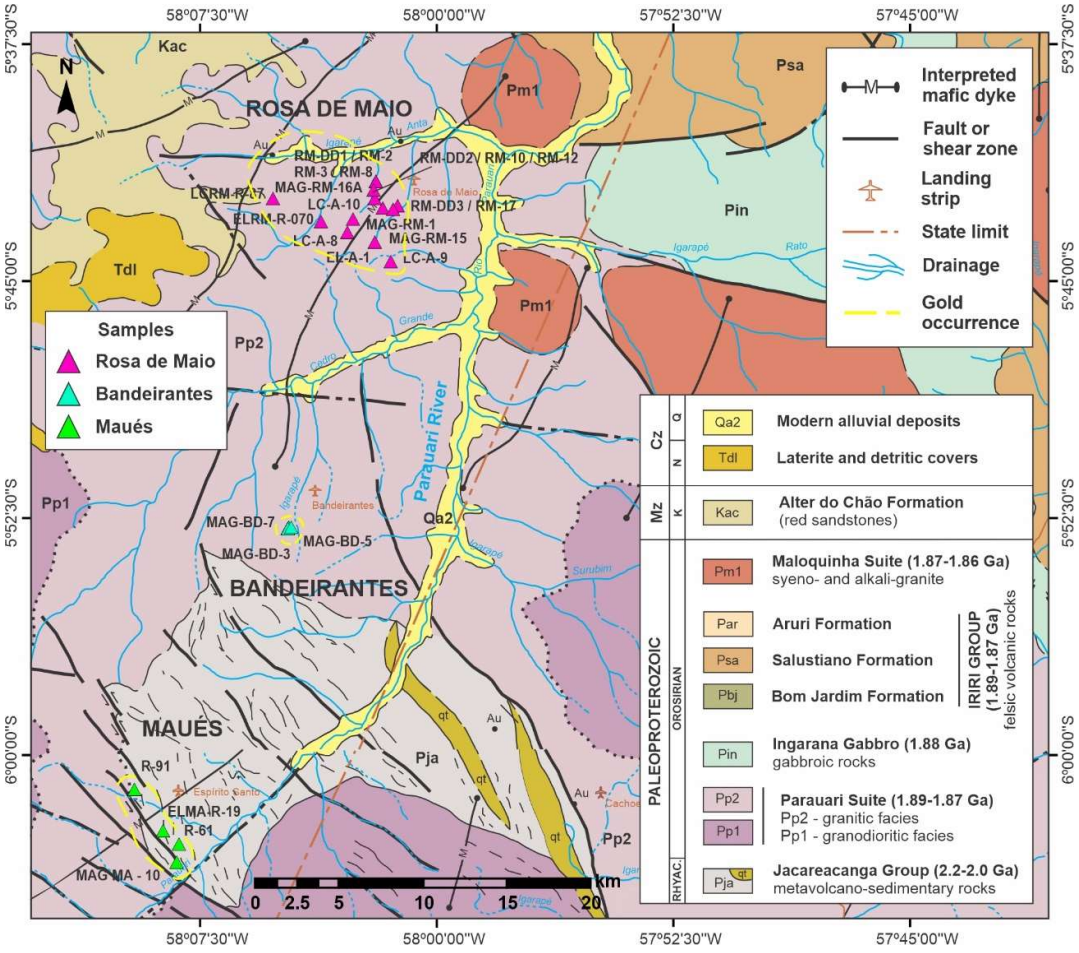

Figure 4.2 – Geological map of the studied area with samples collected from the Rosa de Maio, Bandeirantes, and Maués intrusions. Whole-rock geochemical analyses of these samples are presented in Table 4.2. Modified from Klein et al. (2001).

The biotite monzo- to syenogranite (Fig. 4.3A) is hololeucocratic to leucocratic and displays isotropic fabric characterized predominantly by porphyritic texture (Fig. 4.3B). This porphyritic texture consists of perthitic microcline and minor zoned plagioclase phenocrysts (oscillatory zoning; Fig. 4.4A) within a medium- to coarse-grained groundmass composed of euhedral biotite, subhedral plagioclase, euhedral to anedral quartz (often occurring as hexagonal prisms, Figs. 4.4B and D), and interstitial microcline (Figs. 4.4B, C, and F). Accessory phases commonly occur as inclusions in biotite (*e.g.*, apatite, zircon, and monazite; Figs. 4.4E and F).

The muscovite-rich aplite occurs as centimeter- to decimeter-scale dykes that crosscut the biotite granite (Figs. 4.3D and G to I). The aplite is hololeucocratic and displays isotropic fabric characterized by medium-grained

equigranular to porphyritic texture (Figs. 4.4D, H, and I). This texture consists of euhedral to anedral quartz (Figs. 4.4J and L), subhedral muscovite and plagioclase, and subhedral to anedral microcline (Fig. 4.4J). An important feature of the muscovite-rich aplite is the occurrence of tourmaline as a primary phase (Fig. 4.4K).

Biotite-rich, undeformed enclaves are widespread in the RMG (Fig. 4.3E) and are referred to as microgranitoid enclaves (ME) in this study. The ME are tonalitic to granodioritic in composition, consisting of plagioclase (An_{25-45} Ab_{52-74} $Or_{0.7-3.5}$; ~40-45%), quartz (~30-40%), biotite (~20-25%), and microcline (~1-10%; Figs. 4.4G to I). Accessory phases are fluorapatite, zircon, and magnetite (up to 2.5 wt.% TiO_2). The ME are leucocratic, isotropic, and display inequigranular to porphyritic textures. The porphyritic texture consists of zoned plagioclase (oscillatory zoning; Fig. 4.4H) and biotite phenocrysts embedded within a fine-grained groundmass composed of plagioclase, biotite, and interstitial quartz (Figs. 4.4G to I). Fine-grained plagioclase laths and biotite lamellae are commonly enclosed by quartz (Fig. 4.4G). In contrast, rounded biotite-rich schist enclaves, characterized by a tectonic foliation defined by biotite and quartz and occurring at a centimeter scale, are interpreted as xenoliths (Fig. 4.3F).

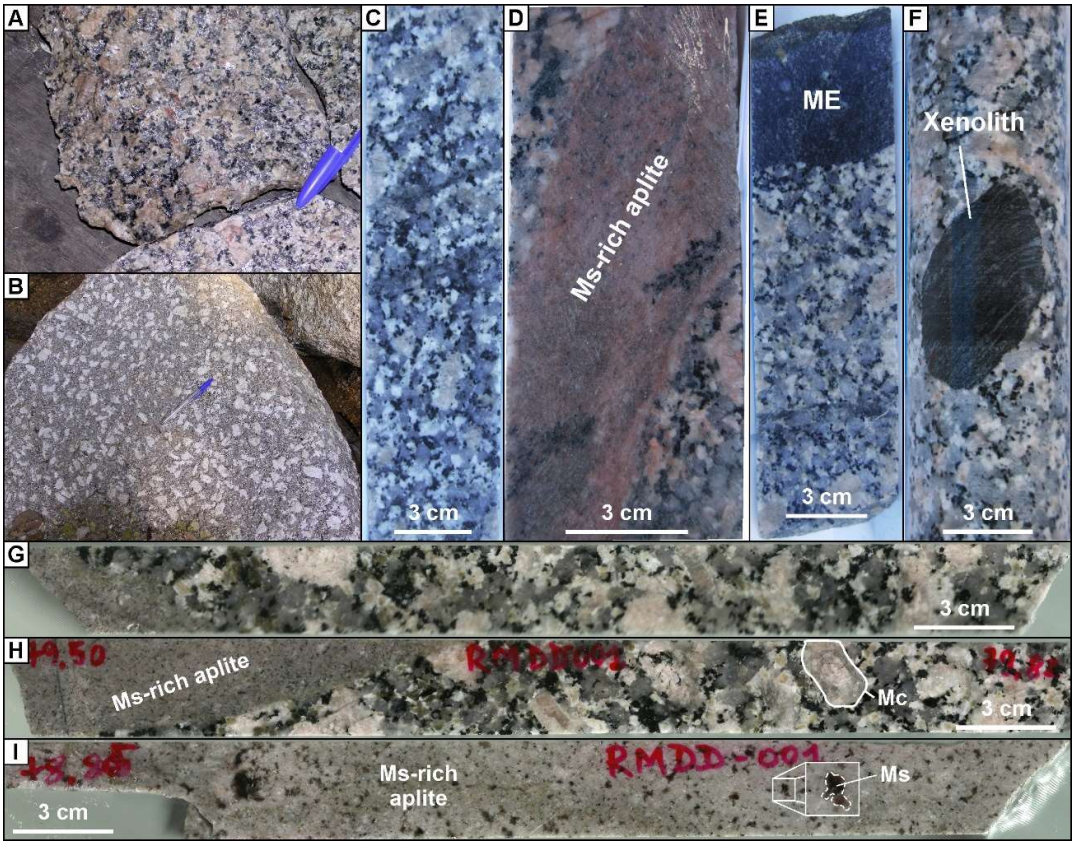

Figure 4.3 – Main rock types of the RMG. A), B) and C) Porphyritic biotite monzogranite, the dominant rock type in the RMG. D) Muscovite-rich aplitic dyke crosscutting the biotite granite. E) and F) Sharp contact between an ME and a xenolith, respectively, and the biotite granite. Note the foliation defined by quartz as thin bands in F). G) and H) Medium-grained muscovite-rich aplitic dykes crosscutting the porphyritic biotite granite. I) Porphyritic muscovite-rich aplite of alkali feldspar granitic composition. Note the muscovite phenocrysts. Ms = muscovite and Mc = microcline. Abbreviations after Whitney and Evans (2010).

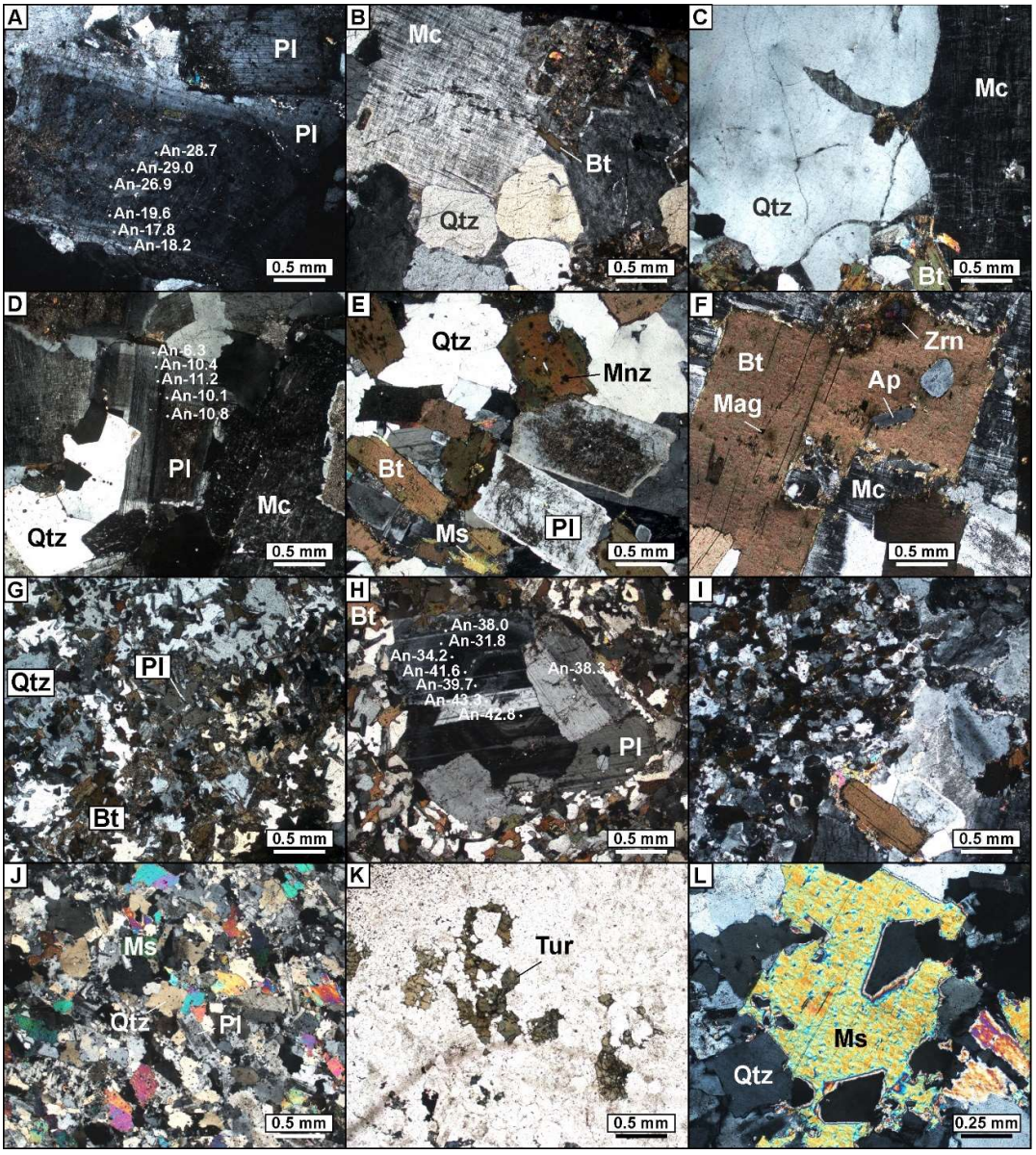

Figure 4.4 – Photomicrographs of the main rock types of the RMG in plane-polarized (PPL) and cross-polarized (XPL) light. A) to F) Biotite granite, G) to I) ME, and J) to L) muscovite-rich aplite. A) Two generations of plagioclase: a phenocryst with oscillatory zoning and indicated An contents from core to rim, and an unzoned crystal. B) and C) Subhedral quartz crystals completely and partially enclosed by microcline. D) Subhedral quartz crystal partially enclosed by zoned plagioclase showing incipient albitization (An contents indicated from core to rim). E) Euhedral biotite lamellae with monazite inclusions. F) Zircon, apatite, and magnetite inclusions within biotite, which is partially enclosed by microcline. G) Fine-grained subhedral biotite lamellae and plagioclase laths, partially and completely enclosed by quartz. H) Plagioclase phenocryst with oscillatory zoning and indicated An contents from core to rim, embedded within a fine-grained biotite + plagioclase + quartz groundmass. I) Sharp contact between the ME and the biotite granite. J) Medium-grained equigranular muscovite-rich aplite. K) Primary tourmaline in the muscovite-rich aplite. L) Subhedral quartz crystals partially enclosed by a muscovite flake. Pl = plagioclase, Qtz = quartz, Mc = microcline, Bt = biotite, Ms = muscovite, Mnz = monazite, Zrn = zircon, Ap = apatite, Mag = magnetite, and Tur = tourmaline. Abbreviations after Whitney and Evans (2010).

4.4.1.1 Hydrothermal alteration and mineralization

The porphyritic biotite granite is the most abundant and voluminous rock type in the RMG and represents the main host for hydrothermal alteration and mineralization in the Rosa de Maio deposit. The hydrothermal assemblages described in this study result from the interaction between hydrothermal fluids and this granite. Five alteration types were identified: sodic, potassic, propylitic, sericitic, and silicification. Gold mineralization is mostly associated with zones of sericitic alteration and silicification, with average ore Cu/Au ratios around 4,650 and values locally reaching up to 34,780 in these mineralized zones. The sequence of magmatic and early- to late-stage hydrothermal assemblages is presented in Figure 4.5.

Sodic alteration represents the earliest stage of the hydrothermal phase in the RMG. It is the most widespread alteration, extending up to several hundred meters from the intrusion center. In moderately altered granites, magmatic textures are largely preserved, and the granites retain characteristics of their unaltered equivalents. This alteration is characterized by the pervasive and partial replacement of magmatic plagioclase, forming discrete albite rims surrounding plagioclase cores altered to sericite. It is also represented by the precipitation of chessboard albite.

Potassic alteration is also widespread in the RMG and overprints the sodic alteration. It occurs as veins surrounded by a pervasive alteration front (*i.e.*, fissural to pervasive) that extends up to a few tens of meters. The porphyritic texture is generally preserved, with the main macroscopic characteristic being a color shift from gray in sodic-altered and unaltered granites to deep reddish in strongly potassic-altered rocks. At the microscopic scale, this alteration is characterized by the pervasive replacement of magmatic biotite by fine-grained aggregates of hydrothermal biotite, forming patches that partially or completely replace the coarser-grained magmatic biotite. The potassic alteration assemblage includes biotite, quartz, and hematite, with minor sericite, carbonate, and chlorite.

Propylitic alteration is volumetrically less extensive and overprints earlier alteration assemblages. It occurs proximal to the intrusion center as centimeter-

scale veins surrounded by a pervasive alteration front (also fissural to pervasive) that extends up to a few meters. This alteration is highly texture-destructive, partially to completely obliterating the magmatic rock fabric, including the porphyritic texture. At the macroscopic scale, the most prominent characteristic is the color change from the deep reddish tones of potassic-altered granites to the dark gray to greenish hues typical of propylitic-altered granites. This alteration is characterized by the pervasive replacement of plagioclase, biotite (both magmatic and hydrothermal), and microcline by chlorite, epidote, clinozoisite, calcite, pyrrhotite, quartz, fluorite, and sericite. This results in a propylitic alteration assemblage that comprises chlorite, epidote/clinozoisite, calcite, quartz, pyrrhotite, chalcopyrite, albite, and minor sericite, fluorite, and ilmenite.

Sericitic alteration is also fissural to pervasive, overprints earlier assemblages, and is less voluminous than the sodic and potassic alterations. It occurs from proximal to distal zones of the intrusion center as millimeter- to centimeter-scale veins surrounded by a pervasive alteration front. The pervasive alteration front extends from a few centimeters to a few meters. This alteration obliterates the magmatic rock fabric, with macroscopic samples displaying dark gray to black hues. It is characterized by the pervasive replacement of previous alteration assemblages by sericite, pyrite, and quartz with minor biotite, albite, chlorite, fluorite, and calcite. Fractures supplying fluid to this pervasive alteration are commonly filled with massive sulfides (mostly pyrite), sericite, and quartz. In the sericitic alteration, gold mineralization is intimately associated with sulfides, particularly pyrite, occurring as fine-grained inclusions or closely associated with them. The sericitic alteration assemblage comprises sericite, pyrite, quartz, chalcopyrite, galena, gold, and minor fluorite, native bismuth, biotite, chlorite, albite, calcite, ilmenite, and rutile.

Silicification is coeval with the development of intense quartz stockwork veining and represents the latest hydrothermal stage in the RMG, predominantly affecting upper distal zones at the top of the intrusion center. Decimeter-scale quartz-sulfide veins form a stockwork system from which a pervasive wallrock alteration extends (*i.e.*, fissural to pervasive), forming silicified zones with disseminated sulfides that extend up to a few decimeters. These zones typically display light gray hues and very fine-grained quartz. Gold mineralization in this

alteration stage is also intimately associated with sulfides, predominantly pyrite, which occurs both disseminated in the wallrock and filling veins together with quartz. The silicification assemblage comprises quartz, pyrite, gold, and galena, with minor chalcopyrite and sericite.

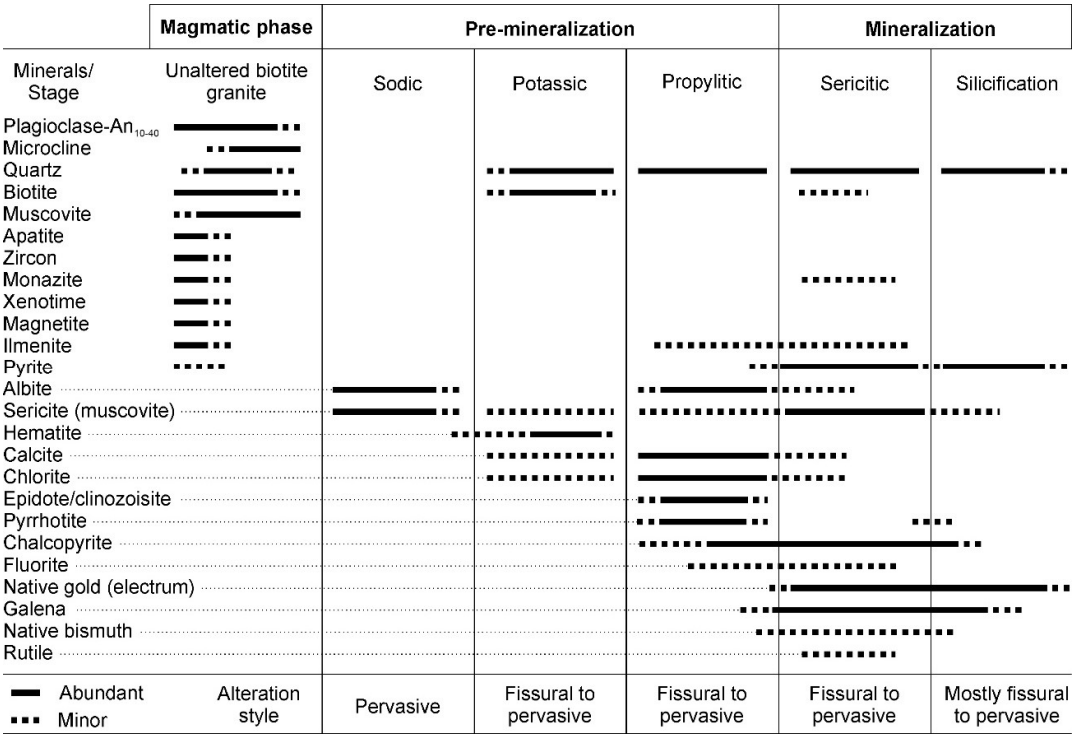

Figure 4.5 – Paragenetic sequence of hydrothermal alteration assemblages in the Rosa de Maio deposit.

4.4.2 Lithogeochemistry

Whole-rock major and trace element analyses of the biotite monzo- to syenogranite, the muscovite-rich aplite of syenogranitic to alkali feldspar granitic composition, and the ME from the Rosa de Maio, Bandeirantes, and Maués intrusions are presented in Table 4.2.

Biotite granites are acidic (69-74.5 wt.% SiO_2), while aplites are strongly acidic (72-76 wt.% SiO_2), and the ME are intermediate to acidic (65-71 wt.% SiO_2, Table 4.2). These rocks are peraluminous to strongly peraluminous (A/CNK ratios > 1.1, Sylvester, 1998; Fig. 4.6A, Table 4.2) and display a slight positive correlation between A/CNK values and SiO_2 contents (Table 4.2). The biotite granites are high-K calc-alkalic, the aplites are predominantly high-K alkali-calcic, and the ME are calcic to calc-alkalic (Figs. 4.6B and D). Most of these rocks are

ferroan rocks, with $FeO_t/(FeO_t+MgO)$ values between 0.70 and 0.93 (Fig. 4.6C). In the Y+Nb vs. Rb tectonic discrimination diagram by Pearce et al. (1984), the biotite granites and the ME plot in the post-collision granites field (Pearce, 1996), whereas the aplites plot in the syn-collision granites field (Fig. 4.6E). Samples of all rock types display low Sr/Y (0.4-19.2), La/Yb (1.4-12.6), and Dy/Yb (0.9-1.9) ratios (Table 4.2).

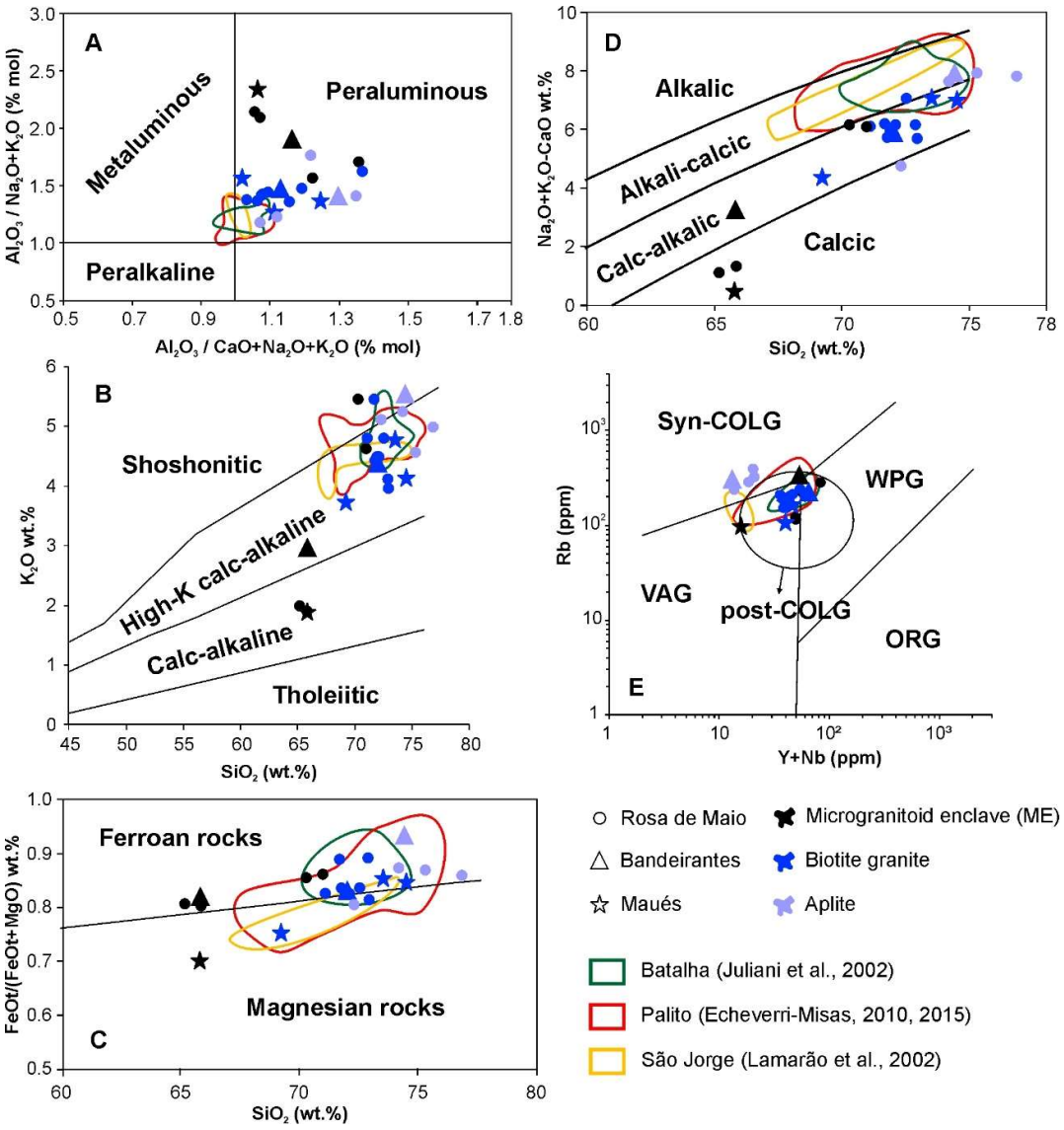

Figure 4.6 – Major and trace element data of the ME, the biotite granite, and the muscovite-rich aplite from the Rosa de Maio, Bandeirantes, and Maués intrusions. A) Al-saturation index diagram (Shand, 1927). B) SiO_2 vs. K_2O diagram (Peccerillo and Taylor, 1976). C) Fe-index diagram by Frost and Frost (2008). D) Modified alkali-lime index (MALI) diagram by Frost and Frost (2008). E) Y+Nb vs. Rb tectonic discrimination diagram by Pearce et al. (1984) with the post-COLG field by Pearce (1996). Contours represent data of the Batalha, Palito, and younger São Jorge host rocks from Juliani et al. (2002), Echeverri Misas (2010, 2015), and Lamarão et al. (2002), respectively.

When considered collectively, samples from the biotite granite, the muscovite-rich aplite, and the ME display a linear trend in Harker diagrams (Figs. 4.7 and 4.8), despite a gap in silica contents between ~66-70 wt.%. Strong inverse correlations are observed between SiO_2 and MgO, Al_2O_3, CaO, Fe_2O_3, MnO, TiO_2, Nb, V, Ni, Sc, Cu, Zn, as well as Cu/Au, Ni/As, and Eu/Eu* ratios (Figs. 4.7 and 4.8), whereas weaker inverse correlations occur between SiO_2 and P_2O_5, Sr, and the Co/Bi ratio (Figs. 4.7 and 4.8). In contrast, SiO_2 shows a positive correlation with Na_2O, K_2O, Ba, LREE, Th, and Zr, with weaker positive correlations observed for Au, As, and Ce/Ce* ratios (Figs. 4.7 and 4.8). Additionally, SiO_2 displays a convex trend with Rb and HREE, characterized by an initial positive correlation followed by a negative correlation (Figs. 7 and 8). In the aplites, Ba, Rb, LREE, Th, HREE, and Zr deviate from these trends (Figs. 4.7 and 4.8).

The biotite granites and the ME display sloping LREE (enrichment factors of over 100 times the chondrite) and flat HREE patterns (Fig. 4.9A), with $(La/Yb)_N$ ratios ranging from 4.74 to 8.47 and 4.93 to 6.81 (Table 4.2), respectively. The biotite granites display pronounced negative Eu anomalies (Fig. 4.9A) with Eu/Eu* ratios between 0.36 and 0.58 (Table 4.2), whereas the ME display less pronounced negative Eu anomalies (Fig. 4.8A) with Eu/Eu* ratios ranging from 0.39 to 0.86 (Table 4.2). Among the ME samples, only one displays an inconspicuous negative Eu anomaly (Eu/Eu* = 0.86, Fig. 4.9A) and a significantly lower total REE content when compared to the average content of the ME group (Fig. 4.9A, Table 4.2). The muscovite-rich aplites display considerably lower total REE contents in comparison to the total REE contents of biotite granites and the ME (Fig. 4.9A, Table 4.2). The aplites exhibit a slight enrichment in LREE and a flat HREE pattern, except for Yb and Lu (Fig. 4.9A), with $(La/Yb)_N$ ratios between 0.91 and 1.55 (Table 4.2). They display pronounced to strongly pronounced negative Eu anomalies (Fig. 4.9A) with Eu/Eu* ratios between 0.04 and 0.29 (Table 4.2).

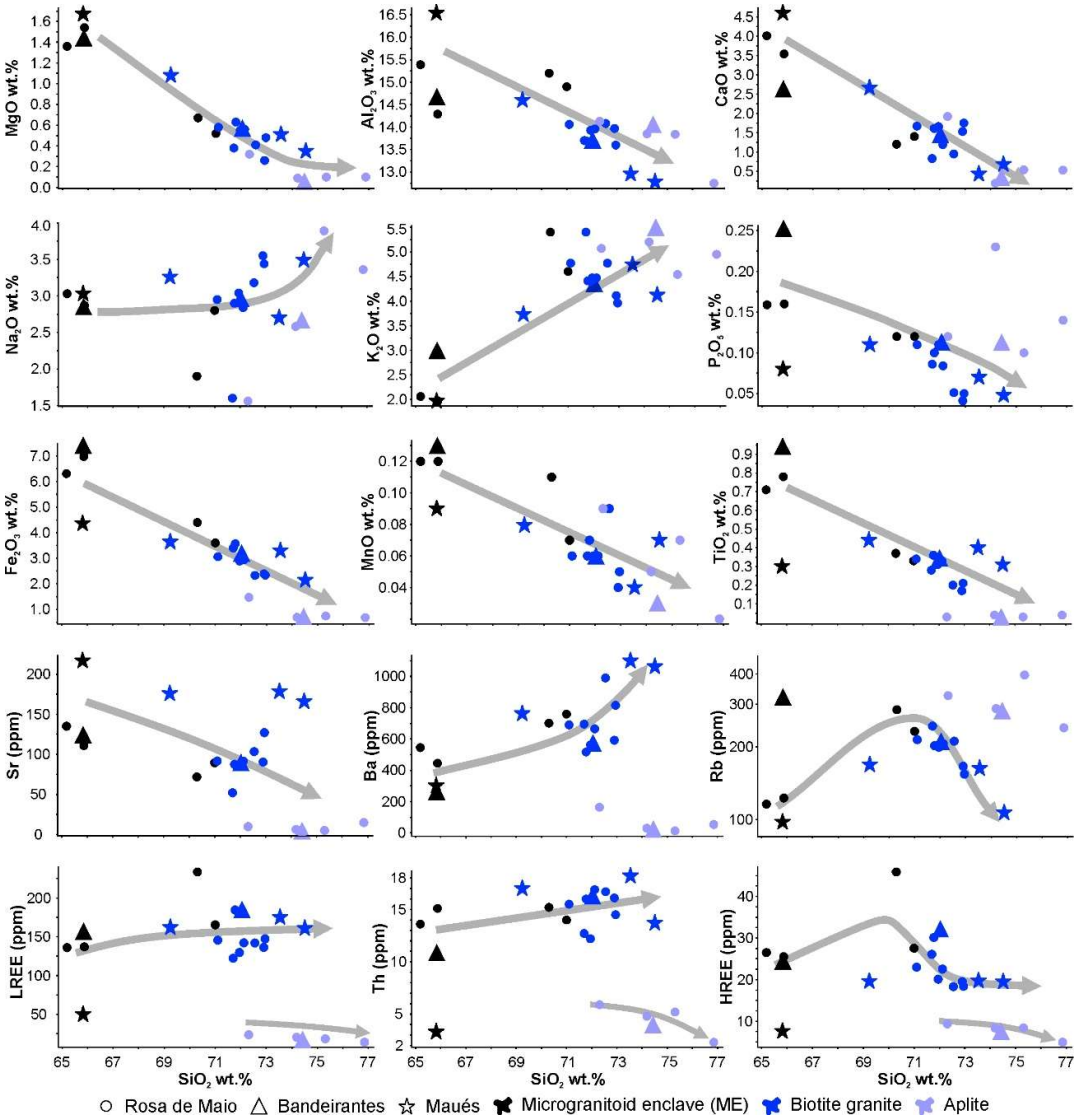

Figure 4.7 – Harker diagrams displaying major and trace element data of the ME, the biotite granite, and the muscovite-rich aplite from the Rosa de Maio, Bandeirantes, and Maués intrusions. Gray arrows indicate positive and negative correlation trends between SiO_2 and the respective oxide/element.

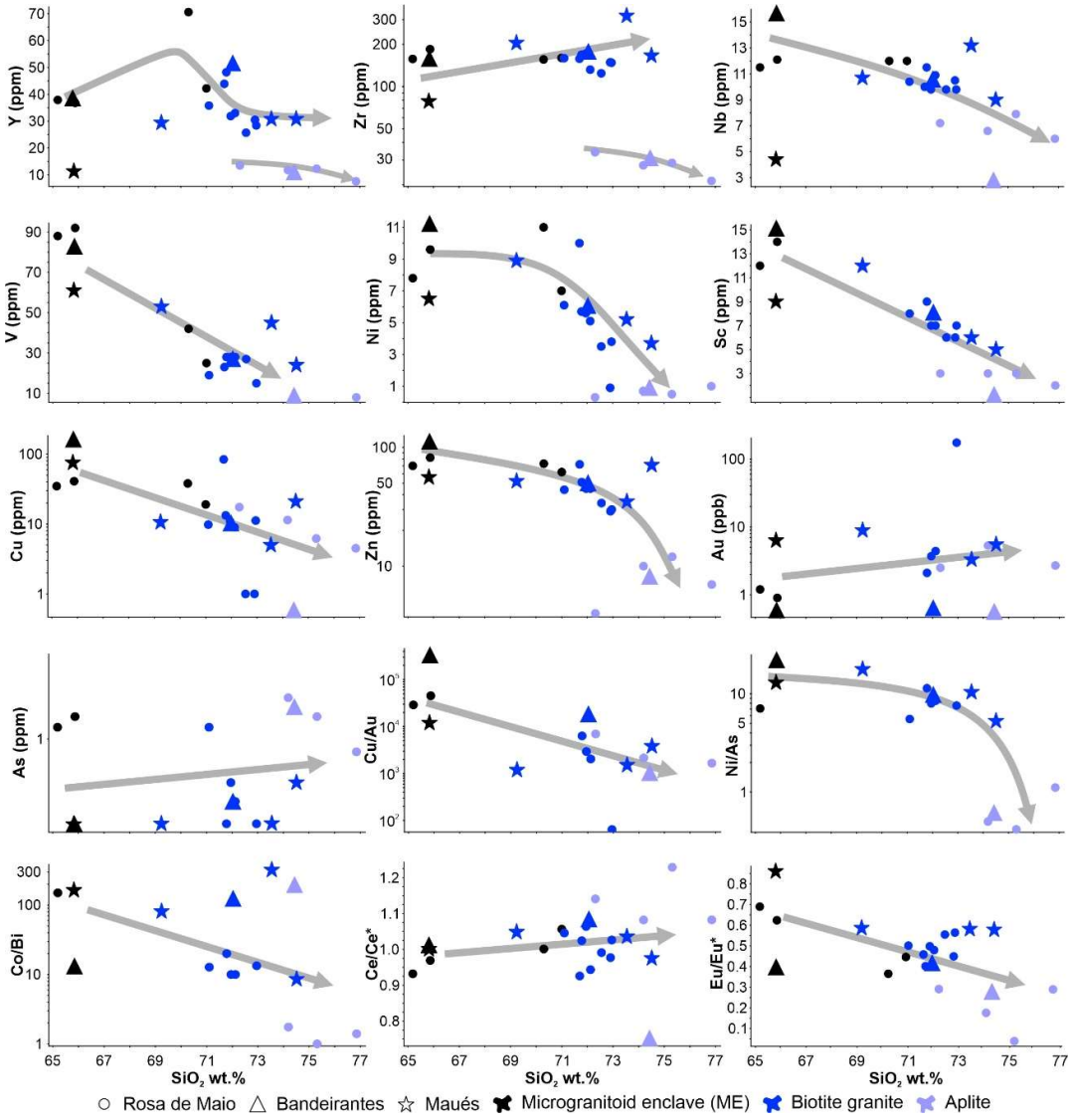

Figure 4.8 – Harker diagrams displaying trace element data of the ME, the biotite granite, and the muscovite-rich aplite from the Rosa de Maio, Bandeirantes, and Maués intrusions. Gray arrows indicate positive and negative correlation trends between SiO_2 and the respective element or element ratio.

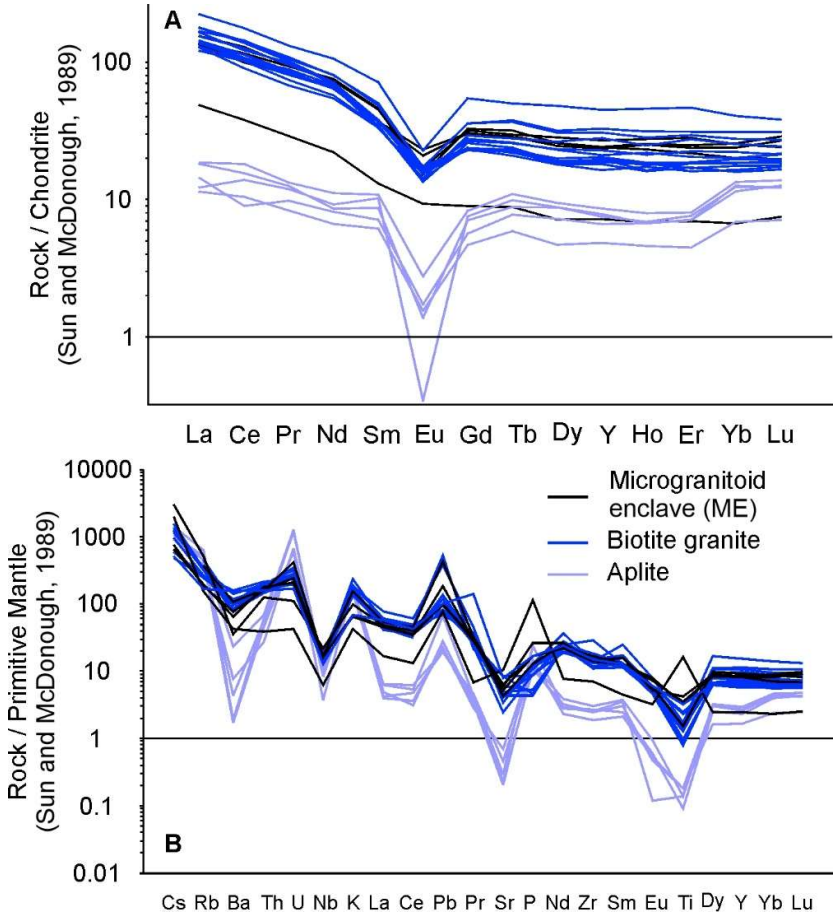

Figure 4.9 – Trace element data of the ME, the biotite granite, and the muscovite-rich aplite from the Rosa de Maio, Bandeirantes, and Maués intrusions. A) and B) REE and multielement patterns normalized to the chondrite and primitive mantle values of Sun and McDonough (1989), respectively.

The biotite granites and the ME commonly contain slightly higher concentrations of LILE and HFSE when compared to the muscovite-rich aplites, with the exception of Cs, Rb, U, K, and P (Fig. 4.9B). The biotite granites and the ME display negative Ba, Nb, Sr, and Ti anomalies, as well as a minor positive Pb anomaly in multielement diagrams (Fig. 4.9B). Within the ME samples, only one sample displays prominent positive P and Ti anomalies (Fig. 4.9B). The aplites display pronounced negative Ba, Nb, La, Ce, Sr, and Ti anomalies, along with a slight positive U anomaly (Fig. 4.9B).

Table 4.2 – Whole-rock major and trace element analyses of the ME, the biotite granite, and the muscovite-rich aplite from the Rosa de Maio[(1)], Bandeirantes[(2)], and Maués[(3)] intrusions.

	Microgranitoid enclaves (ME)						Biotite monzo- to syenogranite				
	LC-A-8[(1)]	R-91[(3)]	MAG-BD-5[(2)]	LC-A-9[(1)]	ELRM-R-219[(1)]	ELRM-R-218[(1)]	R-61[(3)]	RM-2[(1)]	LCRM-R-99[(1)]	MAG-RM-1[(1)]	RM-12[(1)]
SiO_2	65.19	65.82	65.84	65.87	70.30	71.00	69.24	71.10	71.70	71.78	71.95
TiO_2	0.71	0.30	0.93	0.78	0.37	0.33	0.44	0.34	0.28	0.36	0.31
Al_2O_3	15.39	16.54	14.67	14.29	15.20	14.90	14.60	14.06	13.70	13.69	13.93
Fe_2O_3	6.31	4.36	7.29	6.98	4.40	3.60	3.64	3.06	3.40	3.57	2.89
MnO	0.12	0.09	0.13	0.12	0.11	0.07	0.08	0.06	0.06	0.07	0.06
MgO	1.36	1.68	1.44	1.54	0.67	0.52	1.08	0.58	0.38	0.63	0.55
CaO	4.01	4.60	2.59	3.54	1.20	1.40	2.68	1.67	0.83	1.61	1.66
Na_2O	3.03	3.03	2.83	2.87	1.90	2.80	3.26	2.95	1.60	2.90	3.04
K_2O	2.06	1.98	2.95	1.97	5.40	4.60	3.73	4.77	5.40	4.41	4.47
P_2O_5	0.16	0.08	0.25	0.16	0.12	0.12	0.11	0.11	0.09	0.10	0.11
LOI	1.50	1.30	0.90	1.70	1.09	0.64	0.90	1.20	0.84	0.70	0.90
Total	99.84	99.78	99.82	99.82	100.76	99.98	99.76	99.90	98.28	99.82	99.87
A/CNK	1.061	1.068	1.168	1.075	1.363	1.228	1.023	1.077	1.372	1.098	1.083
La	31.8	11.5	32.9	30.6	52.7	36.6	36.4	32.4	30.2	42.3	28.6
Ce	60.8	23.2	70.8	62.1	108.0	78.9	77.4	69.3	55.2	86.9	62.2
Pr	7.8	2.8	8.8	7.9	12.5	8.9	9.1	7.9	6.4	10.3	7.0
Nd	30.0	10.3	35.2	30.7	49.4	34.0	33.2	30.3	25.4	37.3	26.7
Sm	5.7	2.0	7.0	5.6	10.9	6.9	5.8	5.6	5.1	7.7	5.2
Eu	1.3	0.5	0.9	1.2	1.3	1.0	1.0	0.9	0.8	1.0	0.8
Gd	6.2	1.8	6.7	6.2	11.2	6.5	4.9	5.5	6.0	7.4	4.9
Tb	1.1	0.3	1.2	1.1	1.9	1.1	0.9	1.0	1.0	1.4	0.9
Dy	6.5	1.8	6.5	6.2	12.2	7.2	4.7	5.9	6.7	7.8	5.1
Ho	1.4	0.4	1.3	1.4	2.6	1.6	1.0	1.2	1.4	1.6	1.1
Er	4.1	1.2	3.6	3.9	7.7	4.6	3.0	3.7	4.5	4.9	3.1
Tm	0.7	0.2	0.6	0.7	1.1	0.6	0.5	0.5	0.7	0.8	0.5
Yb	4.4	1.1	3.4	4.1	6.9	4.3	3.1	3.8	4.3	4.7	3.4
Lu	0.7	0.2	0.5	0.7	1.0	0.6	0.5	0.5	0.6	0.7	0.5
ΣREE	200.4	68.6	217.1	199.3	350.0	235.1	210.9	204.3	192.3	262.8	181.7
$(La/Yb)_N$	4.934	6.809	6.512	5.100	5.155	5.745	7.875	5.801	4.741	6.075	5.763
Eu/Eu*	0.690	0.861	0.392	0.624	0.365	0.446	0.586	0.501	0.459	0.402	0.498
Ce/Ce*	0.930	0.993	1.000	0.960	1.013	1.052	1.026	1.043	0.954	1.002	1.055
Cs	5.9	15.5	23.4	5.2	-	-	7.6	12.3	-	10.4	9.6
Rb	116.0	97.7	321.1	122.9	285.0	232.0	168.8	214.3	244.0	202.5	199.2
Ba	545.0	301.0	249.0	445.0	701.0	759.0	762.0	690.0	695.0	517.0	562.0
Th	13.6	3.3	10.7	15.1	15.2	14.0	17.0	15.5	12.7	16.0	12.2
U	8.6	0.9	2.3	4.4	5.2	5.1	5.4	5.8	5.3	5.9	4.5
Nb	11.5	4.4	15.6	12.1	12.0	12.0	10.7	10.4	10.0	11.5	9.8
Ta	0.9	0.8	1.3	1.0	1.2	1.0	0.8	1.1	1.2	1.1	1.1
Pb	7.1	1.9	6.7	13.0	27.0	30.0	7.3	6.7	-	4.8	6.7
Sr	135.0	216.7	124.1	110.8	71.7	89.4	175.8	91.6	51.9	87.3	85.4
Zr	157.4	78.5	158.5	184.8	156.0	160.0	204.8	159.4	158.0	168.7	171.8
Y	37.9	11.3	37.6	36.8	70.6	42.2	29.4	35.8	43.9	48.2	31.9
Hf	4.7	2.4	4.2	5.5	5.0	5.0	6.1	5.3	4.0	5.3	5.3
Sc	12.0	9.0	15.0	14.0	-	-	12.0	8.0	-	9.0	7.0
Ga	16.3	17.3	21.0	16.3	19.0	18.0	16.6	16.7	16.0	15.4	17.4
Ni	7.8	6.5	11.1	9.6	11.0	7.0	8.9	6.1	10.0	5.7	5.6
V	88.0	61.0	82.0	92.0	42.0	25.0	53.0	19.0	23.0	28.0	28.0
Co	15.0	49.0	29.0	17.6	-	-	8.1	5.1	-	6.0	4.0
Au (ppb)	1.2	6.3	0.5	0.9	-	-	8.9	<0.5	-	2.1	3.7
As	1.1	0.5	0.5	1.2	-	-	0.5	1.1	-	0.5	0.7
Cu	34.8	75.3	157.3	40.9	38.0	19.0	10.6	9.8	84.0	13.3	10.9
Mo	0.7	1.6	0.6	0.9	10.0	<2	0.2	0.8	4.0	1.9	0.5

Bi	0.1	0.3	2.2	<0.1	-	-	0.1	0.4	-	0.3	0.4
Zn	70.0	56.0	109.0	82.0	73.0	62.0	52.0	44.0	72.0	51.0	45.0
Sr/Y	3.6	19.2	3.3	3.0	1.0	2.1	6.0	2.6	1.2	1.8	2.7
La/Yb	7.3	10.1	9.6	7.6	7.6	8.5	11.7	8.6	7.0	9.0	8.5
Dy/Yb	1.5	1.6	1.9	1.5	1.8	1.7	1.5	1.6	1.6	1.7	1.5

Table 4.2 – Cont. Whole-rock major and trace element analyses of the ME, the biotite granite, and the muscovite-rich aplite from the Rosa de Maio[(1)], Bandeirantes[(2)], and Maués[(3)] intrusions.

	Biotite monzo- to syenogranite							Muscovite-rich aplite				
	MAG BD-3[(2)]	LCRM-R-87[(1)]	LC-A-10[(1)]	EL-A-1[(1)]	MAG RM-15[(1)]	MAG MA-10[(3)]	ELMA-R-19[(3)]	RM-8[(1)]	RM-17[(1)]	MAG BD-7[(2)]	RM-3[(1)]	RM-10[(1)]
SiO_2	72.03	72.12	72.55	72.90	72.95	73.54	74.51	72.31	74.19	74.43	75.31	76.85
TiO_2	0.33	0.33	0.20	0.17	0.21	0.40	0.31	0.03	0.04	0.02	0.03	0.04
Al_2O_3	13.71	13.96	14.08	13.97	13.60	12.96	12.78	14.13	13.85	14.01	13.84	12.75
Fe_2O_3	3.07	2.94	2.33	2.39	2.34	3.30	2.14	1.47	0.69	0.63	0.74	0.68
MnO	0.06	0.06	0.09	0.04	0.05	0.04	0.07	0.09	0.05	0.03	0.07	0.02
MgO	0.56	0.56	0.41	0.26	0.48	0.51	0.35	0.32	0.09	0.04	0.10	0.10
CaO	1.41	1.19	0.95	1.53	1.75	0.43	0.68	1.92	0.19	0.30	0.54	0.53
Na_2O	2.94	2.84	3.18	3.55	3.44	2.70	3.49	1.56	2.58	2.63	3.89	3.36
K_2O	4.31	4.47	4.77	4.11	3.96	4.74	4.12	5.07	5.20	5.43	4.54	4.95
P_2O_5	0.11	0.08	0.05	0.04	0.05	0.07	0.05	0.12	0.23	0.11	0.10	0.14
LOI	1.30	1.30	1.20	0.90	1.00	1.00	1.30	3.00	2.90	2.30	0.90	0.60
Total	99.83	99.85	99.81	99.86	99.83	99.69	99.80	100.02	100.01	99.93	100.06	100.02
A/CNK	1.136	1.196	1.162	1.069	1.036	1.252	1.117	1.224	1.355	1.303	1.126	1.076
La	39.7	32.7	32.3	30.7	33.9	42.0	38.9	4.4	4.3	3.4	2.9	2.7
Ce	87.9	63.8	65.9	62.4	69.7	84.3	74.5	11.1	9.5	5.5	8.5	6.4
Pr	10.0	8.4	7.9	7.7	8.2	9.6	9.4	1.3	1.2	0.9	1.1	0.8
Nd	37.7	31.6	30.8	30.2	29.8	33.4	32.2	5.2	4.0	3.8	4.3	3.1
Sm	7.4	5.7	5.1	5.3	5.6	5.7	5.7	1.7	1.3	1.1	1.6	0.9
Eu	1.0	0.9	0.9	0.8	1.0	1.0	1.0	0.2	0.1	0.1	0.0	0.1
Gd	7.3	5.7	4.8	5.3	4.7	4.7	4.9	1.7	1.5	1.2	1.6	1.0
Tb	1.4	1.0	0.8	0.9	0.8	0.8	0.8	0.4	0.3	0.3	0.4	0.2
Dy	8.1	5.8	4.6	4.8	4.6	4.7	4.7	2.4	2.2	1.8	2.2	1.2
Ho	1.8	1.2	1.0	1.0	0.9	1.0	0.9	0.5	0.4	0.4	0.4	0.3
Er	5.2	3.4	2.7	2.8	2.8	3.1	3.0	1.3	1.3	1.2	1.2	0.7
Tm	0.8	0.6	0.5	0.5	0.4	0.5	0.5	0.3	0.2	0.3	0.2	0.1
Yb	5.3	3.4	2.8	3.0	2.7	3.4	3.2	2.3	2.1	2.0	2.1	1.2
Lu	0.8	0.5	0.4	0.5	0.4	0.6	0.5	0.4	0.3	0.3	0.3	0.2
ΣREE	265.6	197.7	185.9	186.3	194.0	225.5	211.0	46.5	40.5	32.6	39.1	26.5
$(La/Yb)_N$	5.094	6.454	7.814	6.930	8.475	8.462	8.309	1.303	1.382	1.177	0.915	1.558
Eu/Eu*	0.416	0.480	0.555	0.449	0.564	0.582	0.578	0.291	0.176	0.272	0.039	0.290
Ce/Ce*	1.064	0.925	0.995	0.979	1.008	1.009	0.938	1.135	1.011	0.744	1.130	1.055
Cs	9.0	10.6	9.8	4.7	4.7	3.8	4.0	8.3	7.5	9.0	11.1	7.1
Rb	210.5	206.5	211.2	166.4	154.2	164.1	106.8	326.0	288.1	281.8	396.8	239.9
Ba	566.0	665.0	990.0	592.0	815.0	1099.0	1062.0	164.0	30.0	12.0	13.0	54.0
Th	16.2	16.9	16.7	16.1	14.5	18.2	13.7	5.9	4.8	3.8	5.2	2.3
U	7.2	6.7	5.2	5.2	4.1	4.9	3.5	26.1	12.3	13.4	24.6	14.2
Nb	10.5	10.9	9.8	10.5	9.8	13.2	9.0	7.2	6.6	2.7	7.9	6.0
Ta	1.6	0.9	0.9	0.9	1.3	1.7	0.8	2.5	2.2	1.3	1.9	2.5
Pb	5.9	9.7	8.4	5.6	6.7	5.9	38.3	1.4	4.7	2.0	1.4	1.6
Sr	89.4	91.4	103.3	90.3	126.9	178.4	165.8	9.6	6.1	4.3	4.9	14.7
Zr	173.1	132.1	124.4	148.9	148.0	319.6	166.2	34.1	27.5	29.8	28.6	21.3
Y	51.4	33.0	25.7	30.5	28.4	30.8	30.8	13.5	11.8	10.4	12.3	7.6
Hf	5.7	4.1	3.9	5.1	4.8	9.1	4.5	2.6	2.1	2.1	2.4	1.3
Sc	8.0	7.0	6.0	6.0	7.0	6.0	5.0	3.0	3.0	1.0	3.0	2.0
Ga	16.7	14.3	14.3	15.1	15.3	15.5	13.3	16.7	14.3	14.1	15.8	14.3
Ni	5.9	5.1	3.5	0.9	3.8	5.2	3.7	0.3	0.7	0.8	0.5	1.0

V	27.0	28.0	27.0	<8	15.0	45.0	24.0	<8	<8	8.0	<8	8.0
Co	37.3	5.0	6.0	2.0	45.4	64.1	6.0	0.6	0.7	39.2	0.4	0.7
Au (ppb)	0.6	4.4	<0.5	<0.5	174.3	3.3	5.5	2.5	5.3	0.5	<0.5	2.7
As	0.6	0.6	<0.5	<0.5	0.5	0.5	0.7	<0.5	1.4	1.3	1.2	0.9
Cu	10.4	9.0	1.0	1.0	11.2	5.0	21.0	17.4	11.4	0.5	6.2	4.5
Mo	0.3	0.2	0.2	0.2	0.4	0.3	0.6	1.0	0.3	0.4	0.4	2.8
Bi	0.3	0.5	<0.1	<0.1	3.4	0.2	0.7	3.1	0.4	0.2	0.4	0.5
Zn	49.0	45.0	34.0	29.0	30.0	35.0	71.0	4.0	10.0	8.0	12.0	7.0
Sr/Y	1.7	2.8	4.0	3.0	4.5	5.8	5.4	0.7	0.5	0.4	0.4	1.9
La/Yb	7.5	9.6	11.6	10.3	12.6	12.5	12.3	1.9	2.0	1.7	1.4	2.3
Dy/Yb	1.5	1.7	1.6	1.6	1.7	1.4	1.5	1.1	1.1	0.9	1.0	1.0

4.4.3 Mineral chemistry

Representative chemical analyses of biotite from the RMG are presented in Table 4.3.

Biotite is widespread in the RMG (particularly the biotite monzo- to syenogranite), being commonly the only mafic mineral in the primary assemblage, and occurs as euhedral to subhedral lamellae in the porphyric texture. Biotite from all rock types in the RMG is classified as annite, following the classification scheme proposed by Tischendorf et al. (2007). It displays Mg# values ranging from 22 to 26 in the aplites, from 22 to 36 in the biotite granites, and from 30 to 39 in the ME (Table 4.3). Based on the discrimination criteria of Nachit et al. (2005), biotite from all rock types is classified as primary or reequilibrated, forming a reequilibration trend characterized by a progressive decrease in TiO_2 concentrations (Fig. 4.10A). Moreover, according to the discrimination criteria of Abdel-Rahman (1994), biotite from the RMG displays compositions similar to those of biotite in peraluminous suites (Fig. 4.10B).

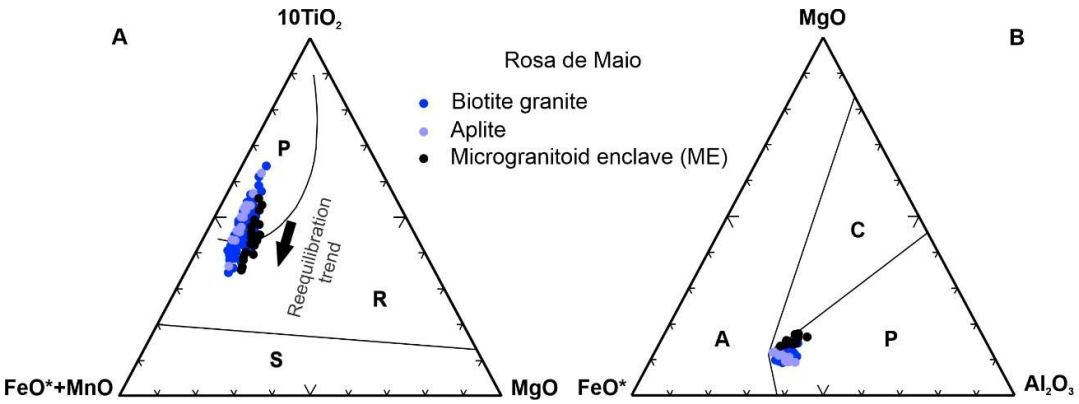

Figure 4.10 – Chemical composition of biotite from the RMG, including the ME, the biotite granite, and the muscovite-rich aplite. A) Biotite discrimination diagram by Nachit et al. (2005). P = primary, R = reequilibrated, and S = secondary/neoformed. The black arrow indicates the reequilibration trend. B) Biotite discrimination diagram by Abdel-Rahman (1994) based on magmatic affinity. A = anorogenic alkaline suites, C = calc-alkaline orogenic suite, and P = peraluminous suites.

Table 4.3 – Representative EPMA analyses (wt.%) and formulae (apfu) of biotite from the RMG. ΣT = tetrahedral site; ΣM = octahedral site; ΣI = interlayer site; ΣA = anionic site.

	Microgranitoid enclaves (ME)				Biotite monzo- to syenogranite					Muscovite-rich aplite			
SiO_2	34.43	34.97	34.84	34.14	36.99	35.68	34.77	35.67	32.92	34.40	35.00	35.03	34.36
TiO_2	2.51	2.86	3.16	4.02	2.06	2.95	5.45	2.40	3.07	3.36	2.72	3.30	2.36
Al_2O_3	16.52	16.47	15.80	15.38	16.26	15.87	15.25	16.96	17.26	16.02	16.48	17.83	17.27
FeO	22.32	22.82	24.74	25.74	22.27	23.74	24.39	25.82	27.39	25.81	25.47	24.39	25.53
MnO	0.27	0.55	0.42	0.50	0.40	0.66	0.35	0.53	0.43	0.73	0.66	0.75	0.68
MgO	8.06	7.75	7.08	6.46	7.09	6.39	5.57	4.89	4.39	5.10	4.82	4.23	4.23
CaO	0.06	0.02	0.02	0.03	0.01	0.05	0.03	0.03	0.01	0.02	0.02	0.01	0.02
BaO	0.41	0.47	0.34	0.69	0.59	0.72	0.77	0.02	0.16	0.66	0.26	0.31	0.45
Na_2O	0.07	0.08	0.08	0.13	0.08	0.13	0.04	0.14	0.09	0.10	0.22	0.14	0.12
K_2O	9.04	9.12	8.88	8.78	9.34	8.85	9.10	9.59	9.70	9.39	9.22	9.63	9.66
F	0.47	0.65	0.27	0.25	0.39	0.56	0.87	0.22	0.58	0.56	0.13	0.80	0.34
Cl	0.04	0.03	0.01	0.02	0.10	0.21	0.06	0.00	0.02	0.01	0.01	0.00	0.03
Total	94.18	95.78	95.64	96.13	95.55	95.81	96.65	96.26	96.02	96.16	95.02	96.42	95.04
apfu on a 11 O basis with total Fe as Fe^{2+}													
Si	2.743	2.755	2.744	2.704	2.886	2.827	2.760	2.797	2.654	2.753	2.781	2.769	2.757
Al^{IV}	1.257	1.245	1.256	1.296	1.114	1.173	1.240	1.203	1.346	1.247	1.219	1.231	1.243
ΣT	4.000	4.000	4.000	4.000	4.000	4.000	4.000	4.000	4.000	4.000	4.000	4.000	4.000
Al^{VI}	0.293	0.285	0.211	0.140	0.381	0.308	0.187	0.364	0.294	0.264	0.324	0.430	0.390
Ti	0.150	0.169	0.187	0.239	0.121	0.176	0.325	0.142	0.186	0.202	0.162	0.196	0.142
Mg	0.957	0.910	0.832	0.762	0.824	0.755	0.659	0.571	0.527	0.608	0.571	0.499	0.505
Fe^{2+}	1.487	1.504	1.630	1.705	1.453	1.573	1.619	1.693	1.847	1.727	1.693	1.613	1.713
Mn	0.018	0.037	0.028	0.034	0.026	0.044	0.024	0.035	0.030	0.049	0.044	0.050	0.046
ΣM	2.909	2.910	2.899	2.889	2.809	2.856	2.821	2.809	2.897	2.851	2.804	2.795	2.805
Ca	0.005	0.002	0.002	0.003	0.001	0.004	0.002	0.002	0.001	0.002	0.002	0.001	0.002
Ba	0.013	0.014	0.010	0.021	0.018	0.022	0.024	0.001	0.005	0.021	0.008	0.010	0.014
Na	0.011	0.012	0.013	0.019	0.012	0.020	0.006	0.021	0.013	0.016	0.033	0.021	0.019
K	0.919	0.916	0.892	0.887	0.929	0.895	0.921	0.959	0.998	0.959	0.935	0.971	0.989
ΣI	0.947	0.944	0.917	0.931	0.960	0.942	0.954	0.983	1.017	0.997	0.979	1.002	1.024
OH	1.877	1.834	1.931	1.936	1.890	1.832	1.774	1.946	1.850	1.857	1.965	1.798	1.910
Cl	0.006	0.004	0.002	0.002	0.013	0.028	0.008	0.000	0.003	0.001	0.001	0.001	0.004
F	0.117	0.162	0.067	0.061	0.096	0.140	0.218	0.054	0.147	0.142	0.034	0.201	0.085
ΣA	2.000	2.000	2.000	2.000	2.000	2.000	2.000	2.000	2.000	2.000	2.000	2.000	2.000
Mg#	39.17	37.70	33.79	30.90	36.20	32.43	28.93	25.23	22.20	26.05	25.24	23.61	22.78

4.4.4 Mössbauer spectroscopy on biotite

The results of Mössbauer spectroscopy and estimated proportions of Fe^{2+} and Fe^{3+} in biotite from surface and drill core samples of the RMG are presented in Table 4.4.

The spectra of all samples were well resolved by considering three quadrupole doublets (Fig. 4.11), one doublet assigned to the Fe^{2+} species (Db1) and two doublets to the Fe^{3+} species (Db2 and Db3, Fig. 4.11). All spectra are characterized by a predominant doublet associated with Fe^{2+} (Db1) and two less pronounced doublets associated with Fe^{3+} (Db2 and Db3). These doublets overlap, forming a first intensified peak, followed by a second small peak, and a third peak mostly due to Db1 (Fig. 4.11). These spectra are typical of biotite containing both Fe^{2+} and Fe^{3+} (Dyar, 2002).

Two groups of biotite are identified based on the relative abundances of Fe (Table 4.4). The first group is composed of 5 samples and displays values for Fe^{2+} and Fe^{3+} between 71-74% and 26-29%, respectively (Table 4.4), while the second group consists of two samples with calculated values of 82% for Fe^{2+} and 18% for Fe^{3+} (Table 4.4). In all samples, Fe^{2+} clearly dominates over Fe^{3+}.

Table 4.4 – Estimated proportions of Fe^{2+} and Fe^{3+} in magmatic biotite of the RMG, determined using Mössbauer spectroscopy analyses.

Sample	Rock type	Oxidation state	Linewidth (mm/s)	Isomer shift* (mm/s)	Quadrupole Splitting (ΔE_Q, mm/s)	Percentage (%)
MAG-RM-1	Biotite granite	Fe^{2+}	0.49	1.15	2.44	74
		Fe^{3+}	0.43	0.32	0.90	13
		Fe^{3+}	0.30	-0.02	0.53	13
RM-DD1-67.10-67.60 m	Biotite granite	Fe^{2+}	0.44	1.12	2.46	73
		Fe^{3+}	0.37	0.23	0.89	12
		Fe^{3+}	0.27	-0.04	0.41	15
RM-DD1-92.20-92.56 m	Biotite granite	Fe^{2+}	0.41	1.13	2.48	74
		Fe^{3+}	0.44	0.30	0.87	12
		Fe^{3+}	0.25	-0.05	0.35	14
RM-DD2-110.40-110.64 m	Biotite granite	Fe^{2+}	0.47	1.14	2.47	82
		Fe^{3+}	0.36	0.26	0.96	11
		Fe^{3+}	0.25	-0.04	0.42	7
RM-DD2-213.30-213.67 m	Biotite granite	Fe^{2+}	0.42	1.14	2.55	73
		Fe^{3+}	0.30	0.27	0.98	8
		Fe^{3+}	0.33	-0.02	0.33	19
RM-DD3-133.83-133-98 m	Biotite granite	Fe^{2+}	0.44	1.11	2.48	71
		Fe^{3+}	0.44	0.33	0.91	13
		Fe^{3+}	0.30	-0.05	0.33	16
RM-DD3-155.13-155.23 m	Biotite granite	Fe^{2+}	0.47	1.14	2.49	82
		Fe^{3+}	0.40	0.29	1.02	12
		Fe^{3+}	0.21	-0.01	0.49	6

*: In relation to Fe-α.

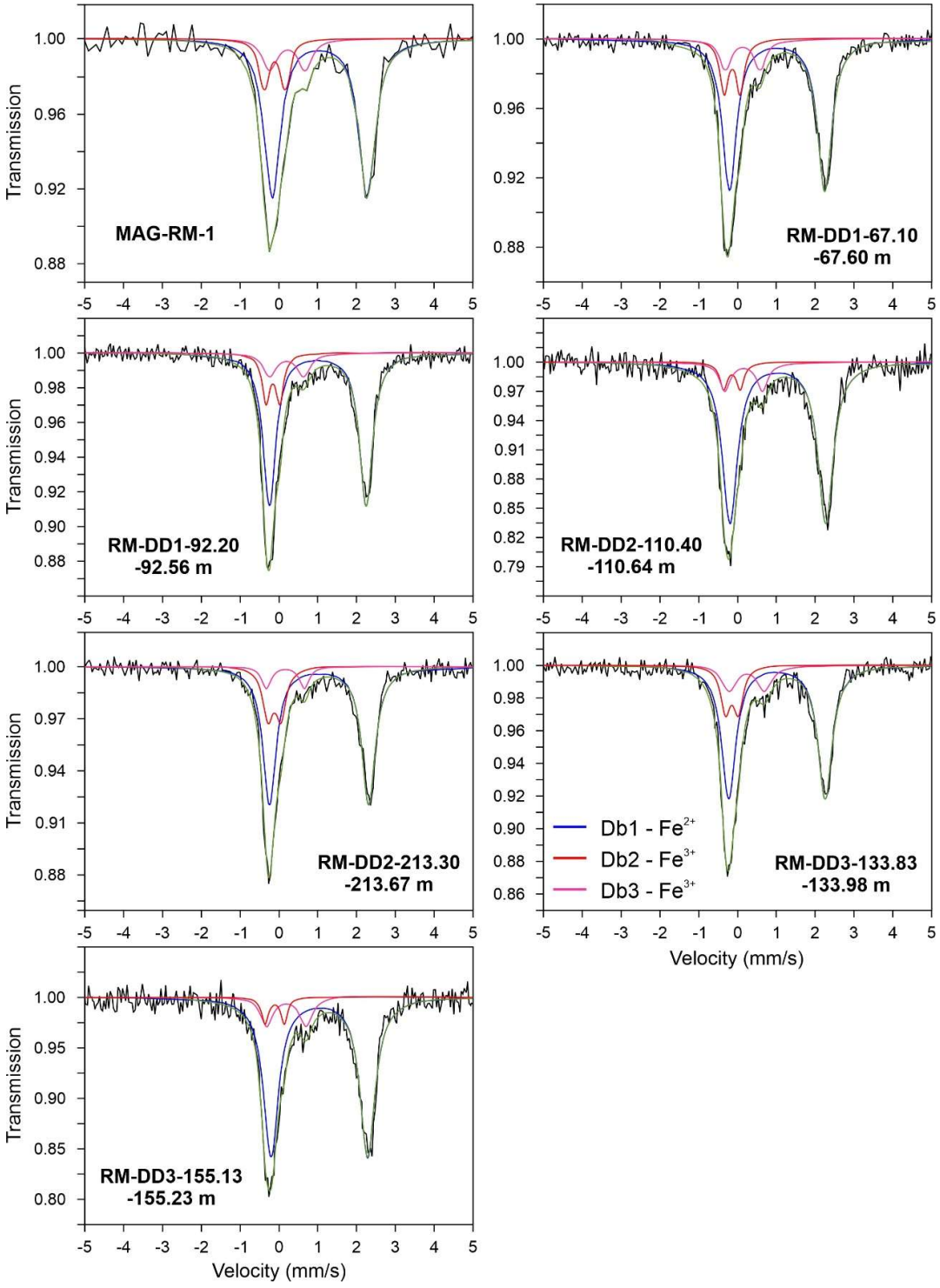

Figure 4.11 – Mössbauer spectra of biotite from the biotite granite of the RMG, including surface and drill core samples. All spectra are characterized by a dominant doublet for Fe^{2+} (blue) and two subordinated doublets for Fe^{3+} (red and pink). Black lines represent measured data, whereas green curves represent the best data fit. Blue, red, and pink curves correspond to the best fits for doublets Db1, Db2, and Db3, respectively.

4.4.5 U-Pb geochronology

4.4.5.1 Zircon

U-Pb LA-ICP-MS analyses were carried out on zircon from two samples of the RMG (biotite monzo- and syenogranite) and one sample of the Bandeirantes intrusion (biotite monzogranite). These analyses are presented in the Appendix A. Interpretations are based on both Concordia and weighted mean $^{207}Pb/^{206}Pb$ ages. In all samples, discordant zircon grains from different populations define overlapping Discordias (Fig. 4.13). Since these populations cannot be reliably distinguished either texturally or using the available mineral chemistry, Discordia dates are avoided. Instead, Concordia dates are calculated using zircon grains with 95-105% concordance. Furthermore, weighted mean Pb-Pb dates are preferred over weighted mean $^{206}Pb/^{238}U$ dates, as they are not affected by recent Pb loss.

Rosa de Maio Granite

Zircon crystals from sample MAG-RM-1 (biotite monzogranite) are euhedral to subhedral, colorless and transparent, occurring as short and long bipyramidal prisms ranging in size from 180 μm to 475 μm, with length/width ratios between 1.4 and 3.8 (Fig. 4.12A). Cathodoluminescence (CL) images show typical magmatic growth zoning, occasionally mantling darker cores. Inclusions are rare and metamorphic rims are absent (Fig. 4.12A). Thirty-five concordant to discordant grains form a well-constrained Discordia with an upper intercept at *ca.* 1890 Ma and a poorly constrained Discordia with an upper intercept at *ca.* 2030 Ma. Both Discordias have lower intercepts at 0 Ma, suggesting recent Pb loss (Fig. 4.13A). Ten concordant grains (95-105% conc.) from the 1890 Ma cluster yield a Concordia age of 1889.5 ± 4.7 Ma (MSWD = 1.4, n=10, Fig. 4.13A) and a weighted mean $^{207}Pb/^{206}Pb$ date of 1894.2 ± 9.2 Ma (MSWD = 1.7, n=10, Fig. 4.13B), both interpreted as representing the crystallization age of the RMG. Concordant grains yielding dates of *ca.* 2030 Ma are interpreted as xenocrysts. In CL images, these grains are often unmantled and display oscillatory zoning (Fig. 4.12A). The Th/U ratios for all analyses range from 0.2 to 4.3 (Appendix A).

Zircon crystals from sample MAG-RM-16A (biotite syenogranite) are also euhedral to subhedral, colorless, and transparent bipyramidal prisms with sizes

ranging from 120 μm to 360 μm and length/width ratios between 2.2 and 6 (Fig. 4.12B). In CL images, they also display typical magmatic growth zoning, occasionally mantling darker cores. Inclusions are rare and metamorphic rims are absent (Fig. 4.12B). Among 34 analyses, 16 concordant grains (95-105% conc.) yield ages of *ca.* 2120 Ma, 2030 Ma, and 1890 Ma (Fig. 4.13C). Most of the remaining discordant grains define a Discordia with an upper intercept corresponding to the *ca.* 1890 Ma cluster and a lower intercept at 0 Ma (Fig. 4.13C), also suggesting recent Pb loss. Twelve concordant grains (95-105% conc.) from the 1890 Ma cluster yield a Concordia age of 1885.6 ± 4.2 Ma (MSWD = 0.33, n=12, Fig. 4.13C) and a weighted mean $^{207}Pb/^{206}Pb$ date of 1889 ± 11 Ma (MSWD = 0.49, n=12, Fig. 4.13D), both interpreted as representing the crystallization age of the RMG. Concordant grains with dates of *ca.* 2120 Ma and 2030 Ma are interpreted as inherited zircon. In CL images, they occur both as darker cores mantled by newly grown zircon or as unmantled prismatic grains displaying oscillatory zoning (Fig. 4.12B). The Th/U ratios of all grains are between 0.3 and 2.4 (Appendix A).

Bandeirantes Intrusion

In sample MAG-BD-1 (biotite monzogranite), zircon crystals are euhedral, colorless with yellowish hues, and transparent bipyramidal prisms with sizes ranging from 130 μm to 610 μm and length/width ratios between 1.4 and 6.5 (Fig. 4.12C). CL images reveal typical magmatic growth zoning, with rare inclusions and no metamorphic rims (Fig. 4.12C). Among 26 analyses, 21 concordant grains (95-105% conc.) yield dates of *ca.* 2190 Ma, 2060 Ma, 1970 Ma, and 1910 Ma (Fig. 4.13E). Thirteen concordant grains (95-105% conc.) from the 1910 Ma cluster yield a Concordia date of 1908.4 ± 3.7 Ma (MSWD = 0.4, n=13, Fig. 4.13E) and a weighted mean $^{207}Pb/^{206}Pb$ date of 1906.7 ± 8.8 Ma (MSWD = 1.2, n=13, Fig. 4.13F), both interpreted as the crystallization age of the Bandeirantes intrusion. Older concordant grains with dates of *ca.* 2190 Ma, 2060 Ma, and 1970 Ma are interpreted as xenocrysts (Fig. 4.13E). In CL images, these grains commonly display oscillatory zoning and are occasionally mantled by darker rims (Fig. 4.12C). The remaining five discordant grains form a Discordia with an upper intercept at the *ca.* 1970 Ma cluster and a lower intercept at 0 Ma (Fig. 4.13E),

suggesting recent Pb loss. The Th/U ratios of all grains are between 0.4 and 4.1 (Appendix A).

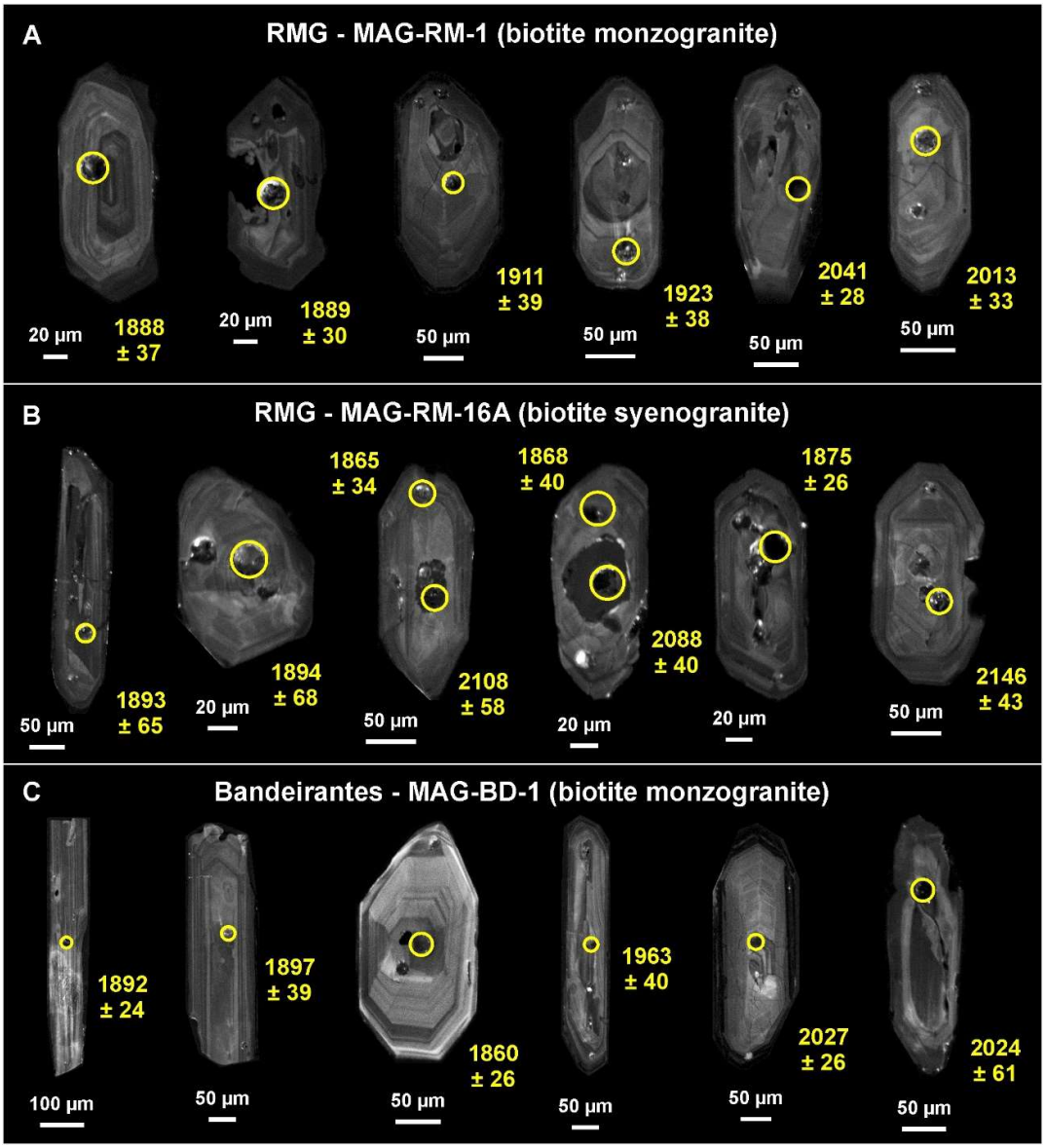

Figure 4.12 – Cathodoluminescence (CL) images of representative zircon grains from biotite granites of the Rosa de Maio (samples MAG-RM-1 and MAG-RM-16A) and Bandeirantes (sample MAG-BD-1) intrusions, along with their corresponding $^{207}Pb/^{206}Pb$ dates. Spot sizes are 25 µm.

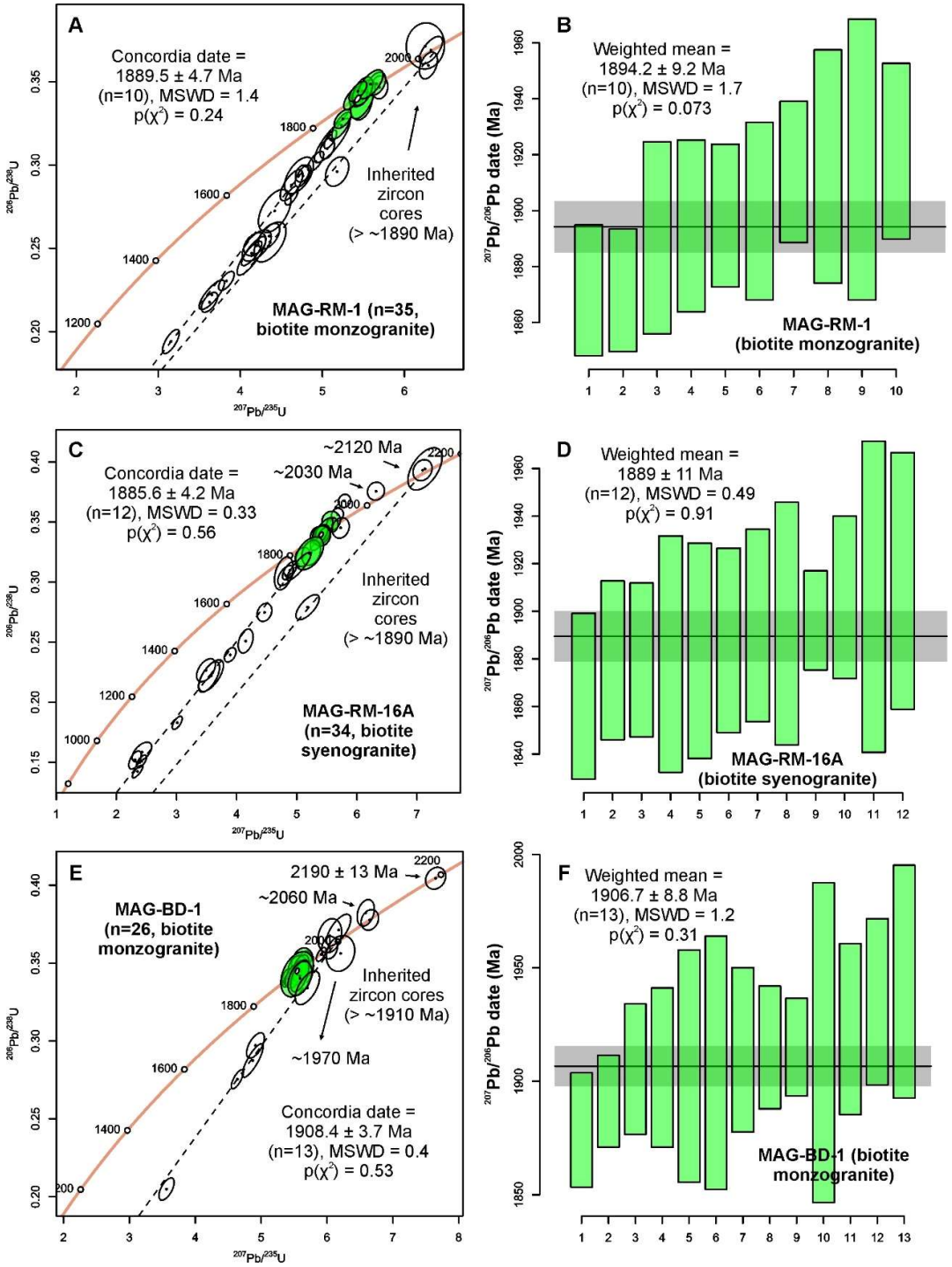

Figure 4.13 – Wetherill Concordia diagrams (zircon data) and weighted mean $^{207}Pb/^{206}Pb$ dates for biotite granites from the Rosa de Maio (MAG-RM-1 and MAG-RM-16A) and Bandeirantes (MAG-BD-1) intrusions. Due to the overlap of discordant grains from different populations, Discordia dates are not determined. Instead, Concordia ages are calculated using grains with 95-105% concordance. n = number of analyses, MSWD = mean square weighted deviation, and $p(\chi^2)$ = probability of fit.

4.4.5.2 Monazite

U-Pb LA-ICP-MS analyses were carried out on monazite from one sample of the RMG (biotite monzogranite). These analyses are presented in the Appendix A.

Monazite crystals from sample MAG-RM-1 (biotite monzogranite) are anhedral, light yellow, and transparent, displaying several granular shapes. Grain sizes range from 230 µm to 670 µm. In the RMG granites, monazite typically occurs as inclusions within magmatic biotite and frequently contains very fine-grained biotite inclusions. All 23 analyzed grains, both concordant and discordant, form a single population. These grains define a Discordia with an upper intercept at 1885 ± 13 Ma (MSWD = 0.98, n=23, Fig. 4.14A) and a lower intercept at 0 ± 0.1 Ma, suggesting recent Pb loss. Additionally, they yield a weighted mean $^{207}Pb/^{206}Pb$ date of 1886 ± 13 Ma (MSWD = 0.95, n=23, Fig. 4.14B). Both the upper intercept date and the Pb-Pb date are interpreted as the crystallization age of the RMG.

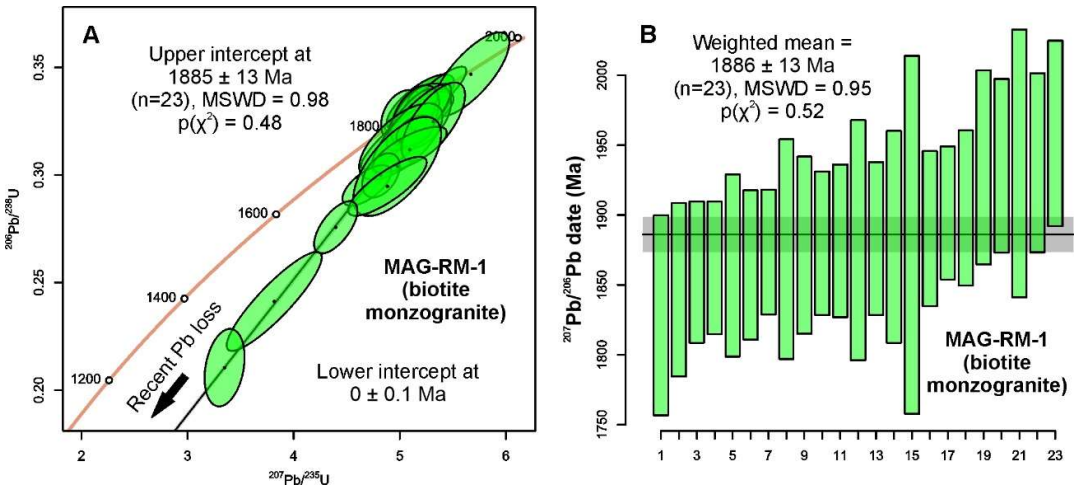

Figure 4.14 – Wetherill Concordia diagram (monazite data) and weighted mean $^{207}Pb/^{206}Pb$ date for a biotite monzogranite (MAG-RM-1) from the RMG. n = number of analyses, MSWD = mean square weighted deviation, and $p(\chi^2)$ = probability of fit.

4.4.6 Sm-Nd isotope geochemistry

Sm-Nd isotope analyses of the RMG are presented in Table 4.5. The crystallization age of 1890 Ma (rounded mean age obtained from zircon U-Pb data in this work) is used for εNd calculations. The biotite monzo- to syenogranite yields both positive and negative εNd (1890 Ma) values within a fairly narrow

interval, ranging from +1.04 to -1.94 (Table 4.5). In addition, the biotite granite yields T_{DM} model ages in a similarly narrow range, between 2.11 Ga and 2.42 Ga (Table 4.5). These data are summarized in Figure 4.16.

Table 4.5 – Sm-Nd isotope data of the biotite granite from the RMG.

Unit	Sample	Rock type	Sm (ppm)	Nd (ppm)	$^{147}Sm/^{144}Nd$	$^{143}Nd/^{144}Nd \pm 2SE$	εNd (T)	T_{DM} (Ga)	T (Ma)
Rosa de Maio Granite (RMG)	RM 1	Biotite granite	5.20	24.91	0.1263	0.511762 ± 11	0.00	2.22	1890
	RM 2		6.11	30.53	0.1210	0.511707 ± 6	0.20	2.19	1890
	RM 7		6.03	29.09	0.1253	0.511727 ± 5	-0.45	2.26	1890
	RM 9		6.08	29.58	0.1242	0.511717 ± 7	-0.38	2.25	1890
	RM 11		3.42	15.39	0.1342	0.511827 ± 11	-0.66	2.32	1890
	RM 12		5.61	27.04	0.1255	0.511735 ± 6	-0.35	2.25	1890
	RM 13		6.65	32.64	0.1232	0.511702 ± 6	-0.42	2.25	1890
	RM 14		6.47	32.05	0.1220	0.511690 ± 8	-0.38	2.24	1890
	RM 15		6.43	32.02	0.1214	0.511693 ± 8	-0.18	2.22	1890
	RM 19		11.02	51.29	0.1299	0.511708 ± 4	-1.94	2.42	1890
	ELRM-R-070		2.25	11.45	0.1185	0.511719 ± 10	1.04	2.11	1890

4.5 Discussions

4.5.1 Magmatic system

4.5.1.1 The role of fractional crystallization

The biotite granite and muscovite-rich aplite from the Rosa de Maio, Bandeirantes, and Maués intrusions represent high-silica (69-76 wt.% SiO_2), peraluminous to strongly peraluminous, high-K calc-alkalic, and ferroan granitic magmas. Descending linear trends of MgO, Fe_2O_3, MnO, Al_2O_3, CaO, P_2O_5, TiO_2, Nb, V, Sc, and Eu/Eu* values in Harker diagrams (Figs. 4.7 and 4.8) suggest that fractional crystallization of biotite, plagioclase, apatite, magnetite, and ilmenite played an important role in the progressive depletion of these oxides/elements during chemical differentiation of those granitic magmas. Additionally, the ascending linear trends of K_2O, Na_2O, and Ba fit with the increasing modal proportions of microcline and progressively lower An contents of plagioclase. The increasing trends of LREE, Th, and Zr (Figs. 4.7 and 4.8) are interpreted as the result of increasing modal proportions of monazite and zircon, whereas the convex trend of HREE suggests that these elements remained incompatible until the onset of extensive xenotime crystallization, which led to their subsequent depletion (Figs. 4.7 and 4.8).

The muscovite-rich aplite is richer in silica (72-76 wt.% SiO_2), displays the lowest contents of MgO, CaO, Fe_2O_3, MnO, and TiO_2, and represents the most evolved member of this magmatic series. In fact, the aplite displays modal proportions of muscovite up to 15%, the lowest An contents of plagioclase (albite, $An_{0.5-6.5}$), and contains primary tourmaline, a phase expected to occur in more evolved rock types in a magmatic series. Furthermore, the aplite displays conspicuous lower REE contents (particularly LREE) and more pronounced negative Eu anomalies (Fig. 4.9A), probably due to the fractionation of monazite (it occurs predominantly in the biotite granite), xenotime, and plagioclase, respectively. The multielement pattern of the aplite mimics that of the biotite granite, except for its depletion in REE, Ti, Zr, Sr, and Ba (Fig. 4.9B), most likely due to early crystallization of monazite, xenotime, ilmenite, zircon, and plagioclase, respectively, in the biotite granite, leaving out a residual melt depleted in those elements.

The occurrence of the muscovite-rich aplite as centimeter- to decimeter-scale dykes crosscutting the biotite granite suggests that they formed as an evolved, water-rich granitic magma ascending trough fractures, likely partitioning mobile elements, and leaving behind less mobile or immobile elements. This process could explain its higher Rb contents and lower Ba, REE, Th, and Zr concentrations compared to the biotite granite (Figs. 4.7 and 4.8). Thus, petrography and geochemical data suggest that fractional crystallization was the dominant process promoting differentiation from biotite granite to aplite.

4.5.1.2 Microgranitoid enclaves: xenoliths, products of basic vs. acidic magma hybridization, or autoliths?

The ME could be interpreted as xenoliths, as products of interaction between coeval basic magma injected into the acidic magma reservoir (*e.g.*, Jayananda et al., 2014), or as stirred up cumulates (autoliths). The presence of xenoliths in the RMG is expected, given the known occurrence of the Jacareacanga Group in this region (Fig. 4.2) and the presence of zircon xenocrysts in RMG samples with dates between 2.0-2.1 Ga (Fig. 4.13). However, the biotite-rich schist enclaves (Fig. 4.3F), which are interpreted as true xenoliths (likely derived from the Jacareacanga Group, 2.2-2.0 Ga), are clearly

distinguished from the ME by their distinct tectonic foliation and dominant mica and quartz composition, whereas the ME display no deformation and have a tonalitic/granodioritic composition. These textural and compositional differences suggest that the ME are unlikely to represent xenoliths from surrounding wall rocks.

The ME could also represent globules of a basic and hotter magma interacting with an acidic magma which would be represented by the biotite granites. However, the hybridization required to produce intermediate to acidic compositions such as those of the ME would imply zones of magma mingling and mixing (Jayananda et al., 2014, Weinberg et al., 2021) which are not observed. The contact between the ME and the biotite granites is sharp (Figs. 4.3E, 4.3F, and 4.4I) and suggests that minimal exchange occurred between these melts. Moreover, enclaves containing crystals from the host felsic magma would be expected if the basic and acidic magmas interacted in the mushy state (Weinberg et al., 2021). This could be accounted for the presence of zoned plagioclase phenocrysts in both ME and the biotite granites (Figs. 4.4A, 4.4D, and 4.4H). However, the compositions of the plagioclase phenocrysts, which are expected to be approximately similar, are distinct. The ME display zoned plagioclase phenocrysts ranging from An_{32-43} (Fig. 4.4H), whereas the biotite granites display plagioclase phenocrysts ranging from An_{18-29} and An_{6-11} (Figs. 4.4A and 4.4D). Thus, the ME are unlikely to be products of hybridization between extraneous hotter basic magmas injected into an acidic magma reservoir.

Instead, this difference in An content of plagioclase phenocrysts is more compatible with previous crystallization of the ME belonging to the same magmatic series of the biotite and aplites (*i.e.*, autoliths). Moreover, when compared to the biotite granites, biotite from the ME is also classified as annite, displays the same reequilibration trend (Fig. 4.10A), the same peraluminous compositions (Fig. 4.10B), and the highest Mg# values (between 30 and 39). Also, An contents of plagioclase in the ME are the highest (An_{25-45}). All these characteristics are compatible with the ME being cogenetic to the biotite granite and aplite, comprising less evolved members of this magmatic series. Furthermore, the ME display REE and multielement patterns that mimic those of the biotite granites and aplites (Figs. 4.9A and 4.9B), except for one ME sample

with higher modal proportions of apatite and ilmenite that produce positive P and Ti anomalies in multielement diagrams (Fig. 4.9B). The less pronounced negative Eu anomalies of the ME (Fig. 4.9A) also suggest fractionation of plagioclase during chemical differentiation of this magmatic series. Therefore, the ME are interpreted as disrupted and stirred up cumulates or simply less evolved rocks (autoliths in both cases) that were transported to upper portions of the magma reservoir due to convective flow and/or chaotic mixing (*e.g.*, Vernon and Paterson, 2006; Weinberg et al., 2021). In this scenario, the ME represent or are similar to parental magmas from which the biotite granites and the more evolved muscovite-rich aplites are derived. During magmatic evolution, fractional crystallization was likely the most important process promoting differentiation from tonalitic and granodioritic magmas (ME) to monzo- and syenogranitic (biotite granites), and later alkali feldspar granitic magmas (muscovite-rich aplites).

4.5.1.3 Oxygen fugacity conditions

Oxygen fugacity of the biotite granites, the most abundant and voluminous rock type in the RMG, was estimated based on the results of Mössbauer spectroscopy on magmatic biotite. Recalculated compositions considering the estimated $Fe^{3+}/\Sigma Fe$ ratios (Table 4.4) indicate two groups of biotite granites, both plotting above the NNO buffer (Fig. 4.15, Wones and Eugster, 1965). One of the groups displays higher $Fe^{3+}/\Sigma Fe$ ratios (Fig. 4.15), with this increase in oxygen fugacity conditions being interpreted as the result of early crystallization of more reduced phases (*e.g.*, sulfides) during differentiation of those magmas. Additionally, the biotite granites are classified as magnetite-series rocks (>0.1 vol.% magnetite, Ishihara, 1977, 1981) and contain primary ilmenite with MnO concentrations between 3-16 wt.%, suggesting that more Mn^{2+} was incorporated into ilmenite when less Fe^{2+} was available (*i.e.,* higher $Fe^{3+}/\Sigma Fe$ ratios). Therefore, oxygen fugacity conditions of the RMG during its crystallization are estimated to have exceeded the NNO buffer, reaching even more oxidizing conditions after the crystallization of reduced phases. These changes in fO_2 of the biotite granites are interpreted to be reflected in varying $Fe^{3+}/\Sigma Fe$ ratios in biotite.

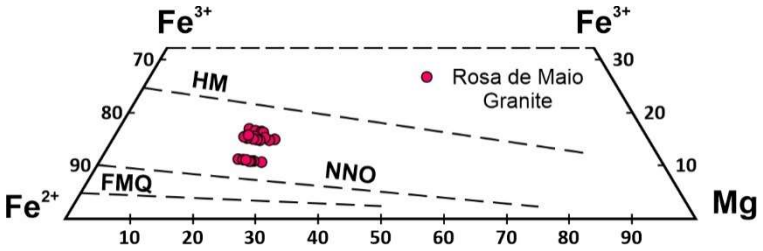

Figure 4.15 – Recalculated compositions of biotite from the RMG in the Fe^{3+}-Fe^{2+}-Mg ternary system of Wones and Eugster (1965). Estimates of Fe^{3+}/Fe^{2+} are based on the results of Mössbauer spectroscopy. Dashed lines represent oxygen buffers. FMQ = fayalite-magnetite-quartz; NNO = Ni-NiO, and HM = hematite-magnetite.

4.5.2 Ages, tectonic context, and magma sources

4.5.2.1 Crystallization ages of the Rosa de Maio and Bandeirantes intrusions

Zircon crystals from the two RMG samples (Figs. 4.13A to 4.13D) are characterized by prismatic, euhedral external morphologies and display internal concentric growth zoning, features typical of magmatic zircon (Fig. 4.12). Th/U ratios > 0.2 further support a magmatic origin, whether the zircon grains are inherited or crystallized directly from the melt. In addition, the absence of deformation in these rocks rules out a metamorphic origin for the analyzed zircon grains. In the two RMG zircon samples, the youngest zircon population, clustering at *ca.* 1890 Ma, is interpreted as the crystallization age of the RMG, with inheritance of older zircon populations dated between *ca.* 2.0-2.1 Ga. The presence of brighter rims disrupting the concentric oscillatory zoning of darker cores is also consistent with inheritance of zircon cores. Furthermore, the upper intercept and weighted mean Pb-Pb dates of 1885 ± 13 Ma and 1886 ± 13 Ma, respectively, obtained from a single monazite population in a RMG sample (Fig. 4.14), which consistently occurs as inclusions in magmatic biotite, also corroborate the crystallization of the RMG at *ca.* 1890 Ma. Thus, based on the Concordia and weighted mean $^{207}Pb/^{206}Pb$ dates from two zircon samples (Figs. 4.13A to 4.13D) and the Discordia and weighted mean $^{207}Pb/^{206}Pb$ dates from one monazite sample (Fig. 4.14), the crystallization age of the RMG is constrained to 1890 Ma. This is consistent with the crystallization ages of *ca.* 1880 Ma obtained by Santos et al. (2000, 2004).

Zircon crystals from the Bandeirantes sample are also characterized by prismatic, euhedral morphologies, internal oscillatory growth zoning, and Th/U ratios > 0.4, all of which are typical of magmatic zircon. The Bandeirantes granites are also undeformed, excluding a metamorphic origin for these zircon grains. In the Bandeirantes sample, the youngest zircon population, dated at *ca.* 1910 Ma, is interpreted as representing the crystallization age, while older zircon cores are interpreted as inherited, with ages of *ca.* 2190 Ma, 2060 Ma, and 1970 Ma. The youngest population yields Concordia and weighted mean Pb-Pb dates of 1908.4 ± 3.7 Ma and 1906.7 ± 8.8 Ma (Figs. 4.13E and 4.13F), respectively, interpreted as the age of crystallization of the Bandeirantes intrusion. Considering the uncertainties associated with the Pb-Pb dates, the Bandeirantes intrusion is coeval with or slightly younger than the RMG, suggesting that the PAR magmatism in this region persisted for a few million years.

Thus, the fertile PAR magmatism associated with the Au-mineralized magmatic-hydrothermal system that includes the Rosa de Maio and Bandeirantes deposits persisted for a few million years, from *ca.* 1907 to 1890 Ma. These ages are similar to those of the Batalha (1883 ± 4 Ma, Juliani et al., 2002), Palito (1883 ± 11 Ma, Aquino et al., 2013; Echeverri Misas, 2015), and younger São Jorge granites (1891 ± 3 Ma, Lamarão et al., 2002; Borges et al., 2009), which are also correlated with the PAR and associated with Au(-Cu) deposits. In a global context of Earth history, this fertile magmatism is coeval with the assembly of the Columbia supercontinent between 2.0-1.8 Ga (Santosh and Groves, 2022). In terms of gold metallogeny associated with convergent margins, this period coincides with the formation of giant orogenic gold systems in West Africa between *ca.* 2160-2030 Ma, whereas porphyry Cu-Au provinces were far less common (Santosh and Groves, 2022). Given the limited preservation of mid- to upper-crustal magmatic-hydrothermal deposits of this age (*ca.* 1.90-1.88 Ga; Santosh and Groves, 2022), these deposits of the TMP represent valuable examples of Au-rich magmatic-hydrothermal deposits that can provide important insights into the role of the supercontinent cycle in Paleoproterozoic metallogeny.

4.5.2.2 Tectonic setting in the context of the TMP

The time span between 1907-1890 Ma places the RMG and Bandeirantes magmatism within the mid to late stages of the tectonic and petrologic evolution of the TMP (Santos et al., 2001, 2004; Cassini et al., 2020). During this period, the tectonic regime transitioned from a subduction-controlled evolved magmatic arc (represented by the OMS) to a late- to post-collisional setting represented by the YMS (Cassini et al., 2020, 2022). The YMS was started by the generation of the high-K calc-alkaline to shoshonitic magmatism of the PAR, including the Rosa de Maio, Bandeirantes, and Maués intrusions, as well as the Batalha, Palito, and younger São Jorge granites (Fig. 4.6B). Moreover, the trace element compositions of all these intrusions indicate a post-collisional setting (Fig. 4.6E).

4.5.2.3 Sources of the RMG

The basement rocks of the RMG in this region are represented by the Jacareacanga Group (metavolcanic and metasedimentary rocks, 2.2-2.0 Ga; Santos et al., 2000, 2004) and the Cuiú-Cuiú Complex (orthogneisses, 2.04-1.99 Ga; Santos et al., 2000, 2004). The Cuiú-Cuiú Complex yields negative εNd(T) values ranging from -3.36 to -0.07 and T_{DM} model ages between 2.23 and 2.49 Ga (Fig. 4.16, Silva, 2017; Moreira, 2019; Alves et al., 2020). Partial melting exclusively of these rocks could not account for the relatively narrow range of εNd(T) values and T_{DM} model ages obtained for the RMG (Fig. 4.16, Table 4.5), while a pure mantle-derived source is also unlikely. In this case, the Nd isotope signature of the RMG instead suggests that the sources of this magmatism include contributions from both crustal rocks, such as the metamorphic rocks of the Jacareacanga Group (2.2-2.0 Ga) and orthogneisses of the Cuiú-Cuiú Complex (2.04-1.99 Ga), and juvenile material. In fact, two samples analyzed for U-Pb geochronology contain inherited zircon populations with dates between *ca.* 2030 and 2120 Ma (Figs. 4.13A and 4.13C). These inherited cores are interpreted as xenocrysts likely derived from source rocks similar to those of the Jacareacanga Group (2.2-2.0 Ga) and the Cuiú-Cuiú Complex (2.04-1.99 Ga). The presence of biotite-rich schist xenoliths and the peraluminous to strongly peraluminous character of the RMG further support contributions from metasedimentary rocks of the Jacareacanga Group.

Additionally, the Bandeirantes sample analyzed for U-Pb geochronology contains a zircon population dated at *ca.* 1970 Ma (Fig. 4.13E). These zircon cores are also interpreted as xenocrysts, possibly derived from rocks at depth analogous to the granitic rocks of the Creporizão Suite (1.99-1.95 Ga). Cassini et al. (2020) obtained εNd(T) values ranging from -2.99 to -1.78 and T_{DM} model ages between 2.3 and 2.4 Ga for this suite, except for one granodiorite with a lower εNd(T) value of -8.36 and a T_{DM} model age of 2.9 Ga (Fig. 4.16, Cassini et al., 2020). Moreover, syenites from the Creporizão Suite (1.97-1.95 Ga) yield higher εNd(T) values between -1.64 and +1.69 due to a stronger mantle contribution (Fig. 4.16, Cassini et al., 2020). Thus, considering the Nd isotope signature of the granitic rocks of the Creporizão Suite (Fig. 4.16), the latter may have also provided crustal inputs to the RMG magmas.

Therefore, the sources of the RMG are interpreted to have mixed contributions involving juvenile material and crustal rocks from the OMS, analogous to those of the Jacareacanga Group (2.2-2.0 Ga) and the Cuiú-Cuiú Complex (2.04-1.99 Ga). According to Cassini et al. (2022), the PAR magmatism (early pulses of the YMS) potentially remobilized Au-rich residual sulfides from a metasomatized SCLM and/or lower crust formed in previous magmatic events (*i.e.*, the OMS). This might be the case for the RMG magmas and would have contributed to their potential to form Au-rich magmatic-hydrothermal deposits.

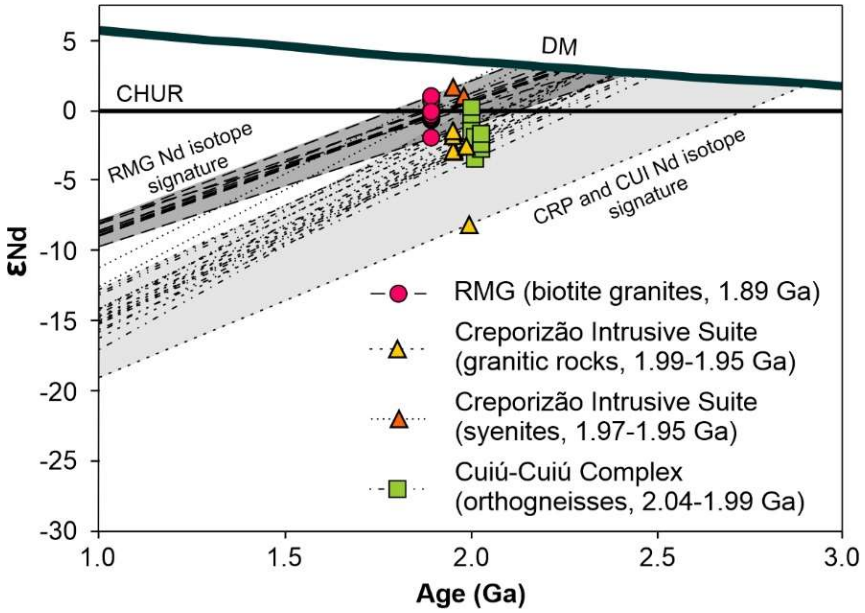

Figure 4.16 – Crystallization age vs. εNd evolution diagram of the RMG, Creporizão Suite (data from Cassini et al., 2020), and Cuiú-Cuiú Complex rocks (data from Silva, 2017; Moreira, 2019; and Alves et al., 2020). Note that the RMG displays a distinct Nd isotope signature compared to the Creporizão Suite and Cuiú-Cuiú Complex rocks from the basement. CRP = Creporizão Suite and CUI = Cuiú-Cuiú Complex.

4.5.3 Constraints on Au fertility

4.5.3.1 Similarities with Au-rich porphyry systems

Although the Rosa de Maio deposit shares some features with orogenic gold deposits — such as low Cu/Au ratios, occurrence within convergent margins (in this case, a continental arc), and structurally controlled gold mineralization hosted in sulfide-rich quartz veins (Groves et al., 1998) — it lacks several key characteristics that define typical orogenic gold systems. For instance, the formation of orogenic gold deposits is commonly associated with major crustal-scale fault zones and prograde metamorphism at greenschist to lower amphibolite facies conditions (Groves et al., 1998; Goldfarb and Groves, 2015). These features are absent in the RMG region. Moreover, orogenic gold deposits are not typically linked to magmatic-hydrothermal processes (Goldfarb and Groves, 2015; Groves et al., 2020; Goldfarb and Pitcairn, 2023), in contrast to the Rosa de Maio deposit, which shows evidence of a magmatic-hydrothermal origin. Hydrothermal activity at the RMG was triggered by the exsolution of high-temperature fluids during the late stages of magmatic evolution. These ore fluids and their associated alteration assemblages are directly linked to a causative

intrusion (i.e., the RMG), consistent with a magmatic-hydrothermal genetic model. Other granite-hosted gold deposits in the TMP that share similar characteristics with the Rosa de Maio deposit include the Batalha (Juliani et al., 2002), Tocantinzinho (Biondi et al., 2018; Lopes and Moura, 2019), and Palito (Echeverri Misas, 2015). In these deposits, hydrothermal evolution involved the exsolution of high-temperature, high-salinity ore fluids, also genetically associated with a causative intrusion, resulting in comparable hydrothermal alteration sequences (including an early potassic alteration stage). These deposits are also interpreted as belonging to magmatic-hydrothermal systems (Juliani et al., 2021).

Similarly, the Rosa de Maio deposit displays several characteristics commonly associated with IRGS. These features include Au-rich ores, a direct genetic link with a causative intrusion emplaced in a post-collisional tectonic setting, and gold mineralization hosted in sulfide quartz veins associated with sericitic alteration (Thompson et al., 1999; Lang and Baker, 2001; Hart, 2007). However, an essential characteristic of IRGS that is absent in the Rosa de Maio deposit is the reduced nature of the causative intrusion (Thompson et al., 1999; Lang and Baker, 2001; Hart, 2007). Thus, although the Rosa de Maio deposit shows some affinities with IRGS, it lacks an important feature that defines this deposit type.

Alternatively, the Rosa de Maio deposit also shares some similarities with low Cu/Au ratio ($<4\times10^4$, Kesler et al., 2002) porphyry-style systems. These porphyry systems are associated with low H_2O and high-K calc-alkaline to alkaline magmatism, shallow depths of formation and/or thin crusts, low Sr/Y (<50), La/Yb (<25), and Dy/Yb (<1.9) values of the associated magmatic rocks, and late- to post-collisional settings (Murakami et al., 2010; Chiaradia, 2015; 2020, 2022; Park et al., 2021; Hao et al., 2022). These characteristics are comparable to those of the high-K calc-alkaline to shoshonitic PAR magmatism that was emplaced in a post-subduction regime likely associated with asthenospheric upwelling and crustal thinning.

The low Sr/Y values of the RMG (<20, Table 4.2), interpreted as the result of extensive fractionation of plagioclase during its magmatic evolution, are

compatible with the evolution of Au-rich porphyry-style systems. In such systems, some authors propose that less hydrous magmas with plagioclase-dominant fractionation (preceding amphibole), emplaced at shallower depths and/or thin crusts, would lead to low Sr/Y values (Chiaradia et al., 2012; Chiaradia, 2015). Similarly, the low La/Yb (<13) and Dy/Yb (<2) values of the RMG align with the geochemical signatures of magmatic rocks associated with Au-rich porphyry deposits (Chiaradia, 2022). The higher Fe contents and lower-pressure magmatic differentiation of these systems would promote later sulfide saturation, ultimately forming Au-rich porphyry systems (Park et al., 2019, 2021; Chiaradia, 2022; Hao et al., 2022). In contrast, deep-seated hydrous magmas with amphibole-dominant fractionation, formed in long-lived subduction-related thick arcs, would lead to typical high Sr/Y, La/Yb, and Dy/Yb values (Chiaradia et al., 2012; Chiaradia, 2015, 2020, 2022). The early Fe depletion and higher-pressure magma evolution would promote earlier sulfide saturation, ultimately forming Cu-rich porphyry systems (Park et al., 2019, 2021; Chiaradia, 2022; Hao et al., 2022).

Therefore, the low Cu/Au ratios, high-K calc-alkaline character of relatively oxidized magmas, low Sr/Y, La/Yb, and Dy/Yb values, and the late- to post-collisional setting of the RMG magmatic-hydrothermal deposit suggest some similarities with Au-rich porphyry-style deposits. This implies that the metallogenetic models of these systems might be applied to understand the Au fertility of the RMG magmas.

4.5.3.2 The potential role of magmatic sulfide saturation

Some studies propose that late sulfide saturation helps maintain higher concentrations of chalcophile elements in the magmatic system until fluid exsolution occurs (Park et al., 2019, 2021; Hao et al., 2022). In cases where magmas experience fluid segregation prior to sulfide saturation, chances are increased that Au-rich porphyry systems will be formed (Park et al., 2019, 2021; Chiaradia, 2020; Hao et al., 2022). Other studies consider not only the timing of sulfide saturation but also the type of segregating sulfide phase as an important control on Cu/Au ratios of porphyry-style systems (Li and Audétat, 2013, 2015; Li et al., 2021; Hao et al., 2022). In arc magmas, sulfide saturation typically leads to the exsolution of an immiscible sulfide liquid (SL), followed by the precipitation of

monosulfide solid solution (MSS) as the dominant phase, along with minor amounts of a Cu-rich sulfide liquid from which intermediate solid solution (ISS) subsequently precipitates (Li and Audétat, 2012, 2013; Zhang and Audétat, 2017; Rottier et al., 2020; Li et al., 2021). The partition coefficients of Cu and Au between MSS and silicate melt (SM), as determined by Li and Audétat (2015) – with $D_{Cu}^{MSS/SM}$ values from 280 to 42000 and $D_{Au}^{MSS/SM}$ from 10 to 2000 – and by Li et al. (2021) – with $D_{Cu}^{MSS/SM}$ values from 530 to 1700 and $D_{Au}^{MSS/SM}$ from 140 to 270 (see silicate melt compositions and experimental conditions in Table 4.6) – demonstrate that precipitation of sulfide as MSS would have a higher impact in the removal of Cu than Au during magma evolution. Since nearly all arc magmas reach sulfide saturation (Georgatou and Chiaradia, 2020; Li et al., 2021) and MSS is expected to be the dominant phase, segregation of MSS would represent one of the factors controlling low Cu/Au ratios in porphyry-style systems.

The magmatic system of the RMG, as previously discussed, indicates that fractional crystallization was likely the most important process driving chemical differentiation during magmatic evolution. This, along with the descending linear trends of Cu/Au ratios in Harker diagrams (Fig. 4.8), suggests that fractionation of a sulfide phase progressively depleted Cu more than Au as the system evolved from tonalitic/granodioritic to monzonitic and alkali feldspar granitic magmas. Additionally, the decreasing trend of Co/Bi (Fig. 4.8) also suggests fractionation of a sulfide phase similar to MSS. Partition coefficients from Li and Audétat (2015) and Li et al. (2021) show that Co preferentially partitions into MSS ($D_{Co}^{MSS/SM}$ = 70-2500 and 55-260, respectively) over SL ($D_{Co}^{SL/SM}$ = 50-580 and 16-160, respectively, Table 4.6). In contrast, Bi preferentially partitions into SL ($D_{Bi}^{SL/SM}$ = 830-11000 and 140-3300, respectively) rather than MSS ($D_{Bi}^{MSS/SM}$ = 1-350, Table 4.6). Thus, the observed decrease in Co/Bi ratios during magmatic evolution supports fractionation of a sulfide phase equivalent to MSS. Similarly, the decreasing trend of Ni/As (Fig. 4.8) reflects preferential partitioning of strongly chalcophile elements (*e.g.*, Ni, Cu) into sulfide phases over relatively less chalcophile elements (*e.g.*, As, Au), further supporting the role of sulfide fractionation during magmatic evolution. Ultimately, this process would have led to lower Cu/Au budgets available for extraction by exsolved fluids during the

hydrothermal stage. We suggest that precipitation and fractionation of this sulfide phase would have partitioned Cu and Au relative to the silicate melt in a manner analogous to MSS, as discussed above. However, given the available data, it is not possible to determine whether the magmatic system remained sulfide-saturated throughout its entire evolution or to estimate the proportions of residual sulfides at each step of crystallization. Furthermore, the role of exsolved fluids in dissolving these magmatic sulfides (*e.g.*, Zhang and Audétat, 2017), thereby releasing metals into the hydrothermal system, cannot be assessed with current knowledge.

Table 4.6 – Partition coefficients (D) of Cu, Au, Co, Bi, Ni, and As between monosulfide solid solution (MSS), sulfide liquid (SL), and silicate melt (SM), as determined by Li and Audétat (2015) and Li et al. (2021). Li and Audétat (2015) – Silicate melt of basaltic to rhyolitic compositions at 900-1200 °C, 0.5-1.5 GPa, and oxygen fugacity ranging from ~FMQ-2 to FMQ+3. Li et al. (2021) – Silicate melt of basaltic to dacitic compositions at 1000-1200 °C, 0.5-1.0 GPa, and oxygen fugacity 1-1.5 log units above the FMQ buffer.

	Li and Audétat (2015)		*Li et al. (2021)*	
Element/ Partition coefficient (D)	$D^{MSS/SM}$	$D^{SL/SM}$	$D^{MSS/SM}$	$D^{SL/SM}$
Cu	280-42000	800-4600	530-1700	1100-8400
Au	10-2000	2000-29000	140-270	5700-90000
Co	70-2500	80-580	55-260	16-160
Bi	1-350	830-11000	-	140-3300
Ni	650-18000	2300-18000	-	-
As	0.2-30	20-180	-	<1-40

Therefore, we propose that the precipitation of sulfide phases (analogous to MSS) during the magmatic evolution of the RMG might have had a greater impact on removing Cu rather than Au, resulting in residual melts with low Cu/Au ratios. This could represent a first-order control on the Au endowment of the RMG mineralization. Clearly, more data are required to evaluate this hypothesis and to assess other magmatic and hydrothermal factors controlling Au fertility.

4.6 Conclusions

The results presented in this work indicate the following conclusions:

1. The Rosa de Maio, Bandeirantes, and Maués intrusions host magmatic-hydrothermal gold deposits in the northwestern portion of the Tapajós Mineral

Province. The associated magmatic rocks are high-silica, peraluminous to strongly peraluminous, high-K calc-alkaline, ferroan, and relatively oxidized granites;

2. Fractional crystallization played a crucial role in the magmatic evolution of these intrusions, leading to the following differentiation sequence: from biotite-rich tonalitic/granodioritic rocks to biotite monzo-/syenogranites, and finally to muscovite syeno-/alkali feldspar granitic aplites. The parental magmas from which the biotite granite and muscovite-rich aplite are derived have compositions similar to the microgranitoid enclaves. These enclaves were transported to upper portions of the magma reservoir due to convective and/or chaotic mixing. The occurrence of oscillatory zoning in plagioclase phenocrysts of the RMG rocks is likely the result of influx of fresh magma into this dynamic magma reservoir;

3. Oxygen fugacity conditions during crystallization of the biotite granites, the most abundant and voluminous rock type in the RMG, are estimated to have been above the NNO buffer;

4. The Parauari magmatism (onset of the younger magmatic sequence) in this region likely persisted for a few million years, represented by the high-K calc-alkaline to shoshonitic magmatism of the Bandeirantes and Rosa de Maio intrusions. They were emplaced at *ca.* 1907 Ma and 1890 Ma, respectively, in a late- to post-collisional setting within the context of the TMP tectonic evolution. This magmatism followed a period of subduction-controlled arc magmatism represented by the older magmatic sequence;

5. The sources of the RMG involve contributions from both juvenile material and crustal rocks from the older magmatic sequence similar to the Jacareacanga Group (2.2-2.0 Ga) and Cuiú-Cuiú Complex (2.04-1.99 Ga) rocks. This is reflected in zircon xenocrysts with ages around 2120-2190 Ma and 2030 Ma;

6. The Rosa de Maio magmatic-hydrothermal deposit shares similarities with Au-rich porphyry-style deposits, including low Cu/Au ratios, low Sr/Y, La/Yb, and Dy/Yb values of associated magmatic rocks, high-K calc-alkaline to shoshonitic character, and late- to post-collisional setting;

7. Magmatic sulfide saturation might have been a first-order control on the Au fertility of the Rosa de Maio primary deposit, although more data are clearly required to assess this hypothesis.

4.7 Acknowledgements

This study was financially supported by the Brazilian Council for Scientific and Technological Development (CNPq, grants 555063/2006-2 and 313172/2020-0) and the Coordenação de Aperfeiçoamento de Pessoal de Nível Superior – Brazil (CAPES, Finance Code 001). This work was also made possible by a scholarship granted by CNPq (168366/2018-5) to Pedro Victor F. de S. Alves. We thank Dr. Marly Babinski (Editor), Dr. M. Santosh (Reviewer), and two anonymous reviewers for their insightful and constructive comments and suggestions, which significantly contributed to improving the manuscript.

CAPÍTULO 5

GENESIS OF THE ROSA DE MAIO GOLD DEPOSIT, TAPAJÓS MINERAL PROVINCE, NORTHERN BRAZIL: HYDROTHERMAL EVOLUTION AND MINERALIZATION FROM GEOCHEMISTRY, MINERAL CHEMISTRY, $^{40}Ar/^{39}Ar$ GEOCHRONOLOGY, AND SULFUR ISOTOPES

5 GENESIS OF THE ROSA DE MAIO GOLD DEPOSIT, TAPAJÓS MINERAL PROVINCE, NORTHERN BRAZIL: HYDROTHERMAL EVOLUTION AND MINERALIZATION FROM GEOCHEMISTRY, MINERAL CHEMISTRY, $^{40}Ar/^{39}Ar$ GEOCHRONOLOGY, AND SULFUR ISOTOPES

Abstract

The Rosa de Maio deposit is a magmatic-hydrothermal gold deposit located in the northwestern Tapajós Mineral Province, within the south-central Amazonian Craton, northern Brazil. It is genetically linked to the Rosa de Maio Granite (*ca.* 1890 Ma), a high-K calc-alkaline and relatively oxidized intrusion associated with the late- to post-collisional continental arc magmatism of the Parauari Suite (1.89-1.87 Ga). Although the magmatic evolution of the deposit has recently been addressed, its hydrothermal evolution has not yet been investigated in detail. This study proposes that the Rosa de Maio deposit comprises two genetically related hydrothermal systems: a deeper system characterized by sodic, potassic, propylitic, and sericitic alteration, and a shallower, near-surface system marked by sericitic alteration and the development of a quartz stockwork system. Gold mineralization occurs in both systems, hosted within sericitic alteration zones and sulfide-rich quartz veins. In all cases, gold shows a consistent spatial association with sulfides, particularly pyrite. Muscovite from a quartz vein in the shallower system yielded a $^{40}Ar/^{39}Ar$ plateau age of 1808.3 ± 7.1 Ma, interpreted either as the result of isotopic resetting during a younger thermal event or as evidence of a younger mineralizing magmatism not yet identified in the area. Sulfur isotope analyses of pyrite from both systems yielded $\delta^{34}S$ values between +0.5 and +1.3‰, consistent with a dominantly magmatic sulfur source. Overall, the deeper system of the Rosa de Maio deposit shares several similarities with Au-rich porphyry-style deposits, whereas the shallower system likely represents a superimposed epithermal mineralization, now largely eroded.

5.1 Introduction

Multiple Au(-Cu) deposits in the Tapajós Mineral Province (TMP), located in the south-central Amazonian Craton (Fig. 5.1), are included in porphyry-epithermal systems (Juliani et al., 2005; Echeverri Misas, 2015; Cassini, 2016;

Borgo et al., 2017; Lopes and Moura, 2019; Juliani et al., 2021; Cassini et al., 2022), intrusion-related-gold-systems (IRGS, Santos et al., 2001; Villas et al., 2013), and hybrid systems combining IRGS and Au-rich porphyry features (Juliani et al., 2002; Borges et al., 2009; Biondi et al., 2018). These deposits are mostly associated with continental arc and post-collisional magmatism of the Tapajós-Parima Orogen (2.04-1.87 Ga, Santos et al., 2000, 2004).

The Rosa de Maio, Bandeirantes, and Maués are magmatic-hydrothermal Au deposits with associated placer deposits, also known as *garimpos* (*i.e.*, artisanal mining camps), in the northwestern portion of the TMP, northern Brazil (Fig. 5.1). The associated magmatic rocks are part of the post-collisional high-K calc-alkaline to shoshonitic magmatism of the Parauari Suite (PAR, 1.89-1.87 Ga; Santos et al., 2000, 2004), which took place after a period of subduction-controlled arc magmatism in the late stages of the tectonic evolution of the TMP (Cassini et al., 2020). Other Au-only and Au(-Cu) deposits hosted by granitic rocks of the PAR include the Batalha (1883 ± 4 Ma; Juliani et al., 2002), Palito (1883 ± 11 Ma; Echeverri Misas, 2015), and younger São Jorge (1891 ± 3 Ma; Lamarão et al., 2002; Borges et al., 2009).

The Rosa de Maio Granite (RMG, 1879 Ma; Santos et al., 2000, 2004), the type-area of the PAR, hosts the homonymous gold deposit. It is mostly composed of undeformed biotite monzogranite that intruded the tonalitic to granodioritic rocks of the Cuiú-Cuiú Complex (2.04-1.99 Ga, Santos et al., 2000, 2004). The Bandeirantes and Maués intrusions also consist of granitic rocks, with the latter intruding the low-grade metavolcanic and metasedimentary rocks of the Jacareacanga Group (2.2-2.0 Ga, Santos et al., 2000, 2004). Previous exploration surveys identified gold mineralization in the RMG as being associated with disseminated sulfides (pyrite ± chalcopyrite ± galena) or quartz-pyrite veins, typically linked to sericitic alteration and quartz stockwork zones, forming a low Cu/Au ratio ore system. Similar characteristics were identified in the Au-only and Au(-Cu) deposits hosted by 1.88 Ga granitic rocks of the PAR mentioned above (Juliani et al., 2002; Borges et al., 2009; Echeverri Misas, 2015; Juliani et al., 2021; Cassini et al., 2022).

The discovery of gold placer deposits along the Tropas River (a tributary of the Tapajós River) by the end of the 1950s initiated the development of small-scale artisanal mining (garimpos) northward during the 1960s and 1970s (Santos et al., 2001; Costa and Rios, 2022). In the 1980s, these garimpos extended even further to the north, reaching tributaries of the Parauari River such as the Anta and Cedro Grande, where the Rosa de Maio and Bandeirantes gold placer deposits are located, respectively (Costa and Rios, 2022). Despite a lack of officially reported production, the annual gold production from 1975 to 1990 was between 60 and 80 tonnes, making the TMP the main gold producer in Brazil during the 1970s (Santos et al., 2001). Most of the garimpo activity declined from the 1990s onwards, and several mining companies explored the region since 1995 (Costa and Rios, 2022; Santos et al., 2001). A drill hole program was conducted in the RMG by the early 2010s, with little further exploration progress. One of the limitations was the challenging accessibility of this area. Up to the present, the Rosa de Maio, Bandeirantes, and Maués are more easily accessible by small aircraft amidst the Amazon rainforest. No formal resource or reserve estimates are currently available for the Rosa de Maio deposit.

Although the Rosa de Maio deposit has been known for decades and its magmatic evolution has been recently investigated (Alves et al., 2025), its hydrothermal evolution and gold mineralization remain poorly understood. In this contribution, we present the first detailed description of the Rosa de Maio hydrothermal system by integrating detailed petrography, whole-rock geochemistry of least-altered to altered host rocks, mineral chemistry, Ar-Ar geochronology of hydrothermal muscovite, and sulfur isotope analyses. These data allow us to propose a paragenetic sequence of hydrothermal alteration, constrain the timing and sources of the mineralizing fluids, and provide insights into the mechanisms of gold precipitation.

5.2 Geological framework

The Tapajós Mineral Province (TMP), also known as the Tapajós Gold Province, is a metallogenic province in the southern Amazonian Craton (northern Brazil) composed predominantly of Au(-Cu) deposits (Fig. 5.1). These deposits are regarded as porphyry-like and epithermal systems (Juliani et al., 2005;

Echeverri Misas, 2015; Cassini, 2016; Borgo et al., 2017; Lopes and Moura, 2019; Juliani et al., 2021; Cassini et al., 2022), intrusion-related gold systems (IRGS, Santos et al., 2001; Villas et al., 2013), and hybrid systems that display both IRGS and Au-rich porphyry features (Juliani et al., 2002; Borges et al., 2009; Biondi et al., 2018). These deposits are hosted in Orosirian (*ca.* 2.0-1.88 Ga) volcanic and plutonic rocks of the Central Amazonian and Ventuari-Tapajós geochronological provinces, as defined by Tassinari and Macambira (1999), or the Central Amazon and Tapajós-Parima provinces, as proposed by Santos et al. (2000).

According to Santos et al. (2000, 2004), the Tapajós-Parima Province (2.04-1.87 Ga) represents a collisional orogen formed by the amalgamation of multiple magmatic arcs with an older Archean-Paleoproterozoic crust, resulting in a crustal segment extending over 2000 km along a NW-SE strike (Fig. 5.1). These authors proposed that island arc magmatism evolved into mature continental arc and post-orogenic magmatism during the Mundurucus and Tropas orogenies, from 2.04 to 1.87 Ga. Carneiro et al. (2018) revised this tectonic evolution, recognizing deep E-W trending structures beneath the TMP (at *ca.* 15 km) using magnetic data, which they interpreted as evidence of the westward continuity of the Carajás Province at depth. In their interpretation, the NNW-SSE structures observed at the surface reflect shallower tectonic processes. Under this new tectonic model, the TMP is considered more of a continental accretionary orogen, similar to the Andean Cordillera, that developed over an Archean basement rather than a collage of multiple arcs.

Most Au-(base metal) deposits in the TMP are hosted in rocks grouped into the older magmatic sequence (OMS, 2.0-1.95 Ga) and the younger magmatic sequence (YMS, 1.90-1.86 Ga), which are separated by a *ca.* 50 Myr gap characterized by an absence of volcanism and plutonism in the geological record (Table 5.1; Cassini et al., 2020, 2022; Santos et al., 2004). In the tectonic model proposed by Santos et al. (2004), the OMS and YMS are equivalent to the Mundurucus and Tropas orogenies, respectively. The OMS comprises the Jacareacanga Group (2.2-2.0 Ga, low-grade metavolcanic and metasedimentary rocks), the Cuiú-Cuiú Complex (2.04-1.99 Ga, tonalite and granodiorite), the Vila Riozinho Formation (2.0 Ga, basaltic andesite, trachyte, and rhyolite), the

Jamanxim Suite (2.0-1.98 Ga, monzogranite), and the Creporizão Suite (1.99-1.95 Ga, high-K calc-alkaline granitic rocks). This sequence essentially represents the evolution from island arc magmatism to Andean-type continental arc magmatism (Table 5.1; Santos et al., 2000, 2001, 2004; Lamarão et al., 2002; Cassini et al., 2020). Examples of Au deposits hosted in the OMS include the porphyry-like Tocantinzinho (Borgo et al., 2017; Biondi et al., 2018; Lopes and Moura, 2019) and Patrocínio (Cassini, 2016) deposits, the structurally-controlled granite-hosted Moreira Gomes (Assunção and Klein, 2014), and the epithermal Coringa (Guimarães and Klein, 2020; Guimarães et al., 2021) deposits (see Juliani et al., 2021).

The YMS includes the Tropas Suite (1.90-1.88 Ga, tonalite and granodiorite), the Parauari Suite (1.89-1.87 Ga, tonalite, granodiorite, monzo- and syenogranite), and the Iriri Group (1.89-1.87 Ga, high-K to shoshonite series intermediate to acidic volcanic rocks). This group encompasses the Bom Jardim (1.89-1.88 Ga, basaltic andesite, andesite, trachyte, and ignimbrites), Salustiano (1.88-1.87 Ga, dacite, rhyodacite, and rhyolite), Aruri (1.88-1.87 Ga, acidic tuffs, volcanic breccias, and dacitic ignimbrites), and Moraes Almeida (1.89-1.87 Ga, rhyolite, trachyte, and ignimbrites) formations (Table 5.1). This sequence represents a further evolution of the continental arc after a *ca.* 50 million-year hiatus, involving the progressive metasomatism of the mantle wedge and the generation of mature arc magmatism and volcanism in a late- to post-orogenic tectonic setting (Dall'Agnol et al., 1999; Santos et al., 2000, 2001, 2004; Lamarão et al., 2002; Juliani et al., 2005; Cassini et al., 2020, 2022). The last stage of granitic magmatism in the YMS is represented by the Maloquinha Suite (1.87-1.86 Ga, high-K to shoshonite series syeno- and alkali feldspar granite), which occurred following flat-subduction and slab break-off, in a post-orogenic to early-anorogenic setting (Santos et al., 2000, 2001, 2004; Lamarão et al., 2002; Cassini et al., 2020, 2022). A summary of the main rock types, corresponding geotectonic settings, and associated mineral deposits for these lithostratigraphic units is presented in Table 5.1.

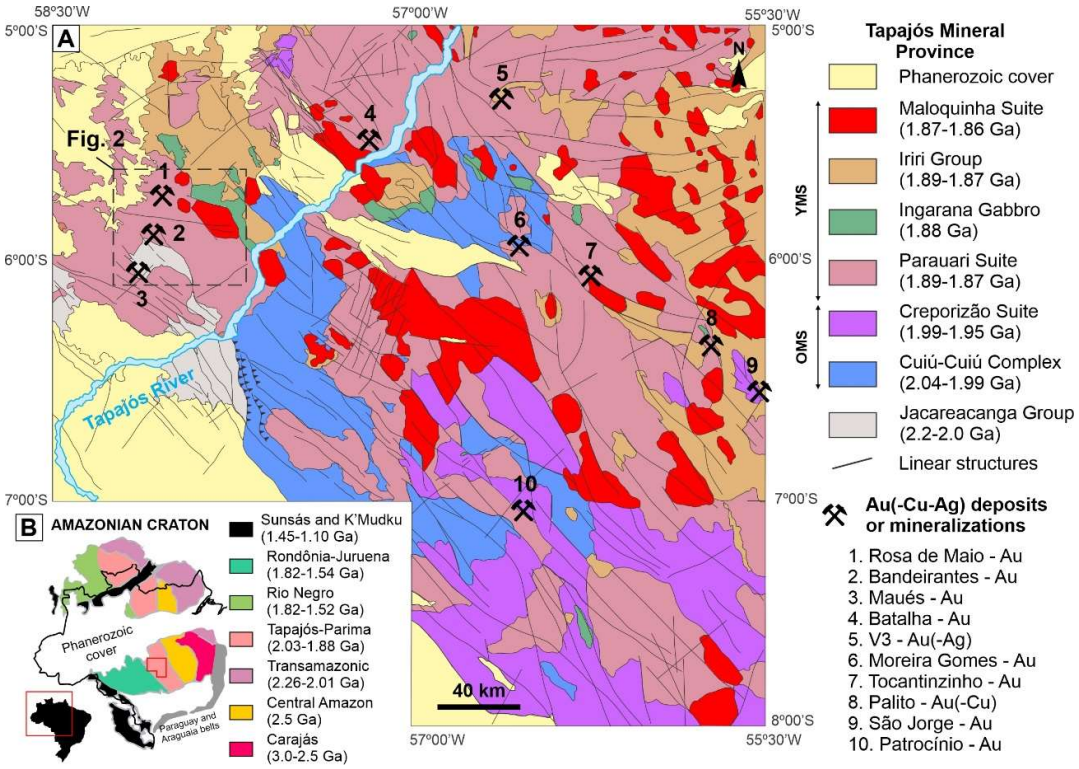

Figure 5.1 – A) Simplified geological map of the Tapajós Mineral Province (TMP) showing some of the main Au(-Cu-Ag) deposits. B) Location of the TMP within the Amazonian Craton. Tectonic subdivision of the craton after Santos et al. (2000, 2006). From Alves et al. (2025), modified after Klein et al. (2001). OMS = Older magmatic sequence; YMS = Younger magmatic sequence.

The Parauari Suite (PAR, 1.89-1.87 Ga) represents a widespread evolved arc magmatism troughout the TMP (Fig. 5.1) that intruded the Cuiú-Cuiú Complex and the Creporizão Suite. This suite consists of high-K calc-alkaline to shoshonitic, metaluminous to weakly peraluminous porphyritic granitic rocks, ranging from biotite and/or hornblende tonalite to syenogranite, with monzonite as the dominant rock type (Santos et al., 2000, 2004; Cassini et al., 2020). The Ingarana Gabbro (1881 ± 3; Santos et al., 2004) comprises calc-alkaline augite gabbros, which were included in the magmatic evolution of the PAR by Santos et al. (2004). Its mafic composition and coeval emplacement with the PAR led these authors to interpret the suite as bimodal. In the tectonic model proposed by Santos et al. (2004), the PAR is interpreted as a third continental arc that developed following the initial island arc phase associated with the Tropas Suite during the Tropas Orogeny (1.90-1.88 Ga). This magmatism took place after the 50 Myr quiescent period that separates the Mundurucus Orogeny (2.04-1.95 Ga, closely correlated with the OMS) from the Tropas Orogeny (which closely correlates with the YMS). According to Cassini et al. (2020), the PAR marks the

onset of the YMS. As subduction continued and the slab flattened, a mature continental arc magmatism was generated by partial melting of a progressively metasomatized mantle wedge above a long-lived subduction zone in a late- to post-orogenic tectonic setting.

Table 5.1 – Summary of the main lithostratigraphic units of the TMP. Modified from Alves et al. (2025) and Cassini et al. (2020, 2022).

	Tectonic subdivision	Lithostratigraphic unit		Description	Geotectonic context	Deposit/Mineral occurrence
Tapajós Mineral Province - TMP (closely correlates with the Tapajós-Parima Orogen[3])	Younger magmatic sequence (YMS)[6] or Tropas Orogeny[3]	Maloquinha Suite (1.87-1.86 Ga)[2, 3, 4]		Shoshonitic syeno- to alkali feldspar granite	Post-orogenic[1, 2, 3], Post-orogenic to early-anorogenic[6]	
		Iriri Group (1.89-1.87 Ga)[2, 3, 5]	Moraes Almeida Aruri Salustiano Bom Jardim	High-K calc-alkaline to shoshonitic intermediate to acidic volcanic rocks	Multiple interpretations including magmatic arc and post-orogenic to early-anorogenic[1, 2, 3, 4, 5, 6]	V3 (Au)[13]
		Parauari Suite (1.89-1.87 Ga)[2, 3, 6]		High-K calc-alkaline to shoshonitic tonalitic to syenogranitic rocks	Magmatic arc[2, 3], Late- to post-orogenic[6]	Rosa de Maio (Au), Bandeirantes (Au), Batalha (Au)[12], Palito (Au-Cu)[13], São Jorge (Au)[4, 14]
		Tropas Suite (1.90-1.88 Ga)[2, 3]		Tonalite and granodiorite	Island arc[2, 3]	
	Older magmatic sequence (OMS)[6] or Mundurucus Orogeny[3]	Creporizão Suite (1.99-1.95 Ga)[2, 3, 6]		High-K calc-alkaline to shoshonitic tonalitic to syenogranitic rocks	Magmatic arc[2, 3, 6]	Tocantinzinho (Au)[7, 8, 9], Patrocínio (Au)[10], Moreira Gomes (Au)[11]
		Jamanxim Suite (2.0-1.98 Ga)[3]		Monzogranite		
		Vila Riozinho Formation (2.0 Ga)[4]		Calc-alkaline to shoshonitic intermediate to acidic volcanic rocks	Magmatic arc[4]	Coringa (Au-Ag)[15]
		Cuiú-Cuiú Complex (2.04-1.99 Ga)[1, 2, 3]		Calc-alkaline tonalite, diorite, granodiorite	Island arc[1, 2, 3], Magmatic arc[6]	
		Jacareacanga Group (2.2-2.0 Ga)[1, 2, 3]		Metavolcanic and metasedimentary rocks	Back-arc and trench sedimentation[1, 2, 3]	

References: 1 - Santos et al. (2000), 2 - Santos et al. (2001), 3 - Santos et al. (2004), 4 - Lamarão et al. (2002), 5 - Juliani et al. (2005), 6 - Cassini et al. (2020), 7 – Borgo et al. (2017), 8 – Biondi et al. (2018), 9 – Lopes and Moura (2019), 10 – Cassini (2016), 11 - Assunção and Klein (2014), 12 - Juliani et al. (2002), 13 - Echeverri Misas (2015), 14 – Borges et al. (2009), and 15 – Guimarães et al. (2021).

Cassini et al. (2020, 2022) considered the PAR magmatism potentially fertile for the formation of Au-rich magmatic-hydrothermal deposits. These authors proposed that the generation of this mature arc magmatism, driven by partial melting of a metasomatized subcontinental lithospheric mantle, may have

destabilized pre-formed Au-rich residual sulfides in the mantle. Additionally, they suggested that the PAR magmatism could have remobilized earlier Au mineralization associated with the OMS. Alves et al. (2025) studied the granitic rocks genetically linked to the Rosa de Maio Au deposit (1.89 Ga), the type locality for the PAR magmatism (Santos et al., 2004), and highlighted their similarities to magmatic host rocks genetically associated with Au-rich porphyry-style systems. These similarities include low Cu/Au ratios, a high-K calc-alkaline signature, low Sr/Y values, and emplacement in a late- to post-orogenic tectonic setting. Good examples of Au-rich magmatic-hydrothermal deposits associated with granitic magmatism coeval to the PAR are the Batalha (Juliani et al., 2002), Palito (Echeverri Misas, 2010, 2015), and São Jorge (Lamarão et al., 2002) deposits (see also Juliani et al., 2021; Cassini et al., 2022).

The Batalha Au deposit (Fig. 5.1; Juliani et al., 2002) is hosted by the eponymous granite intrusion (1883 ± 4 Ma, Juliani et al., 2002), which consists of metaluminous to peraluminous, high-K calc-alkaline, hornblende and/or biotite syeno- to monzogranites with a late- to post-orogenic affinity. During the hydrothermal stage (500-290 °C and 2.6-1.2 kbar), these rocks underwent pervasive and fissural Na metasomatism, as well as potassic, propylitic, and sericitic alteration. Gold mineralization is mostly associated with sericitic alteration and occurs with quartz, sericite, pyrite, chalcopyrite, and galena assemblages, both within stockworks and disseminated around hydrothermal veins (Juliani et al., 2002, 2021). Juliani et al. (2002) recognized characteristics of both porphyry-like deposits and intrusion-related gold systems (IRGS) in the Batalha deposit, while Juliani et al. (2021) interpreted it as a deep-emplaced granite-hosted Au-(Cu) deposit.

The Palito Au(-Cu) deposit (Fig. 5.1; Echeverri-Misas, 2010, 2015) is hosted by the Palito Granite (1883 ± 11 Ma, Aquino, 2013), which is composed of metaluminous to peraluminous and high-K alkali-calcic biotite monzogranite to alkali feldspar granite. This intrusion, included in the PAR, was also emplaced in a late- to post-orogenic setting (Cassini et al., 2020, 2022). The deposit has proven and probable reserves estimated at 717,000 t @ 11.74 g/t Au (Juliani et al., 2021 and references therein). These granitic rocks were affected by potassic, propylitic, sericitic, and argillic/advanced argillic alteration. The Au(-Cu)

mineralization occurs in sulfide-quartz and semi-massive sulfide veins, stockworks, hydrothermal breccias, and finely disseminated sulfides (Echeverri-Misas, 2010; Juliani et al., 2021). Based on $\delta^{34}S$ values between +1.2 and +3.6‰ for pyrite and chalcopyrite, Echeverri-Misas (2010) proposed a magmatic sulfur source for the sulfides precipitated in the hydrothermal stage. These magmatic and hydrothermal features are consistent with Au(-Cu) porphyry-type deposits (Echeverri-Misas, 2010, 2015; Juliani et al., 2021; Cassini et al., 2020, 2022).

The São Jorge Au deposit (Fig. 5.1; Lamarão et al., 2002; Borges et al., 2009) is hosted by two distinct intrusions: the older (1.98 Ga) and younger (1.89 Ga) São Jorge granites (Lamarão et al., 2002). The younger São Jorge Granite (1891 ± 3 Ma, Lamarão et al., 2002), more closely associated with Au mineralization, comprises metaluminous to peraluminous , high-K alkali-calcic hornblende-biotite monzogranites (Cassini et al., 2022; Borges et al., 2009). These rocks underwent potassic, propylitic, and sericitic alteration, with gold mineralization predominantly associated with sericitic alteration and occurring in stockworks, sheeted quartz-sulfide veins, and disseminated ore. The sericitic assemblage includes sericite, pyrite, carbonates, chalcopyrite, sphalerite, and galena (Borges et al., 2009; Juliani et al., 2021). Borges et al. (2009) recognized the São Jorge deposit as either a porphyry-like or IRGS, while Juliani et al. (2021) interpreted it as a structurally-controlled granite-hosted Au deposit.

5.3 Analytical methods and procedures

5.3.1 Lithogeochemistry

Sample preparation was carried out in the Laboratório de Preparação de Amostras of the Instituto de Geociências of the University of Brasília (Brazil) and involved hand sample disaggregation, crushing, pulverization with a swing mill, and quartering. Major, minor, and trace element bulk rock analyses of 23 samples were conducted at ACME Analytical Laboratories Ltd. (Vancouver, Canada). The standard analytical procedure involves blending rock pulps with lithium tetraborate and then melting the mixture to produce fused glass beads. The fused beads undergo X-ray fluorescence spectroscopy (XRF) analysis for major elements and inductively coupled plasma mass spectrometry (ICP-MS) for minor

and trace elements. Further information on analytical procedures is available at acmelab.com.

5.3.2 Mineral chemistry

Chemical compositions of biotite, epidote, chlorite, and muscovite were obtained using a JEOL JXA-8230 electron microprobe at the Instituto de Geociências of the University of Brasília (Brazil). Analyses of Si, Ti, Al, Fe, Mn, Mg, Ca, Ba, Na, K, F, and Cl were performed on polished thin sections (30 μm thick) at an accelerating voltage of 15 kV and a beam current of 10 nA with 1 μm spot diameter. Dwell times in all elements were 10 s at peak and 5 s in the background. The Kα X-ray line was used for all elements. Standards were the following reference materials: microcline (Si, Al, and K), andradite (Fe and Ca), barite (Ba), albite (Na), forsterite (Mg), topaz (F), vanadinite (Cl), and pyrophanite (Ti and Mn). Data reduction was carried out using the microprobe software package.

5.3.3 Ar-Ar isotope systematics

The $^{40}Ar/^{39}Ar$ geochronological analyses of muscovite were conducted at the Queen's Facility for Isotope Research (QFIR), Department of Geological Sciences and Geological Engineering, Queen's University, Canada. High-purity unaltered mineral separates were obtained by crushing, sieving, and handpicking under a binocular microscope. The selected grains were further purified by ultrasonic cleaning in ethanol for 20 minutes, followed by washing with deionized water. For irradiation, 10 mg of muscovite separate were wrapped in aluminum foil and stacked vertically in an aluminum canister with the irradiation standard Hb3gr hornblende (K-Ar age = 1072 ± 11, 1σ; Roddick, 1983; Turner et al., 1971). The samples underwent neutron irradiation for 40 hours at the McMaster Nuclear Reactor in Hamilton, Ontario, Canada. Following irradiation, the $^{40}Ar/^{39}Ar$ step-heating analyses were performed using a MAP 216 noble gas mass spectrometer with a Baur-Signer ion source and an electron multiplier. Samples and standards were loaded into small pits (2mm diameter, 1.5 mm depth) drilled into a Cu sample holder, positioned beneath a sapphire viewpoint in a bakeable stainless-steel chamber. The irradiation parameter (J value) was determined through second-order polynomial interpolation. Step-heating was conducted using a

defocused 8W Lexel 3500 Ar-ion laser. Each heating step lasted approximately three minutes, with final steps involving full fusion of the sample. Released gases were purified using a Ti sponge and Zr-Al getters before analysis. Argon isotope ratios were normalized to an atmospheric $^{40}Ar/^{36}Ar$ ratio, and dates were calculated using conventional ^{40}K decay constants (Renne et al., 2011). Isotope analyses were corrected for system blanks, atmospheric contamination, and neutron-induced interference (*e.g.*, radioactive decay of ^{37}Ar and ^{39}Ar, and minor reactions from Ca, Cl, and K). To assess potential excess argon from alteration or mineral inclusions, Ca/K and Cl/K ratios were determined from $^{37}Ar/^{39}Ar$ and $^{38}Ar/^{39}Ar$ ratios using values derived from the flux monitor Hb3gr. The analytical precision for individual steps used in plateau age calculations was 0.5% at the 2σ confidence level. Dates were calculated using the online version of IsoplotR (Vermeesch, 2018).

5.3.4 Sulfur isotope systematics

Sulfur isotope compositions ($^{34}S/^{32}S$ ratios) of pyrite were determined at the Laboratório de Estudos Geodinâmicos, Geocronológicos e Ambientais of the University of Brasília, Brazil, following the procedures described by Bender et al. (2008). Pyrite grains were handpicked, mounted in epoxy, and polished for vaporization in a laser ablation system using a 65 μm spot size. The ablated material was conveyed into a Thermo Finnigan Neptune multicollector ICP-MS. The laser frequency was 10 Hz with 60% energy. Py-BSB was used as the internal standard. Isotope ratios ($^{34}S/^{32}S$) are expressed in δ notation (‰) relative to the Vienna-Canyon Diablo Troilite (V-CDT). Internal analytical precision is between ±0.1-0.2 ‰ (2σ).

5.4 Results

5.4.1 Local geology and the RMG intrusion

The Rosa de Maio, Bandeirantes, and Maués are Au-mineralized magmatic-hydrothermal deposits in the northwestern TMP with associated high-grade, low tonnage placer deposits (Fig. 5.2; Alves et al., 2025). These deposits have been mined by *garimpos* (small-scale artisanal mining) since the 1980s (Costa and Rios, 2022), following the northward expansion of this activity initiated in 1958 along the Tropas River, a tributary of the Tapajós River (Fig. 5.2),

southeast of this region (Santos et al., 2001). After the 1990s, *garimpo* activity declined, and multiple mining companies have explored this area since 1995 (Santos et al., 2001; Costa and Rios, 2022). Between 2005 and 2006, gold soil geochemical sampling and an airborne geophysical survey were conducted in the Rosa de Maio prospect, followed by core drilling in the early 2010s, with little further exploration progress since then.

The magmatic rocks associated with the Rosa de Maio, Bandeirantes, and Maués magmatic-hydrothermal deposits are part of the PAR magmatism (1.89-1.87 Ga; Santos et al., 2000, 2004), which is widespread in this region and comprises mostly biotite monzo- to syenogranites. This high-K calc-alkaline to shoshonitic magmatism persisted for at least 10 Myr in this area (*ca.* 1907-1890 Ma; Alves et al., 2025) and took place in a late- to post-orogenic setting during the late stages of the TMP tectonic evolution, following a period of subduction-controlled arc magmatism (Cassini et al., 2020). In this area, the PAR magmatism intruded low-grade metavolcanic and metasedimentary rocks of the Jacareacanga Group (2.2-2.0 Ga, Santos et al., 2000, 2004), which is represented by a roof pendant enclosed by PAR granites between the Bandeirantes and Maués deposits (Fig. 5.2). The PAR magmatism is also coeval with the felsic volcanism of the Iriri Group (1.89-1.87 Ga, Santos et al., 2001, 2004; Juliani et al., 2005). These volcanic rocks also host gold mineralization at the Doze de Outubro prospect, located ~50 km northeast of the RMG, and it has been recognized either as an epizonal intrusion-related system (Santos et al., 2001) or as an epithermal deposit (Juliani et al., 2021).

The Rosa de Maio Granite (RMG, 1890 Ma) outcrops over an area of at least 5 km² as porphyry stocks that intruded an older PAR granite emplaced prior to 1890 Ma (Figs. 5.3 and 5.4). It comprises high-silica, peraluminous to strongly peraluminous, high-K calc-alkaline, ferroan, and relatively oxidized granites (Alves et al., 2025). Unaltered rock types in the RMG are undeformed and include the biotite monzo- to syenogranite, the muscovite-rich aplite, and biotite-rich microgranitoid enclaves (Alves et al., 2025). The medium- to coarse-grained porphyritic biotite granite is the most abundant and voluminous rock type, composed of quartz, plagioclase, microcline, biotite, and muscovite. Fluorapatite, zircon, monazite, xenotime, magnetite, ilmenite, and pyrite are accessory phases

(Alves et al., 2025). The biotite granite is crosscut by aplitic dykes, which is composed of quartz, microcline, plagioclase, and muscovite (Alves et al., 2025). Plutons of the Maloquinha Suite (1.87-1.86 Ga, Santos et al., 2000, 2001, 2004) intruded the older PAR granite (pre-1890 Ma) ~5 km east of the RMG (Figs. 5.2 and 5.3).

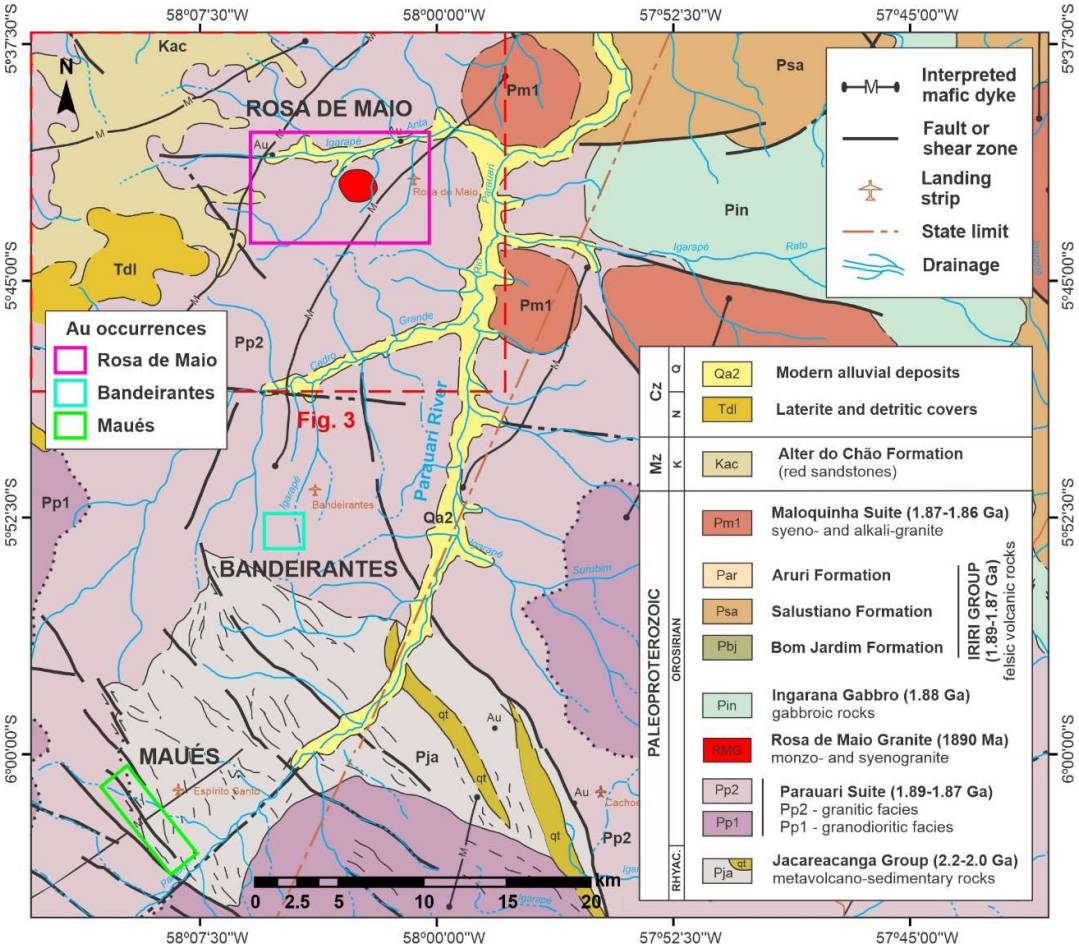

Figure 5.2 – Geological map of the study area showing the approximate extent of gold occurrences associated with the Rosa de Maio, Bandeirantes, and Maués deposits. Modified from Alves et al. (2025) and Klein et al. (2001).

Alves et al. (2025) proposed that the monzo- to syenogranitic magmas represented by the biotite granite evolved from biotite-rich tonalitic to granodioritic parental magmas essentially via fractional crystallization. Continued fractionation would have led to the formation of muscovite-rich syeno- and alkali feldspar granitic aplites during the late stages of the RMG's magmatic evolution. These authors also suggest that magmatic sulfide saturation may have been a first-order

control on the low Cu/Au ratios of this deposit. For further details on the magmatic evolution of the RMG, see Alves et al. (2025).

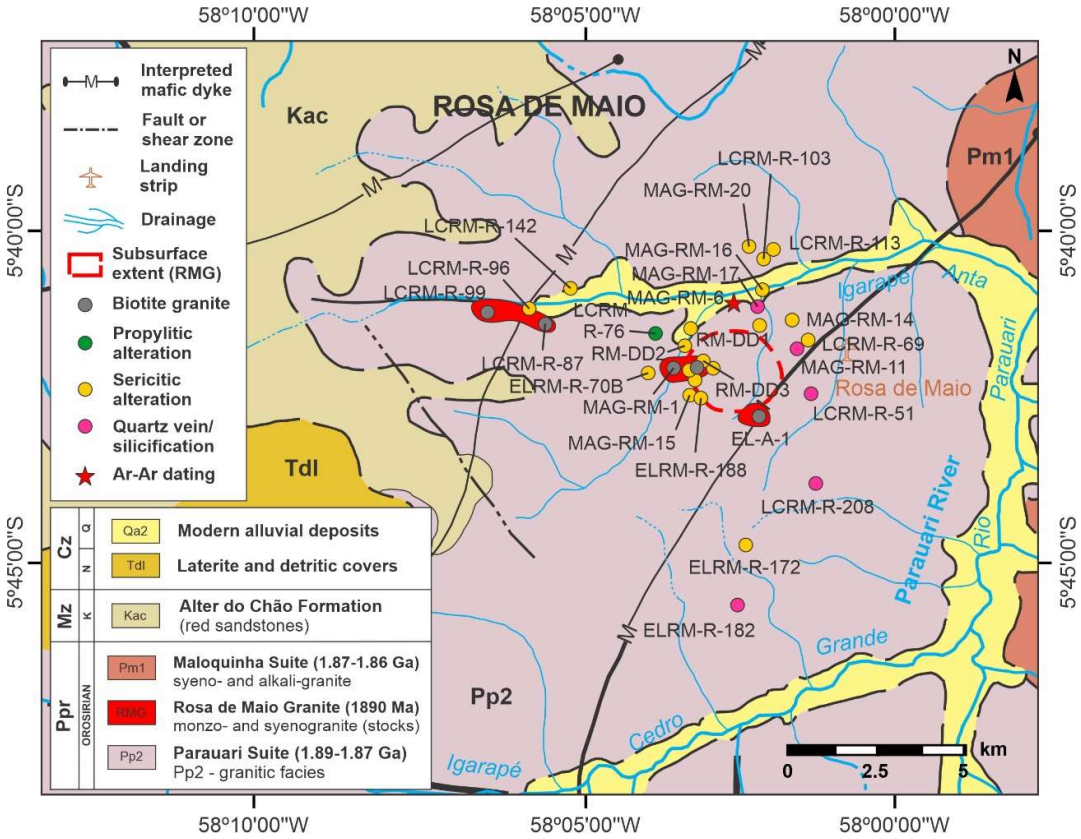

Figure 5.3 – Geological map of the Rosa de Maio deposit showing the locations of samples used for whole-rock geochemical analyses and $^{40}Ar/^{39}Ar$ geochronology. Whole-rock geochemical data are presented in Appendix A, and $^{40}Ar/^{39}Ar$ geochronological data are presented in Appendix C. Modified from Klein et al. (2001).

Based on deposit-scale mapping and petrography of surface and drill core samples (to depths of up to 260 m), two distinct hydrothermal systems are recognized at the Rosa de Maio deposit: (i) a deeper magmatic-hydrothermal system spatially associated with the RMG, characterized by a sequence of sodic, potassic, propylitic, and seritic alterations; and (ii) remnants of a shallower hydrothermal system developed above the RMG at surface and near-surface levels, displaying sericitic alteration zones and silicification associated with quartz veins. Gold mineralization occurs in both systems (Fig. 5.4).

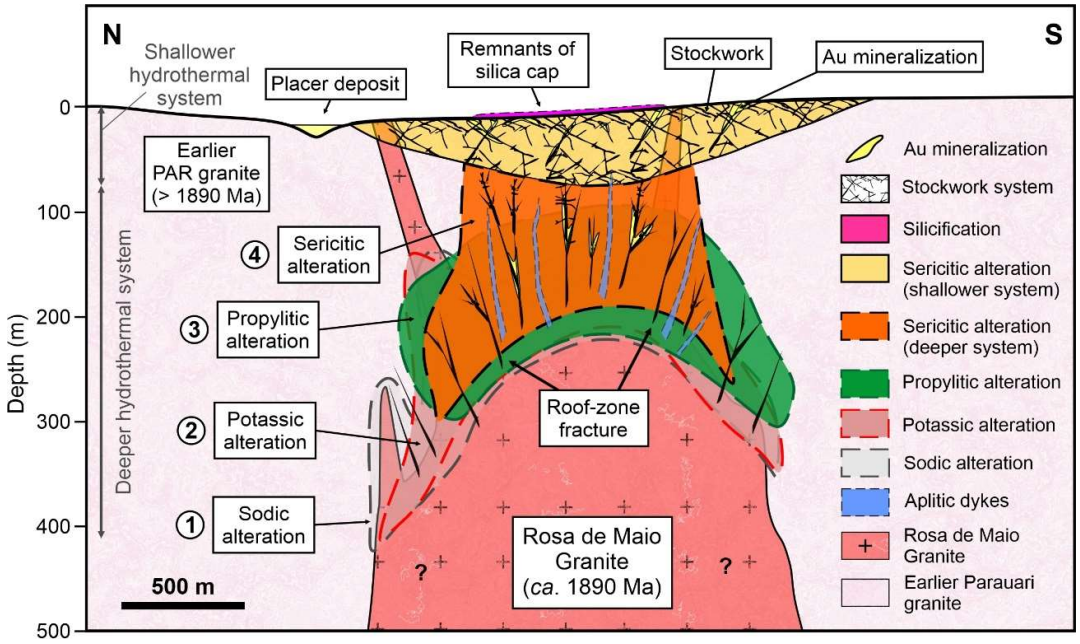

Figure 5.4 – Simplified schematic cross-section of the Rosa de Maio deposit showing the interpreted sequence of hydrothermal alteration and associated gold mineralization. The extent of the alteration zones is exaggerated for clarity, and the scales are approximate.

5.4.2 Hydrothermal assemblages and mineralization in the deeper system

Four alteration types are identified in the deeper Rosa de Maio hydrothermal system: sodic, potassic, propylitic, and sericitic (Fig. 5.4). The sequence of magmatic and early- to late-stage hydrothermal assemblages is presented in Figure 5.5, established from crosscutting relationships and both macroscopic and microscopic petrography (optical and electron microscopy). Pervasive sodic alteration is commonly overprinted by fissural to pervasive potassic, propylitic, and sericitic alterations. Gold mineralization is mostly hosted within the sericitic alteration.

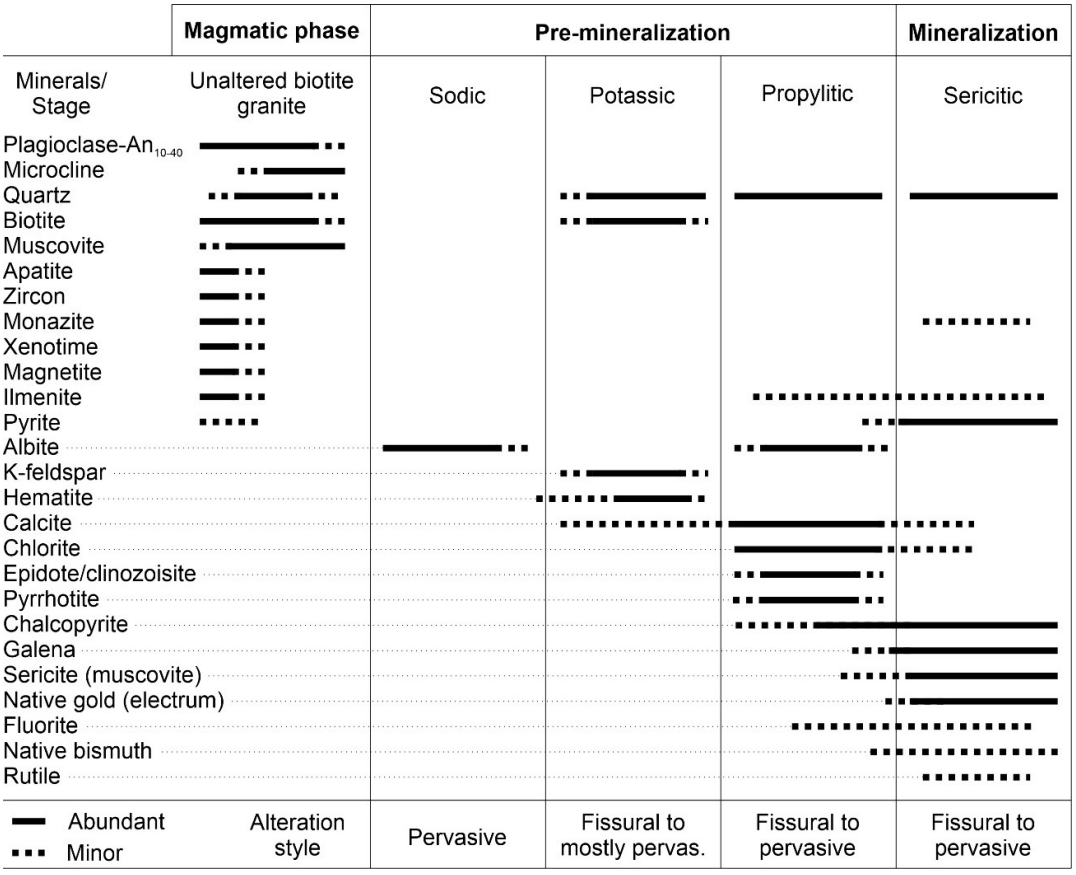

Figure 5.5 – Magmatic assemblage of the biotite granite and paragenetic sequence of hydrothermal alteration assemblages in the deeper Rosa de Maio hydrothermal system. Modified from Alves et al. (2025).

5.4.2.1 Sodic alteration

Sodic alteration represents the earliest stage of the hydrothermal phase in the RMG. It is the most widespread alteration, extending up to several hundred meters, with many of the least-altered granites displaying incipient sodic alteration. Most of the magmatic textures are preserved in moderately sodic-altered granites, which maintain characteristics similar to their unaltered counterparts. In the late sodic alteration transitioning to the potassic alteration, primary feldspars, particularly plagioclase, become more reddish due to the onset of hematite precipitation.

Sodic alteration in the Rosa de Maio deposit is characterized by pervasive and partial replacement of magmatic plagioclase (An_{10-40}) through a dissolution-precipitation process, forming discrete and clear albite rims around magmatic plagioclase cores that were subsequently altered to sericite (Figs. 5.6A to 5.6F).

This alteration is also represented by the precipitation of chessboard albite (Fig. 5.6E). Perthitic microcline (primary) is less affected than plagioclase.

5.4.2.2 Potassic alteration

The potassic alteration is also widespread in the RMG and overprints the sodic alteration. It occurs as veins surrounded by a pervasive alteration front (*i.e.*, fissural to pervasive) that extends up to a few tens of meters. Zones of potassic- and sodic-altered, and unaltered granites alternate along the length of drill cores, which reach depths of 150-260 m. The porphyritic texture can still be recognized (Figs. 5.6G to 5.6I), while the main characteristic of this alteration at the macroscopic scale is the color change from gray in sodic-altered and unaltered granites to deep reddish in advanced potassic-altered granites (Figs. 5.6G to 5.6I). Plagioclase is markedly more affected and becomes deeper red than microcline (Fig. 5.6H). The reddish hues are likely due to the precipitation of disseminated, very fine-grained hematite.

In the Rosa de Maio deposit, potassic alteration is characterized by pervasive replacement of magmatic feldspars by hydrothermal K-feldspar and of magmatic biotite by fine-grained aggregates of hydrothermal biotite, both commonly associated with quartz (Figs. 5.6J to 5.6L). Hydrothermal biotite often forms patches that partially or completely replace coarser-grained magmatic biotite, progressing from rims towards cores (Figs. 5.6J and 5.6K). The potassic alteration assemblage includes K-feldspar + biotite + quartz + hematite ± calcite.

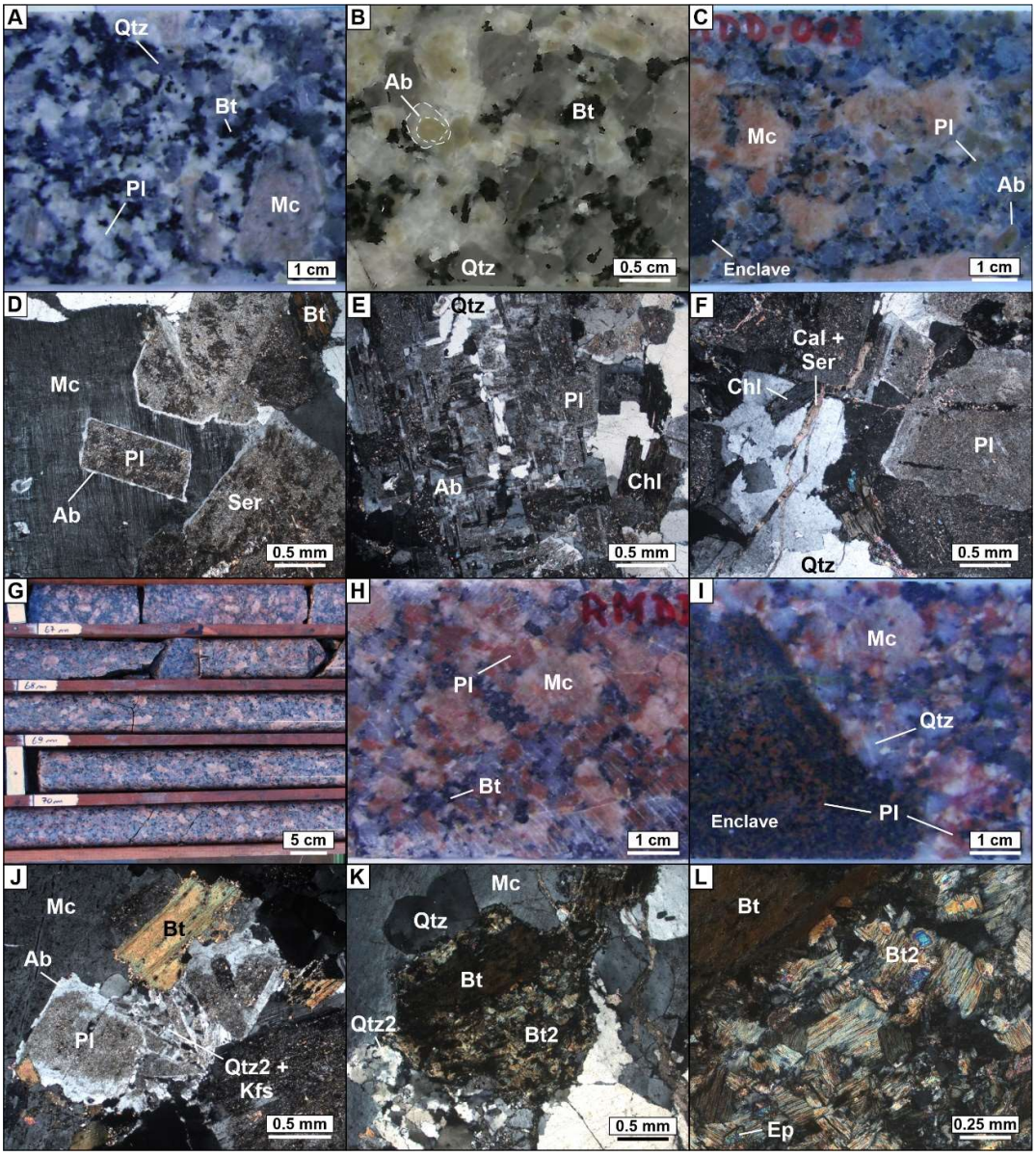

Figure 5.6 – Sodic- and potassic-altered granites from the RMG. A-C) Sodic-altered porphyritic biotite granite. Note albite rims surrounding magmatic plagioclase cores. D-F) Photomicrographs of sodic-altered granite in cross-polarized light (XPL). D) Albite rims around magmatic plagioclase cores, subsequently altered to sericite. E) Chessboard albite formed during sericitic alteration. F) Sodic-altered granite crosscut by late carbonate and sericite veinlets. G-I) Potassic-altered biotite granite characterized by its typical reddish hues, the main macroscopic feature of this alteration. Note that plagioclase displays a deeper red color than microcline. I) Microgranitoid enclave affected by potassic alteration. J-L) Photomicrographs of potassic-altered granite in XPL. J) Interstitial hydrothermal quartz (Qtz2) and K-feldspar (Kfs) formed between magmatic plagioclase previously affected by sodic alteration. K-L) Fine-grained aggregates of hydrothermal biotite (Bt2) replacing magmatic biotite. Qtz = quartz, Pl = plagioclase, Mc = microcline, Bt = biotite, Ab = albite, Ser = sericite, Cal = calcite, Chl = chlorite, Kfs = K-feldspar, Bt2 = hydrothermal biotite, Ep = epidote. Abbreviations after Whitney and Evans (2010).

5.4.2.3 Propylitic alteration

The propylitic alteration is volumetrically less extensive and overprints previous alterations. It occurs proximal to the intrusion center as centimeter-scale veins surrounded by a pervasive alteration front (also fissural to pervasive) that extends up to a few meters. This alteration is highly texture-destructive, partially to completely obliterating the magmatic rock fabric, including the porphyritic texture. At the macroscopic scale, the most prominent characteristic is the color change from the deep reddish hue of potassic-altered granites to the dark gray-greenish hue of propylitic-altered granites (Figs. 5.7A to 5.7C). The magmatic rock-forming assemblage is almost completely destroyed, except for quartz remnants (Fig. 5.7A).

This alteration is characterized by the pervasive replacement of plagioclase, biotite (both magmatic and hydrothermal), and microcline by chlorite, epidote, clinozoisite, calcite (1-3 wt.% MnO, 0.5-1 wt.% FeO), pyrrhotite (0.1-0.2% Pb, ~0.1% Co; Appendix B), quartz, fluorite, and sericite (Figs. 5.7D to 5.7F). Occasionally, the fracture supplying the pervasive alteration is filled by chlorite and calcite. Plagioclase is often replaced by fine-grained chlorite, epidote, sericite, and calcite (Fig. 5.7E). Magmatic biotite is frequently altered to chlorite and epidote/clinozoisite, while acicular ilmenite forms along its cleavage (Fig. 5.7G). In late propylitic alteration, hydraulic brecciation forms millimeter-scale interconnected veinlets composed of chlorite ± carbonate ± sericite and epidote + albite + quartz that crosscut the previously formed propylitic assemblage (Fig. 5.7H). Similar to pyrrhotite in this alteration, chalcopyrite (~0.1% Pb) occurs disseminated and eventually displays a pyrite rim (Fig. 5.7I). The propylitic alteration assemblage comprises chlorite + epidote/clinozoisite + calcite + quartz + pyrrhotite + chalcopyrite + albite ± sericite ± fluorite ± ilmenite.

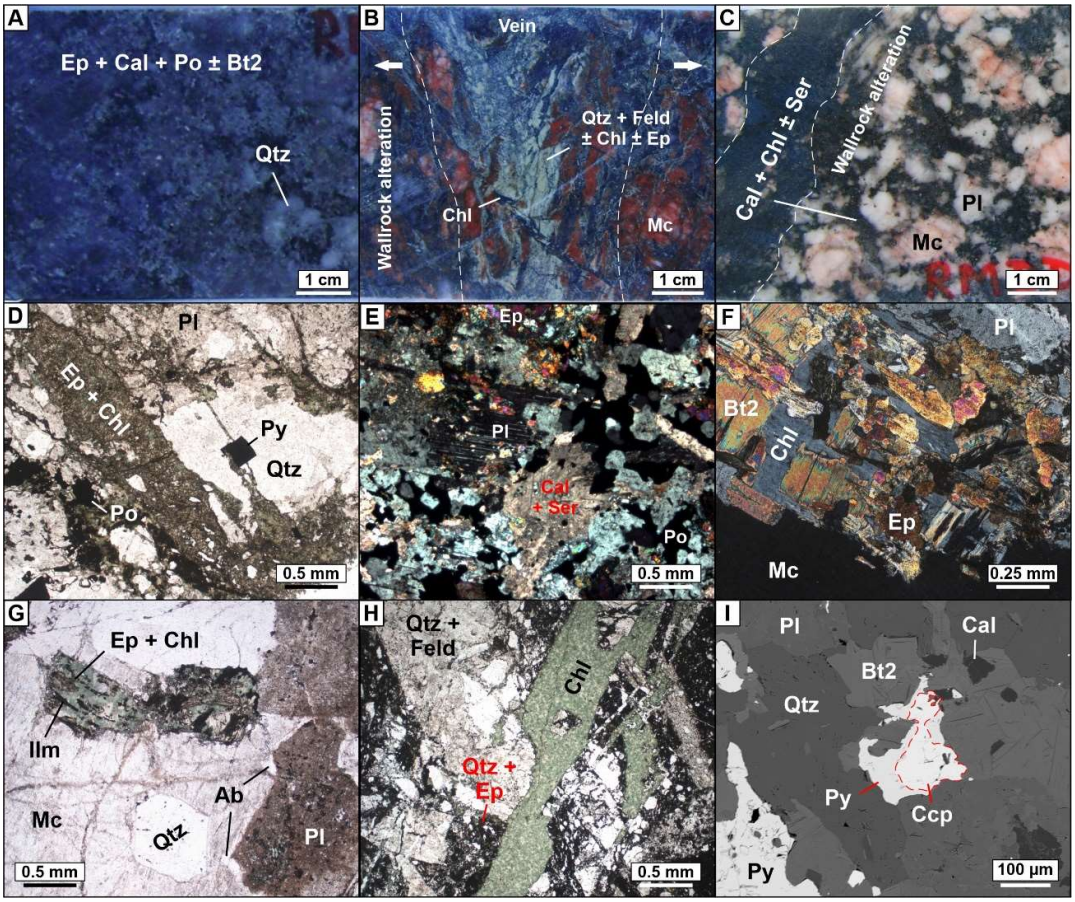

Figure 5.7 – Propylitic alteration zones in the Rosa de Maio deposit. A) Propylitized granite showing characteristic dark greenish hues. B-C) Fractures that channeled fluids driving wallrock alteration, typically infilled with chlorite, epidote, and calcite. D-H) Photomicrographs of propylitic alteration zones in plane-polarized (PPL) and cross-polarized light (XPL). D) Veinlets of epidote and chlorite, with associated pyrrhotite, replace magmatic plagioclase. Pyrite, interpreted as part of a sericitic overprint, is not crosscut by the epidote-chlorite veinlets. E) Epidote, carbonate, pyrrhotite, and sericite replacing magmatic biotite and plagioclase. F) Hydrothermal biotite from the potassic alteration stage being replaced by chlorite and epidote. G) Magmatic biotite replaced by epidote, chlorite, and ilmenite along its cleavage. H) Late chlorite veinlets crosscutting previously formed propylitic assemblage. I) Backscattered electron (BSE) image showing chalcopyrite with a pyrite rim. Ep = epidote, Cal = calcite, Po = pyrrhotite, Bt2 = hydrothermal biotite, Qtz = quartz, Feld = feldspars, Ser = sericite, Mc = microcline, Pl = plagioclase, Py = pyrite, Ilm = ilmenite, Ab = albite, Ccp = chalcopyrite. Abbreviations after Whitney and Evans (2010).

5.4.2.4 Sericitic alteration

The sericitic alteration is also fissural to pervasive, less voluminous compared to the sodic and potassic alterations, and it overprints earlier alterations. It occurs from proximal to distal zones of the intrusion center as millimeter to centimeter-scale veins surrounded by a pervasive alteration front. These veins are often sulfide-rich (Figs. 5.8A to 5.8C). The pervasive alteration front extends from a few centimeters up to one meter. This alteration also

obliterates the magmatic rock fabric, with macroscopic samples displaying dark gray to black hues (Figs. 5.8B and 5.8C). Primary quartz is frequently the only remaining mineral from the magmatic rock-forming assemblage.

Sericitic alteration in the deeper hydrothermal system of the Rosa de Maio deposit is characterized by the pervasive replacement of previous alteration assemblages by sericite, pyrite (0.1-1.2% Co, 0.1-0.2% Pb; Appendix B), and quartz, with minor chlorite, calcite, and fluorite (Figs. 5.8D to 5.8G). Fractures fluid-supplying this pervasive alteration are commonly filled with massive sulfides (mostly pyrite) and fine-grained sericite and quartz (Figs. 5.8D and 5.8E). Fine-grained sericite, quartz, chlorite, and hydrothermal biotite frequently occur as inclusions within these sulfides (Fig. 5.8E). Magmatic biotite is locally completely altered to muscovite, accompanied by acicular ilmenite and rutile precipitating along its cleavage (Fig. 8F). Fluorite commonly occurs with pyrite aggregates (Fig. 5.8G). Hydrothermal monazite may also occur as fine-grained inclusions within pyrite (Fig. 5.8K).

This alteration is marked by the precipitation of sulfides, predominantly pyrite, which occur both filling fractures as small veins and disseminated throughout the pervasive alteration. Galena and chalcopyrite commonly occur as very fine-grained rounded inclusions within pyrite (Fig. 5.8I and 5.8L). In the sericitic alteration, gold (electrum, ~10% Ag) mineralization is intimately associated with sulfides, particularly pyrite, occurring as fine-grained inclusions or closely associated with them (Fig. 5.8H). Native bismuth is also linked to massive precipitation of pyrite (Fig. 5.8J). In samples affected by late sericitic alteration, a second generation of pyrrhotite may occur at pyrite rims and/or filling pyrite fractures (Fig. 5.8L).

The sericitic alteration assemblage comprises sericite + pyrite + quartz + chalcopyrite + galena + gold (electrum) ± fluorite ± native bismuth ± chlorite ± calcite ± ilmenite ± rutile ± monazite.

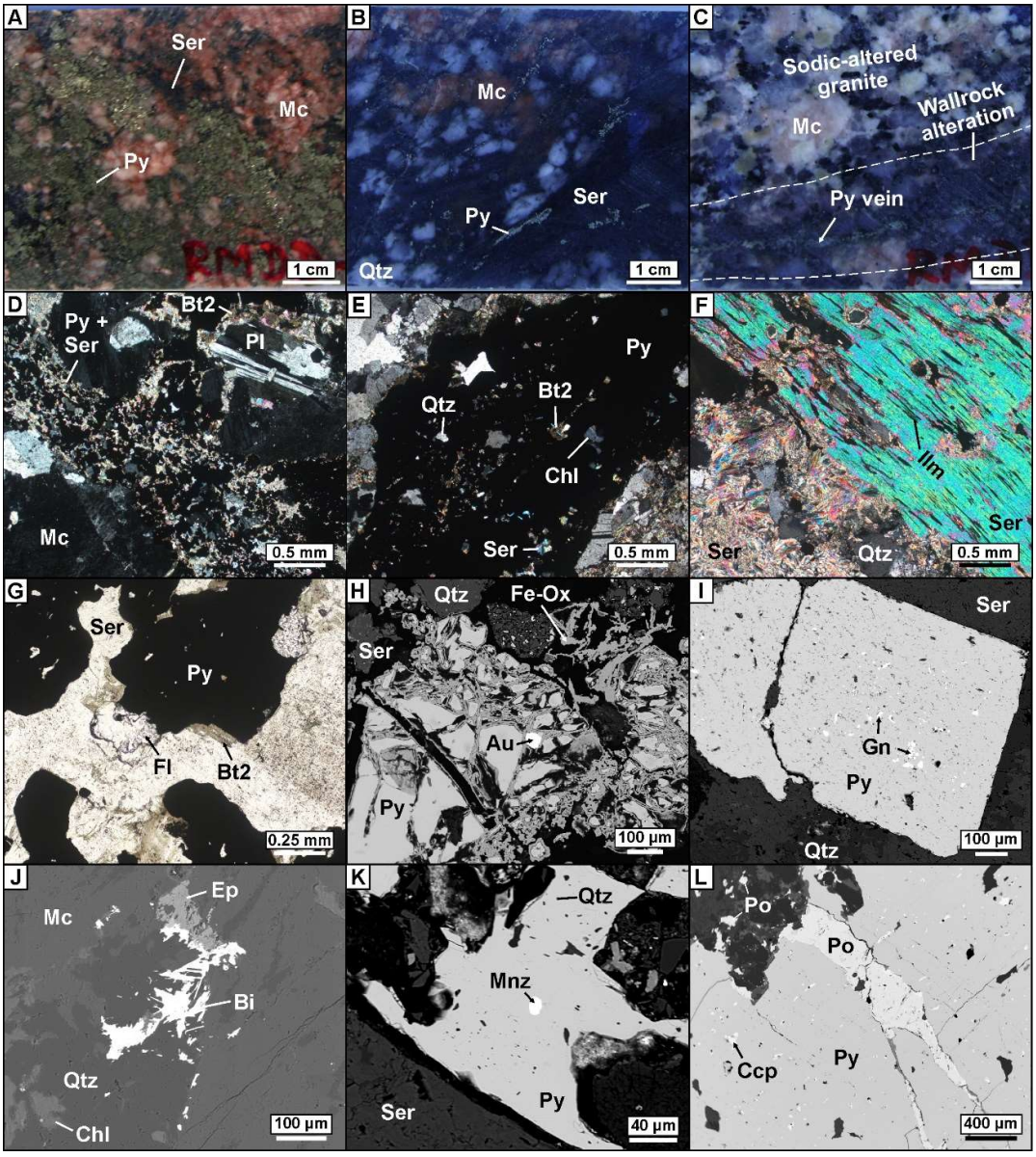

Figure 5.8 – Sericitic alteration zones in the deeper hydrothermal system of the Rosa de Maio deposit. A-C) Sericitized granites displaying typical disseminated pyrite and pyrite-filled veinlets. D-H) Photomicrographs of sericitic alteration zones in plane-polarized (PPL) and cross-polarized light (XPL). D) Veinlet of pyrite and sericite with minor hydrothermal biotite crosscutting the altered biotite granite. E) Pyrite containing inclusions of chlorite, hydrothermal biotite, quartz, and sericite. F) Ilmenite formed along cleavage planes of magmatic biotite pseudomorph altered to muscovite. G) Fluorite associated with pyrite and sericite. H-L) Backscattered electron (BSE) images of sericitic alteration zones. H) Native gold associated with pyrite. Iron oxides along pyrite fractures are interpreted as products of post-hydrothermal supergene alteration. I) Galena inclusions within euhedral pyrite. J) Native bismuth in association with sericitic alteration zone. K) Hydrothermal monazite occurring as an inclusion within pyrite. L) Pyrrhotite filling fractures in pyrite, which contains inclusions of chalcopyrite. Py = pyrite, Ser = sericite, Mc = microcline, Bt2 = hydrothermal biotite, Pl = plagioclase, Qtz = quartz, Chl = chlorite, Ilm = ilmenite, Fl = fluorite, Au = native gold, Fe-Ox = iron oxide, Gn = galena, Bi = native bismuth, Ep = epidote, Mnz = monazite, Po = pyrrhotite, Ccp = chalcopyrite. Abbreviations after Whitney and Evans (2010).

5.4.3 Shallower hydrothermal system

The shallower hydrothermal system at the Rosa de Maio deposit (Fig. 5.4) is hosted within the older PAR granite (pre-1890 Ma) and is preserved only as remnants at surface and near-surface levels. Two alteration types are recognized: fissural to pervasive sericitic alteration and fissural (vein-controlled) silicification associated with quartz veins (Figs. 5.9 and 5.10). Gold mineralization is hosted mainly by sulfide-rich quartz veins, which may contain up to 108 g/t Au (unpublished survey report), but also sulfide-rich sericitized granites. This system is strongly overprinted by supergene processes, with weathering obliterating much of the original hydrothermal fabric (Figs. 5.9A to 5.9C). Due to its limited preservation, no clear spatial relationships or systematic zoning patterns between the alteration types have been identified.

Sericitic alteration zones are characterized by pervasive replacement of the primary assemblage in the host granite by sericite, quartz, and pyrite, with minor chalcopyrite, galena, and barite (Figs. 5.9D and 5.9E). Silicification is coeval with the development of an intense quartz–sulfide stockwork system, predominantly affecting zones at the top of the intrusion center (Fig. 5.4). Centimeter- to decimeter-scale veins form a dense network from which pervasive wallrock alteration develops (fissural to pervasive), forming silicified zones with disseminated sulfides (mainly pyrite) and minor sericite and chalcedony that extend up to a few decimeters (Figs. 5.9 and 5.10). Locally, remnants of a silica cap characterized by vuggy silica are preserved (Fig. 5.9F), with cavities commonly filled by quartz (Fig. 5.10E). Platy quartz, interpreted as pseudomorphs after bladed calcite, may also occur in quartz veins (Figs. 5.9G and 5.10F). The silicified granite is often crosscut by coarser-grained quartz veinlets (Fig. 5.10), locally displaying comb textures (Fig. 5.10A). Silicified zones typically display light gray hues, with the magmatic rock fabric completely destroyed, particularly where overprinted by supergene alteration.

Gold mineralization in the shallower hydrothermal system is also intimately associated with sulfides, predominantly pyrite (0.1-0.5% Co, 0.1-0.2% Pb; Appendix B), which occurs both disseminated in the wallrock and filling veins together with quartz (Figs. 5.9 and 5.10). The mineralized quartz-vein

assemblage typically comprises quartz + pyrite + gold ± galena ± chalcopyrite ± sericite. Galena frequently occurs as very fine-grained rounded inclusions within pyrite (Fig. 5.10I). Chalcocite and covellite coronas around pyrite are interpreted as products of post-hydrothermal supergene processes (Figs. 5.10H and 5.10I).

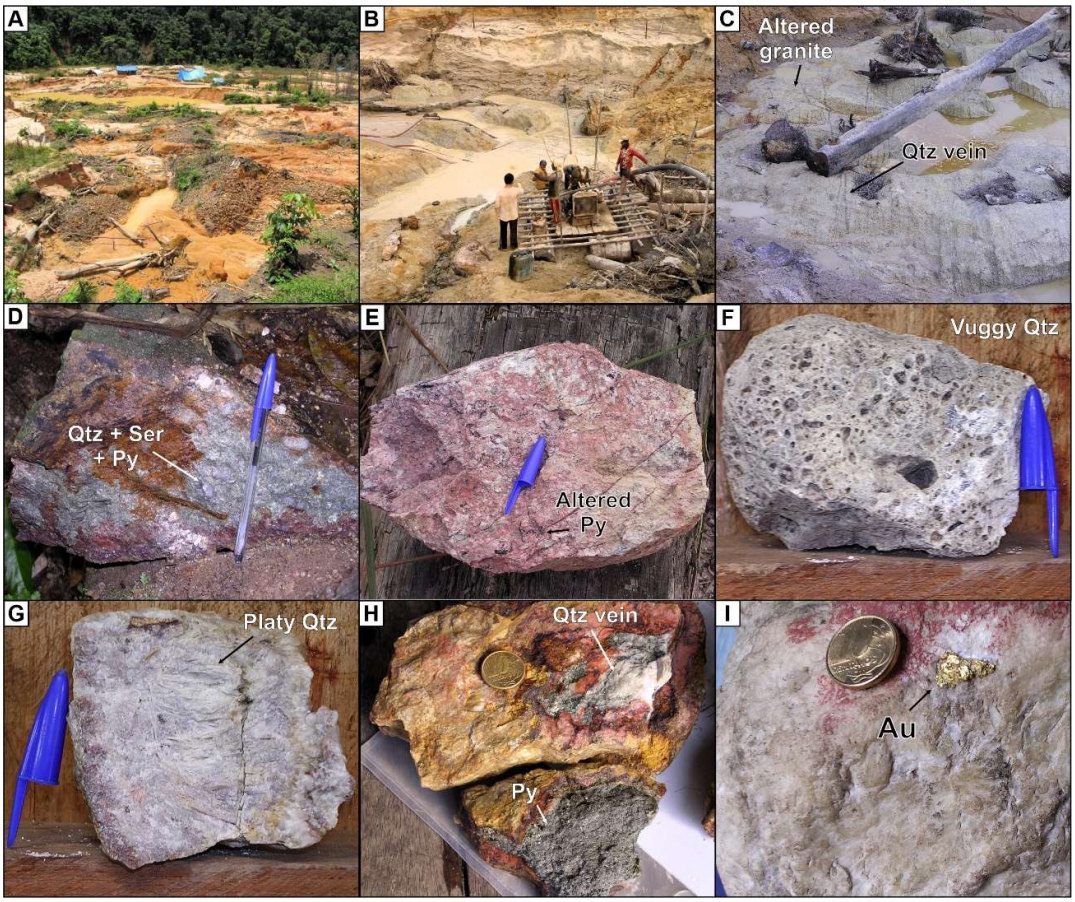

Figure 5.9 – A-B) Strongly weathered granite at the Rosa de Maio artisanal mining site (garimpo). C) Sub-parallel quartz vein system crosscutting altered and weathered granite. D) Sericitized granite composed of sericite + quartz + pyrite (MAG-RM-4). E) Sericitized granite that was subsequently weathered, with altered pyrite leaving behind cavities (MAG-RM-7). F) Strongly leached granite, resulting in vuggy quartz (LC-A-7). G) Platy quartz within a quartz vein, likely formed by replacement of bladed calcite (LC-A-2). H) Mineralized pyrite-rich quartz vein containing 10.4 g/t Au (MAG-RM-17). I) Native gold hosted in quartz vein. Qtz = quartz; Ser = sericite; Py = pyrite. Abbreviations after Whitney and Evans (2010).

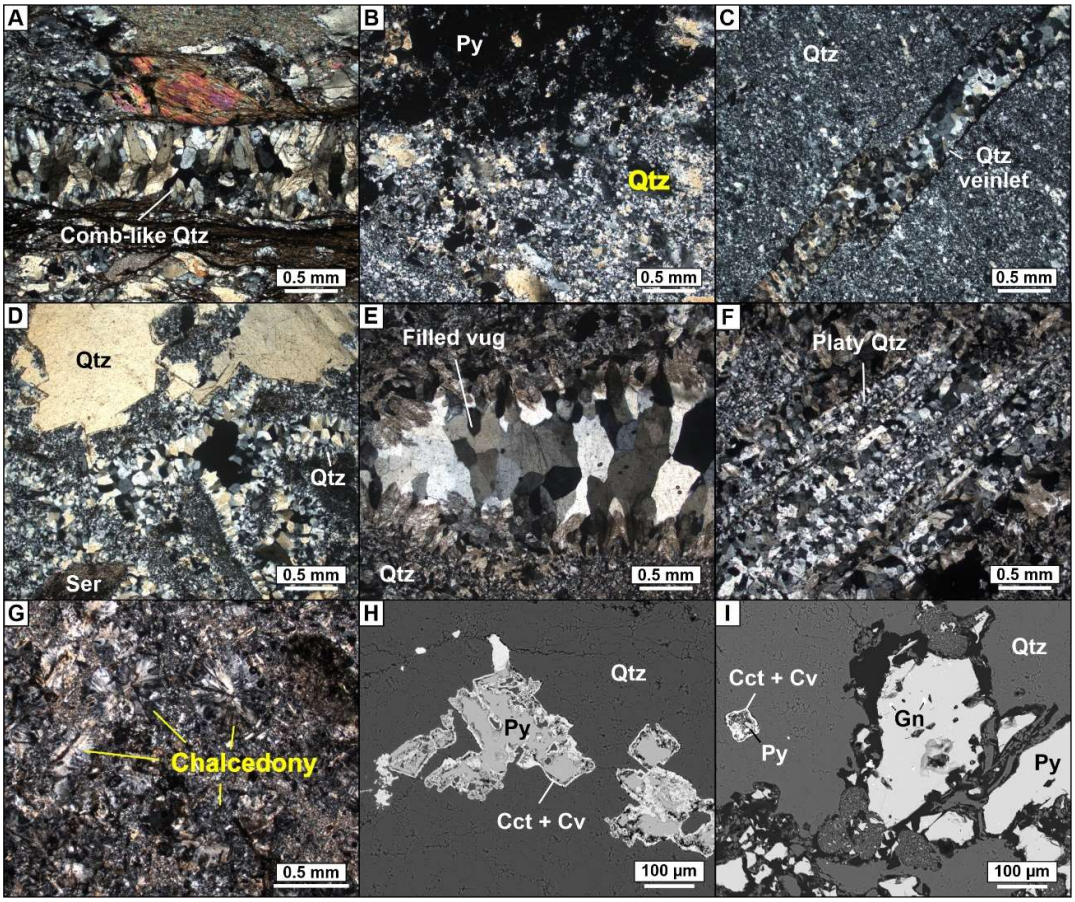

Figure 5.10 – Photomicrographs in cross-polarized light (XPL) and backscattered electron (BSE) images of quartz veins and associated silicified zones. A) Quartz veinlet with comb-like texture. B) Pyrite associated with fine-grained quartz. C) Silicified host rock crosscut by a veinlet of coarser-grained quartz. D) Quartz vein with quartz-filled cavities. E) Vug filled by quartz in vuggy silica zones. F) Platy quartz, likely formed by replacement of bladed calcite. G) Fibrous radial chalcedony. H-I) BSE images of pyrite, commonly with galena inclusions. Chalcocite and covellite rims around pyrite are interpreted as products of post-hydrothermal supergene alteration. Py = pyrite, Qtz = quartz, Ser = sericite, Gn = galena, Cct = chalcocite, Cv = covellite. Abbreviations after Whitney and Evans (2010).

5.4.4 Lithogeochemistry

Whole-rock major- and trace-element analyses of the least-altered biotite granite from the RMG (Alves et al., 2025), together with granites affected by propylitic and sericitic alteration (in both deeper and shallower hydrothermal systems) and quartz veins/silicified rocks, are presented in Appendix A. Owing to varying degrees of alteration intensity and the pervasive-to-fissural nature of some alterations, the whole-rock compositions represent only an approximation of the actual bulk chemical changes affecting the unaltered granites. Therefore, the analyses presented here reflect a range of alteration intensities and, in some

cases, are more representative of fracture infill than of pervasive alteration products.

The unaltered biotite granite from the RMG is high-silica, peraluminous to strongly peraluminous, high-K calc-alkaline to shoshonitic, ferroan, and relatively oxidized (Alves et al., 2025). Fluid interaction with this host rock in the deeper hydrothermal system promoted the following main chemical changes: (i) average Na_2O enrichment in sodic-altered and propylitized granites, mainly due to albite; (ii) CaO and MnO enrichment in propylitized granites, related to epidote, chlorite, and calcite (see section 4.2); and (iii) Fe_2O_3, Rb, and Cs enrichment in sericitized granites, linked to pyrite and sericite. In the shallower hydrothermal system, sericitized granites also show Fe_2O_3, Rb, and Cs enrichment due to pyrite and sericite, as well as Ba enrichment related to barite. Silica enrichment is typical of quartz veins and silicified granites, reflecting abundant quartz, and is accompanied by depletion of most major elements (Appendix A).

The precipitation of sulfides during propylitic and sericitic alteration, predominantly pyrrhotite and pyrite, is reflected in the higher average Fe_2O_3 contents of propylitized and sericitized samples (Fig. 5.11). Quartz veins and silicified granites show variable Fe_2O_3 contents (Fig. 5.11), consistent with variations in the modal abundance of pyrite. The close association between gold and pyrite, as observed petrographically, is also reflected in the highest Au concentrations recorded in samples associated with the sericitic alteration (from both deeper and shallower systems) and in quartz veins/silicified rocks (Fig. 5.11). In these zones, gold contents can reach up to 100 g/t (Appendix A). Geochemical data from exploration campaigns indicate average grades of ~1 g/t Au in mineralized zones, with localized values up to 108 g/t Au in quartz veins (unpublished survey report). Copper contents are highest in sericitic alteration (up to 2330 ppm, Appendix A), whereas propylitic alteration displays the highest Cu/Au ratios (Fig. 5.11).

When considered collectively, samples affected by propylitic and sericitic alteration (deeper and shallower systems), along with quartz veins and silicified granites, display a weak positive correlation between Au and Cu, Mo, Pb, and Co, as well as a stronger positive correlation between Au and Fe_2O_3, Ag, Bi, and

As (Fig. 5.11). Conversely, Au displays a negative correlation with total REE + Y (Fig. 5.11). The strong positive correlation between Fe_2O_3 and Cu (Fig. 5.11) is most likely related to the presence of chalcopyrite in the hydrothermal assemblages. Moreover, higher Cu/Au ratios correlate positively with MgO contents (Fig. 5.11).

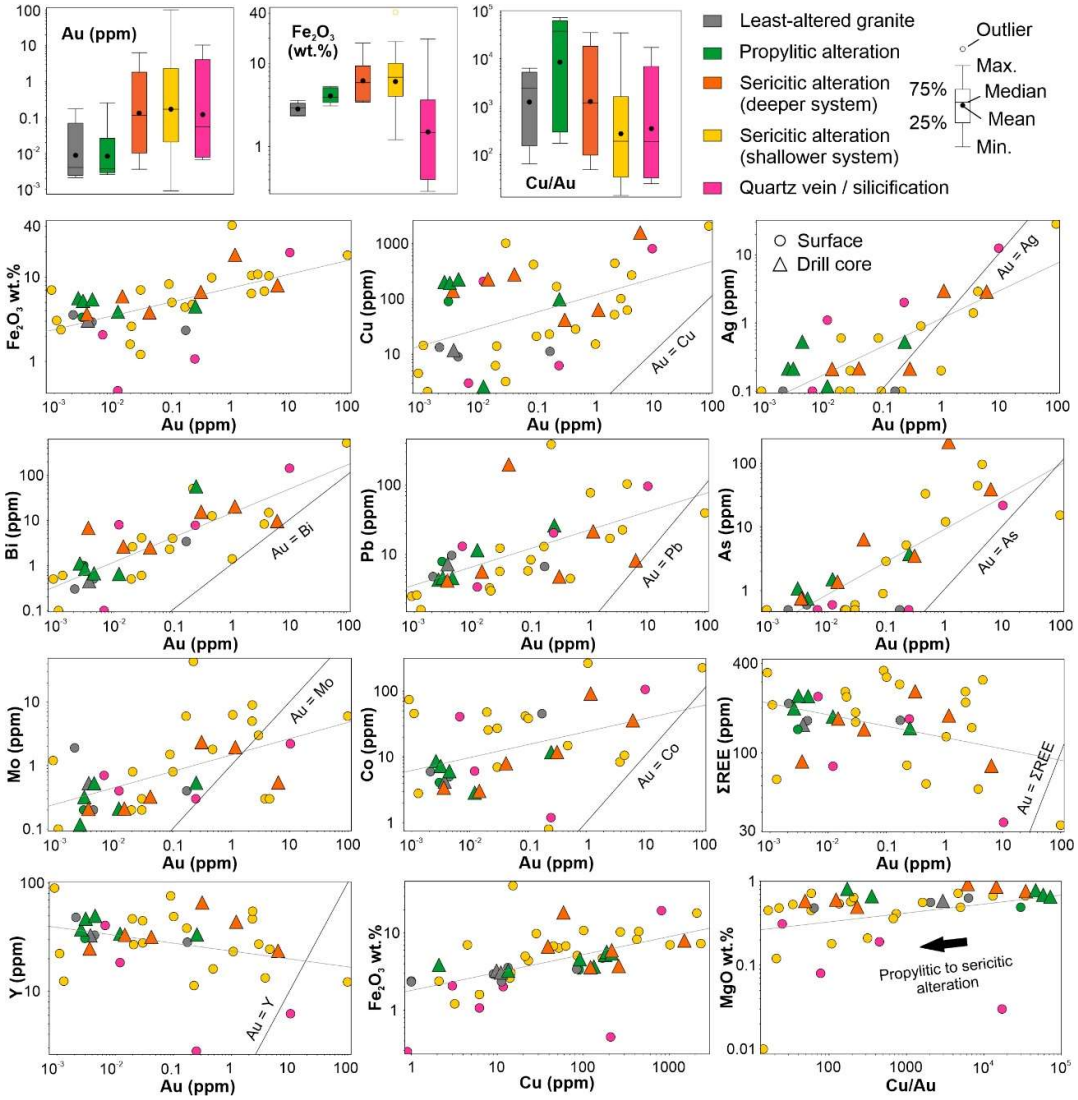

Figure 5.11 – Whole-rock major and trace element data from the Rosa de Maio deposit, including least-altered biotite granite, and rocks affected by propylitic and sericitic alteration (deeper and shallower hydrothermal systems), as well as quartz veins and silicified zones. Colored bars represent the interquartile range (central 50% of the data distribution). Plots include Au vs. Fe_2O_3, Cu, Ag, Bi, Pb, As, Mo, Co, total REE, and Y; as well as Cu vs. Fe_2O_3 and Cu/Au vs. MgO. Gray lines represent ordinary least-squares regression fits.

The REE patterns of the least-altered and propylitized granites are nearly identical, characterized by enrichment in LREE (over 100x chondrite), flat HREE patterns, and pronounced negative Eu anomalies (Fig. 5.12A). Samples

associated with sericitic alteration in the deeper hydrothermal system are overall similar, although slightly depleted in total REE, with one sample displaying a distinct negative Ce anomaly (Fig. 5.12B). Samples affected by sericitic alteration in the shallower hydrothermal system can be divided into four groups according to their REE patterns (Figs. 5.12C to 5.12E): 1. Patterns similar to those described above, slightly depleted in total REE; 2. Variable LREE enrichment (up to 300x chondrite), flat HREE, pronounced negative Eu anomalies, and weak to strong negative Ce anomalies; 3. Variable LREE enrichment (also up to 300x chondrite), weak HREE depletion, and negative Eu, Y, and Ce anomalies; and 4. Weakly enriched in LREE (~20x chondrite), flat HREE, a negative Eu anomaly, and a positive Ce anomaly (Fig. 5.12E). Negative Ce anomalies ($Ce/Ce^* < 1$) in samples affected by sericitic alteration in the shallower hydrothermal system correlate positively with P_2O_5 and Th, and negatively with K_2O, Rb, and Cs (Figs. 5.12G to 5.12K). Quartz veins and silicified rocks are variably depleted in total REE and display REE patterns with LREE enrichment, flat HREE, and negative Eu anomalies (Fig. 5.12F).

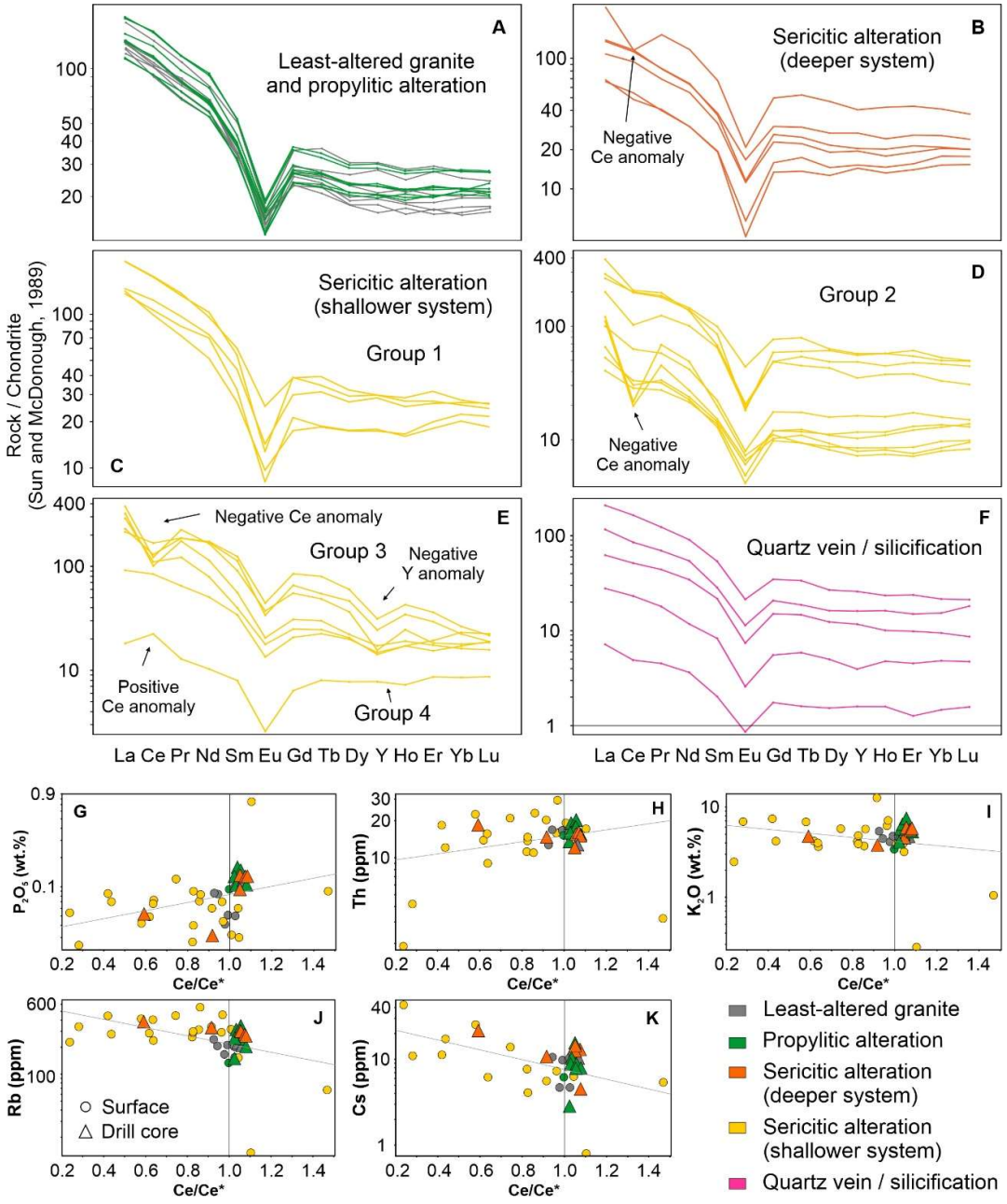

Figure 5.12 – A-F) Chondrite-normalized REE patterns from the Rosa de Maio deposit, including least-altered biotite granite, and rocks affected by propylitic and sericitic alteration (deeper and shallower hydrothermal systems), as well as quartz veins and silicified zones (normalization values from Sun and McDonough, 1989). G-K) Ce/Ce* values plotted against P_2O5, Th, K_2O, Rb, and Cs.

5.4.5 Mineral chemistry

5.4.5.1 Biotite

Chemical analyses (EPMA) of hydrothermal biotite from the Rosa de Maio deposit are presented in Appendix B. Hydrothermal biotite occurs mostly in

potassic-altered zones as fine-grained aggregates, frequently replacing coarser-grained magmatic biotite (Fig. 5.6K). It is consistently associated with the magmatic biotite, which is often the only mafic mineral in the rock-forming assemblage of the unaltered biotite granite (Alves et al., 2025). Both magmatic and hydrothermal biotite are classified as annite, following the classification scheme proposed by Tischendorf et al. (2007), with the latter being slightly richer in MgO on average (Fig. 5.13A, Appendix B). Hydrothermal biotite has Mg# values ranging from 30 to 39, MnO contents between 0.1-1.1 wt.%, and F contents between 0.2-1.0 wt.% (Appendix B). It displays lower TiO_2 contents (frequently <1 wt.%) compared to the magmatic biotite (2-5 wt.% TiO_2; Alves et al., 2025). Using the discrimination diagram of Nachit et al. (2005), hydrothermal biotite predominantly plots in the secondary/neoformed field, while magmatic biotite plots in the primary and reequilibrated fields (Fig. 5.13B). For more details on the magmatic biotite of the RMG, see Alves et al. (2025).

5.4.5.2 Epidote

Chemical analyses (EPMA) of epidote from the Rosa de Maio deposit are presented in Appendix B. Epidote is closely associated with the propylitic alteration stage of the Rosa de Maio deposit, being often indicative of this alteration. It occurs as fine-grained anhedral to euhedral crystals, commonly replacing magmatic and hydrothermal biotite in the early propylitic alteration and progressively replacing plagioclase in intensely propylitized granites (Fig. 5.7E). It also occurs filling fractures together with albite. Most epidote in all altered rock types of the Rosa de Maio deposit is classified as epidote *sensu stricto*, with a high Fe^{3+} component (X_{Ep} > 0.5) and compositions close to the epidote end-member (Fig. 5.13C). In biotite granites affected by intense propylitic alteration, epidote compositions are between X_{Ep} = 0.54-0.99 (mean = 0.83), while in those affected by incipient propylitic alteration, values are between X_{Ep} = 0.63-0.87 (mean = 0.76). In biotite granites affected by propylitic alteration with incipient sericitic overprint, epidote compositions are between X_{Ep} = 0.46-0.87 (mean = 0.63, Fig. 5.13C, Appendix B). MnO contents in epidote from altered biotite granites range from 0.09 to 1.18 wt.% (Appendix B).

5.4.5.3 Chlorite

Chemical analyses (EPMA) of chlorite from the Rosa de Maio deposit are presented in Appendix B. Chlorite is abundant in propylitic alteration zones and occurs subordinately in sericitic alteration zones of the deeper hydrothermal system. In all these alteration zones, it is classified as chamosite (19-42% clinochlore, 56-80% chamosite, and 0-3% pennantite, Wiewióra and Weiss, 1990, Appendix B) and trioctahedral (type I) Fe-chlorite (Zane and Weiss, 1998; Fig. 5.13D). Chlorite from the Rosa de Maio deposit has Mg# values ranging from 19 to 42, SiO_2 contents from 22 to 27.7 wt.%, Al_2O_3 contents from 15.7 to 20.8 wt.%, and MnO contents from 0.2 to 1.5 wt.% (Appendix B). These compositional variations do not reflect distinct hydrothermal alteration stages but rather result from localized heterogeneities in fluid composition and other factors controlling chlorite composition, such as fluid-rock interaction and minor variations in the fluid's chemical evolution within the hydrothermal system.

Chemical chlorite geothermometry

Formation temperatures of chlorite from 8 samples of propylitic and sericitic alteration zones in the deeper hydrothermal system were calculated using seven chlorite geothermometers proposed by various authors (Fig. 5.13E, Cathelineau and Nieva, 1985; Kranidiotis and MacLean, 1987; Cathelineau, 1988; Kavalieris et al., 1990; Zang and Fyfe, 1995; El-Sharkawy, 2000). These geothermometers employ empirical approaches based on tetrahedral aluminum occupancy or octahedral vacancy. Temperatures were calculated using the WinCcac program (Yavuz et al., 2015). Despite the wide range of temperatures obtained from all the seven geothermometers (as low as ~150 °C and up to ~400 °C, Fig. 5.13E, Appendix B), the formation temperatures for chlorite in propylitic alteration zones are typically between 367 °C and 167 °C, while those in sericitic alteration zones (deeper system) are between 325 °C and 161 °C. These intervals correspond to the combined interquartile range (values between the first and third quartiles) obtained from all seven geothermometers (Fig. 5.13E, Appendix B). The similar range of formation temperatures reflects comparable chlorite compositions in the propylitic and sericitic alteration zones of the RMG.

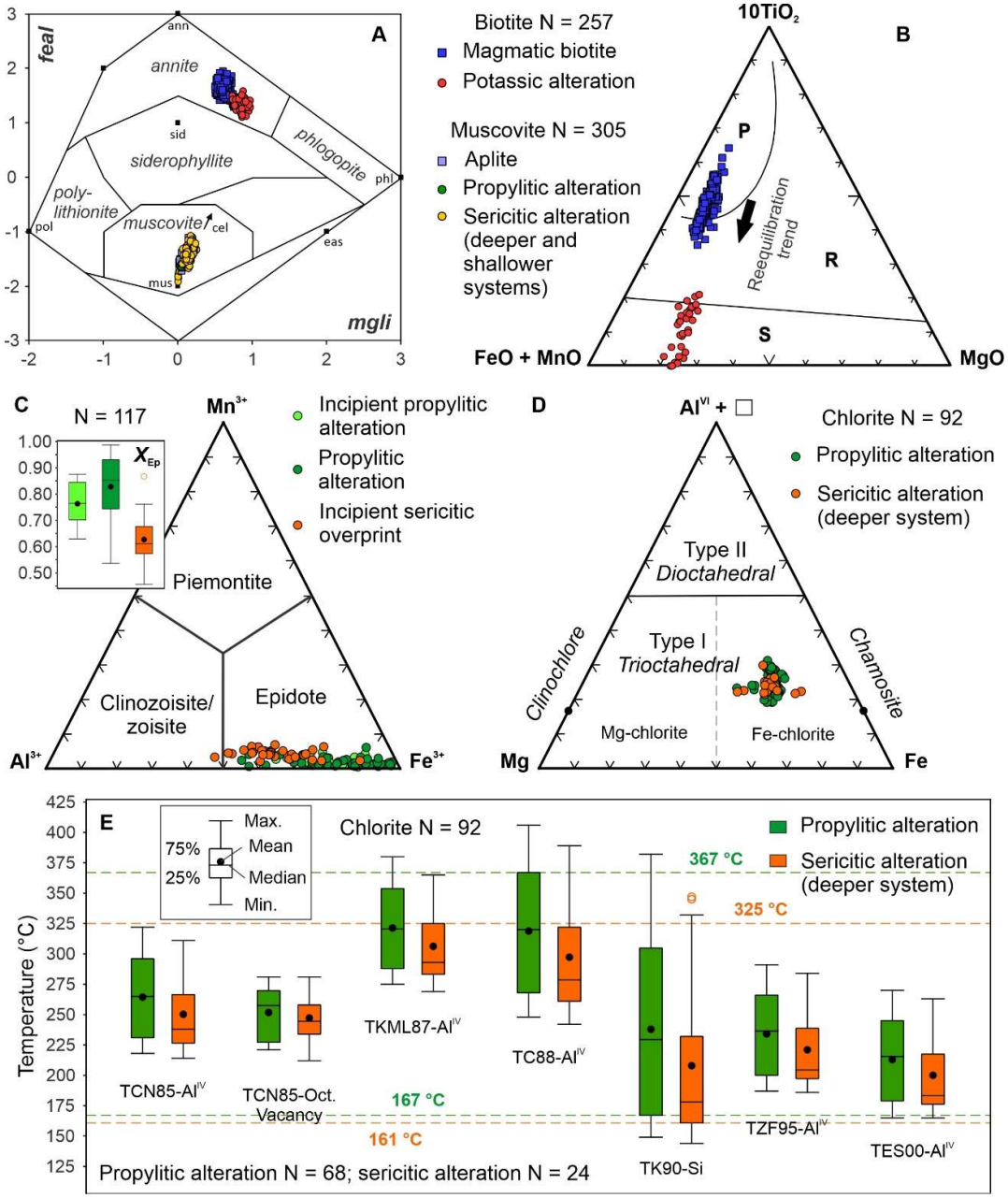

Figure 5.13 – Chemical composition of biotite, muscovite, epidote, and chlorite from the Rosa de Maio deposit. A) True mica classification diagram by Tischendorf et al. (2007). B) Biotite discrimination diagram by Nachit et al. (2005). C) Al^{3+}-Mn^{3+}-Fe^{3+} ternary classification diagram for epidote. D) Chlorite classification diagram by Zane and Weiss (1998). E) Chlorite geothermometers based on tetrahedral aluminum occupancy or octahedral vacancy: TCN85-Al^{IV} and TCN85-Oct. Vacancy (Cathelineau and Nieva, 1985), TKML87-Al^{IV} (Kranidiotis and MacLean, 1987), TC88-Al^{IV} (Cathelineau, 1988), TK90-Si (Kavalieris et al., 1990), TZF95-Al^{IV} (Zang and Fyfe, 1995), and TES00-Al^{IV} (El-Sharkawy, 2000).

5.4.5.4 Muscovite

Chemical analyses (EPMA) of magmatic and hydrothermal muscovite from the Rosa de Maio deposit are presented in Appendix B. Magmatic muscovite

is a minor phase (~1% modal abundance) in the biotite granite and a rock-forming mineral (~3-15% modal abundance) in the muscovite-rich aplite (Alves et al., 2025). Sericite is widespread in sericitic alteration zones of both the deeper and shallower hydrothermal systems. In these zones, it occurs as fine-grained lamellae replacing primary feldspars and biotite, commonly associated with quartz and pyrite, and also forms pseudomorphs after magmatic biotite (Fig. 5.8).

According to the classification scheme of Tischendorf et al. (2007), both magmatic muscovite from the aplite and sericite from propylitic and sericitic alteration zones (deeper and shallower systems) are classified as muscovite (Fig. 5.13A). In the discrimination diagram of Miller et al. (1981), magmatic muscovite plots mostly in the primary field, whereas sericite from propylitic and sericitic alteration zones plots predominantly in the secondary field, defining a trend of progressively decreasing Na/Mg ratios from magmatic to hydrothermal muscovite (Fig. 5.14A). Based on major-element compositions, muscovite from the RMG can be roughly divided into three groups: (i) late-magmatic muscovite from the aplite (high Na_2O, low MgO), (ii) hydrothermal muscovite from propylitized granites (intermediate to low Na_2O and MgO), and (iii) hydrothermal muscovite from sericitic alteration zones (low Na_2O, high MgO). Muscovite from sericitic alteration in the deeper and shallower systems is largely similar, although the shallower-system muscovite tends to be slightly richer in F (Fig. 5.14F). In variation diagrams as a function of MgO, all muscovite compositions from the Rosa de Maio deposit show negative correlations with Na_2O and Al_2O_3, and positive correlations with SiO_2, FeO, and F (Figs. 5.14B to 5.14F). TiO_2 contents in both magmatic and hydrothermal muscovite are below 1 wt.% (Appendix B). Due to the low modal abundance of muscovite in the biotite granite and the scarcity of absolutely unaltered samples, muscovite compositions from this rock type are not presented.

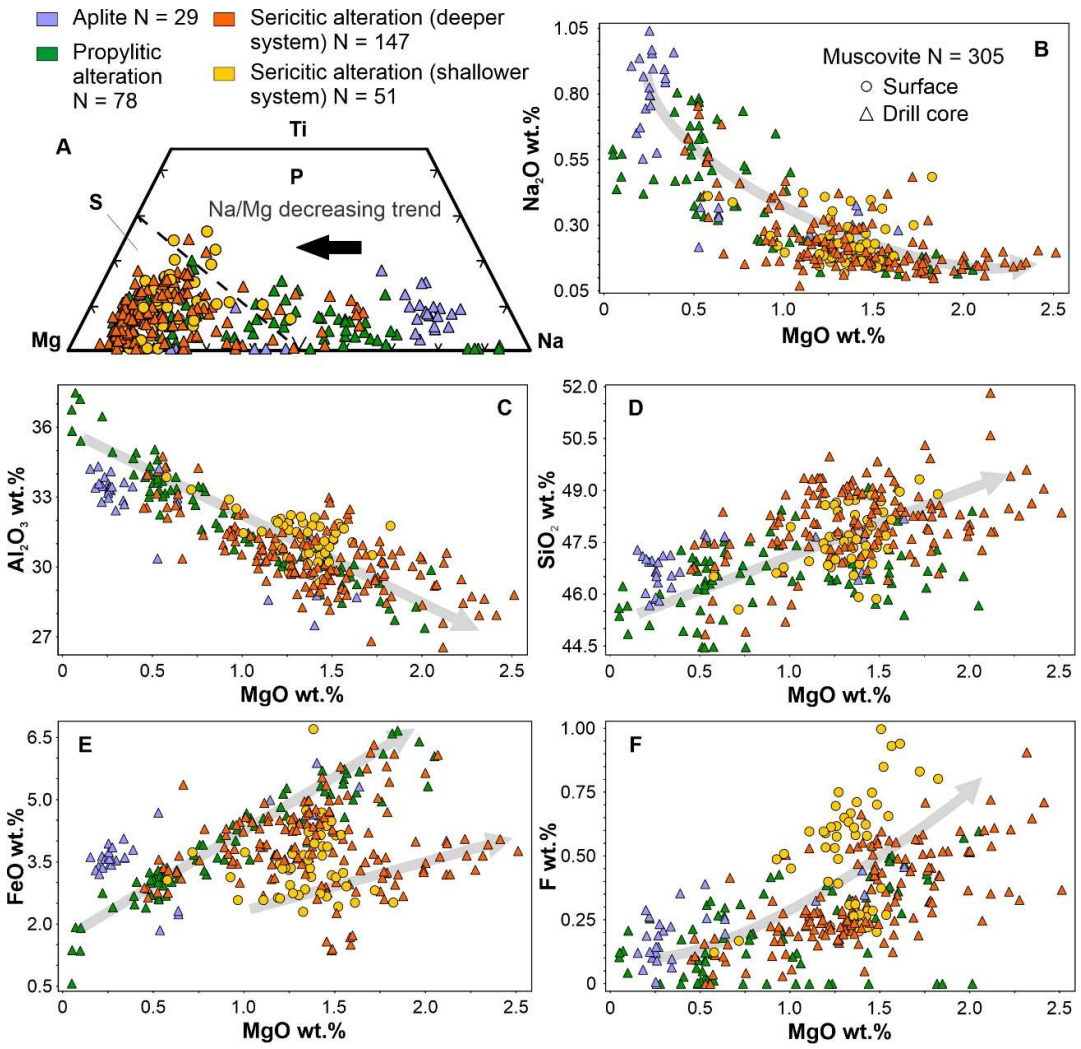

Figure 5.14 – Chemical composition of muscovite/sericite from the Rosa de Maio deposit, including the muscovite-rich aplite, as well as propylitic and sericitic (deeper and shallower hydrothermal systems) alteration zones. A) Muscovite discrimination diagram by Miller et al. (1981). P = primary and S = secondary/neoformed. B) to F) MgO plotted against Na_2O, Al_2O_3, SiO_2, FeO, and F.

5.4.6 Ar-Ar geochronology

5.4.6.1 Muscovite

$^{40}Ar/^{39}Ar$ analyses were conducted on muscovite from a quartz vein at the Rosa de Maio deposit (384780E, 9371510N, UTM zone 21M, WGS84), associated with the shallower hydrothermal system. These analyses are presented in Appendix C.

A total of 16 steps yielded apparent ages ranging from 891 to 1826 Ma (Fig. 5.15, Appendix C). The first four steps (14.65% of released ^{39}Ar) are discordant and show significant date variability, forming a staircase-like pattern

ascending towards the plateau (typical of radiogenic ^{40}Ar loss), whereas the last three steps (2.12% of released ^{39}Ar) display an upward date drift following the plateau. These seven steps (16.77% of released ^{39}Ar) were excluded from the plateau age calculation. The remaining nine steps (83.2% of released ^{39}Ar) are concordant and define a flat $^{40}Ar/^{39}Ar$ spectrum, with apparent ages between 1789 and 1826 Ma, yielding a well-defined plateau age of 1808.3 ± 7.1 Ma (MSWD = 1.1, N = 9 steps; Fig. 5.15, Appendix C). Ca/K ratios are low across all steps, consistent with mineral chemistry data of hydrothermal muscovite from the Rosa de Maio deposit (see Appendix C).

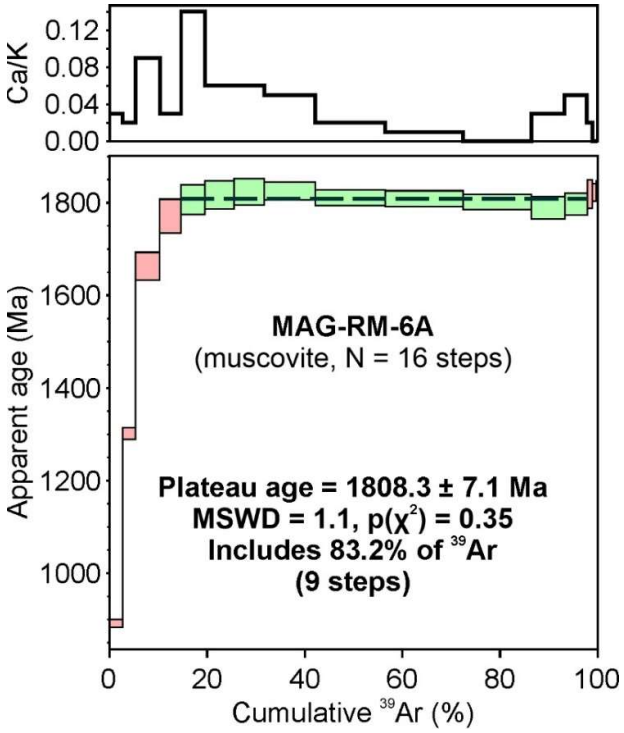

Figure 5.15 – $^{40}Ar/^{39}Ar$ release spectrum for step-heated muscovite from a quartz vein of the Rosa de Maio deposit, with corresponding Ca/K ratios for each step. Steps shaded in green indicate the $^{40}Ar/^{39}Ar$ apparent ages included in the plateau age calculation. The step thickness represents 2σ uncertainties. N = number of steps, MSWD = mean square weighted deviation, and $p(\chi^2)$ = probability of fit.

5.4.7 Sulfur isotope geochemistry

Sulfur isotope data for pyrite from the sericitic alteration in the deeper hydrothermal system and from a sulfide-rich quartz vein in the shallower hydrothermal system of the Rosa de Maio deposit are presented in Table 5.2. Pyrite, the dominant sulfide phase in both sericitic assemblages and sulfide-rich quartz veins, is closely associated with gold mineralization. It is chemically

homogeneous in major elements across the two hydrothermal systems (Appendix B) and yields $\delta^{34}S$ values within a narrow range, from +0.5 ± 0.2‰ to +1.3 ± 0.1‰ (Table 5.2).

Table 5.2 – Sulfur isotope data for pyrite from the sericitic alteration (deeper system) and from a sulfide-rich quartz vein at surface.

Sample	Mineral	Stage / rock type	$\delta^{34}S_{V\text{-}CDT}$ (‰)	2σ (‰)
RM-DD2-79.10	Pyrite	Sericitic alteration (deeper system)	+0.8	0.1
RM-DD2-79.10	Pyrite	Sericitic alteration (deeper system)	+1.3	0.1
MAG-RM-17	Pyrite	Quartz vein (shallower system)	+0.5	0.2
MAG-RM-17	Pyrite	Quartz vein (shallower system)	+0.6	0.2

5.5 Discussions

5.5.1 Evolution of hydrothermal alteration and gold mineralization in the deeper system

The hydrothermal evolution of the deeper system in the Rosa de Maio deposit is characterized by the following paragenetic sequence, inferred from textural equilibria and replacement relationships: sodic, potassic, propylitic, and sericitic alteration (Fig. 5.4). This sequence, established through detailed petrography, is further supported by lithogeochemistry and mineral chemistry data. Together, these data provide insights into fluid composition and the physicochemical conditions that prevailed during fluid-rock interaction, vein and veinlet infill, and gold mineralization.

5.5.1.1 Sodic and potassic alterations

The sodic alteration stage represents the onset of hydrothermal activity in the Rosa de Maio deposit and is characterized by a pervasive, though relatively low fluid/rock ratio interaction between high-temperature, alkaline magmatic fluids – exsolved during the late stages of the RMG magmatic system – and the porphyritic biotite granite, the dominant rock type of the intrusion. This Na enrichment during the transition from the magmatic to the hydrothermal phase is consistent with the magmatic evolution of the RMG proposed by Alves et al. (2025). The highest Na_2O contents in magmatic muscovite from the aplite (Fig. 5.14B), which represents the last magmatic stage prior to hydrothermal activity, also indicate progressive Na enrichment in the melt. This Na was subsequently

partitioned into the exsolving fluids that triggered sodic alteration. Hydrothermal muscovite from propylitized to sericitized granites shows progressively lower Na_2O contents (Fig. 5.14B), suggesting higher Na availability during earlier alteration stages. As the hydrothermal fluid evolved chemically, it shifted towards K-richer compositions, leading to the formation of hydrothermal K-feldspar and the replacement of magmatic biotite (Mg# = 22-36) by hydrothermal biotite with higher Mg# values (30-39, Figs. 5.13A).

5.5.1.2 Propylitic alteration

The propylitic alteration represents a fissural to pervasive stage, characterized by higher fluid/rock ratios and cooler hydrothermal fluids. Chemical chlorite geothermometry yields low to intermediate temperatures ranging from ~370 to 170 °C (Fig. 5.13E), consistent with the wide temperature range typical of propylitic alteration in magmatic-hydrothermal systems (200-350 °C; *e.g.,* Norman et al., 1991). This stage marks the onset of significant sulfide precipitation, dominated by pyrrhotite and chalcopyrite. The presence of pyrrhotite, rather than pyrite, suggests lower sulfur fugacity conditions compared to the subsequent sericitic alteration stage, where pyrite is the dominant sulfide. Precipitation of chalcopyrite in the absence of gold accounts for the highest whole-rock Cu/Au ratios in propylitized samples (Fig. 5.11). The presence of carbonate (mainly calcite) and fluorite suggests precipitation from a F-rich, aqueo-carbonic fluid. This is further supported by the commonly higher F contents of hydrothermal muscovite with lower Na/Mg ratios from propylitic and sericitic alteration zones compared to magmatic muscovite (Fig. 5.14F). Although the primary rock-forming assemblage of the host granite is typically replaced by epidote and Fe-chlorite (chamosite), the accessory assemblage remains largely unaltered, which is reflected in REE patterns similar to those of the unaltered host rock (Fig. 5.12A).

5.5.1.3 Sericitic alteration

The sericitic alteration represents a structurally-controlled stage (fissural with associated peripheral alteration halos extending up to a few decimeters), characterized by high fluid/rock ratios, relatively acidic conditions, and temperatures slightly lower than those of the propylitic stage. Chemical chlorite

geothermometry yields temperatures ranging from ~325 to 160 °C (Fig. 5.13E). This stage is closely associated with gold mineralization. The predominance of pyrite over pyrrhotite suggests higher average sulfur fugacity conditions relative to the previous stage. The sericitic alteration is marked by abundant sulfide precipitation, including pyrite, chalcopyrite, and galena, with co-precipitation of native bismuth and gold (electrum). This association is consistent with the positive correlations between Au and Fe_2O_3, Cu, Pb, Bi, and Ag, as well as other chalcophile elements such as As, Mo, and Co in whole-rock samples (Fig. 5.11). Hydrothermal muscovite from this stage is commonly enriched in SiO_2 and FeO, and depleted in Al_2O_3 compared to magmatic muscovite (Fig. 5.14), suggesting that the fluid from which it crystallized was relatively enriched in Fe and Si. This interpretation is consistent with the abundant co-precipitation of pyrite and quartz at this stage. The inverse correlation between SiO_2/FeO and Al_2O_3 is interpreted to reflect the substitution of Al by Si and Fe in the tetrahedral and octahedral sites of the muscovite crystal lattice, respectively. A second generation of pyrrhotite, occurring at pyrite rims and/or filling fractures within pyrite grains (Fig. 5.8L), may indicate fluctuating sulfur fugacity conditions during the waning stages of the sericitic alteration. The REE patterns of sericitic alteration samples suggest that most of the primary REE-bearing assemblage remained unmodified. However, a sample displaying a negative Ce anomaly (Fig. 5.12B) indicates partitioning of Ce, likely caused by the breakdown of primary monazite and subsequent precipitation of neoformed hydrothermal monazite depleted in Ce. The occurrence of hydrothermal monazite as inclusions in pyrite within sericitic assemblages further supports this interpretation (Fig. 5.8K).

This sequence of hydrothermal alterations identified in the deeper system of the Rosa de Maio deposit is similar to that of other Au(-Cu) deposits in the TMP, including the Batalha (1883 ± 4 Ma; Juliani et al., 2002), Palito (1883 ± 11 Ma; Echeverri Misas, 2010, 2015), and São Jorge (1983 ± 8 Ma and 1891 ± 3 Ma; Lamarão et al., 2002; Borges et al., 2009). In these deposits, gold mineralization is generally associated with sericitic alteration, occurring as disseminated ore and within sulfide-rich quartz veins in stockwork systems.

5.5.2 Significance of the shallower hydrothermal system

The hydrothermal evolution of the shallower system in the Rosa de Maio deposit is characterized by acidic and cooler fluids, expressed initially by sericitic alteration and subsequently by silicification. Silicification is structurally controlled (mostly fissural), associated with high fluid/rock ratios, and linked to the development of a quartz stockwork system along fractures in the brittle apical roof zones of the intrusion center. At near-surface levels, both barren quartz veins and sulfide-rich, high-grade gold-bearing veins were formed. Gold mineralization also displays a strong spatial association with pyrite, both in sulfide-rich sericitized zones and in quartz veins.

The REE patterns of near-surface sericitized samples are significantly distinct from those of other alteration types, displaying both negative and positive anomalies, as well as negative Y anomalies (Fig. 5.12). These anomalies are interpreted as the result of interaction between hydrothermal fluids and the host rock's accessory assemblage (*e.g.*, monazite, xenotime, apatite), and/or the neoformation of REE-bearing phases that precipitated from fluids infilling fractures. We interpret that the hydrothermal fluids scavenged REEs from the primary accessory phases, mobilizing them as complexes with fluoride, sulfate, and carbonate – important ligands known to enhance REE solubility in aqueous fluids (Wood, 1990; Banks et al., 1994; Migdisov and Williams-Jones, 2014; Migdisov et al., 2016). During precipitation of pyrite, these REE complexes were likely destabilized, triggering the co-precipitation of hydrothermal monazite and other REE-bearing carbonates, phosphates, and halides not identified in this study (*e.g.*, bastnäsite, parisite, fluocerite). In these hydrothermal fluids, Ce is assumed to occur as Ce^{4+}, favoring its incorporation into these newly formed REE-bearing phases and resulting in positive Ce anomalies. Conversely, samples lacking these Ce^{4+}-rich phases typically display negative Ce anomalies. Samples with no Ce anomaly, only negative Ce anomalies, or both negative Ce and Y anomalies are interpreted to reflect progressive alteration of the host rock, involving the breakdown of monazite and xenotime. Because Ce anomalies are essentially absent in other hydrothermal alterations of the Rosa de Maio deposit, they provide a useful geochemical proxy for assessing the sericitic alteration in the shallower system. In Ce/Ce* vs P_2O_5 and Th diagrams, sericitized samples

display a negative correlation, interpreted to reflect the progressive alteration and breakdown of magmatic monazite. In contrast, a positive correlation between Ce/Ce* and K_2O, Rb, and Cs is interpreted as the increasing abundance of sericite/muscovite, typical of this alteration. The processes controlling the formation of hydrothermal REE-bearing phases, and thereby producing the Ce and Y anomalies in sericitized samples, are likely the same processes that led to the precipitation of pyrite and gold, consistent with the close association between gold mineralization and sericitic alteration. Quartz veins and silicified rocks commonly have lower total REE contents but preserve REE patterns similar to those of unaltered rocks. This suggests that silicification did not significantly modify the original accessory assemblage, and that the lower REE concentrations simply reflect dilution by abundant quartz and sulfide phases.

Remnants of vuggy silica indicate leaching by strongly acidic fluids (Hedenquist et al., 2000), suggesting that a silica cap (now largely eroded) developed in the upper levels of the shallower system. The occurrence of platy quartz in quartz veins (interpreted as pseudomorphs after bladed calcite) further indicates that boiling took place (Simmons and Browne, 1990; Etoh et al., 2002). These features are characteristic of epithermal systems in the TMP, such as the Botica Velha (V3), Coringa, and Chapéu de Sol deposits (Juliani et al., 2005; Aguja-Bocanegra, 2013; Guimarães et al., 2021; Juliani et al., 2021). In this area, the absence of volcanic host rocks (typically associated with epithermal deposits) likely reflects erosion of Orosirian volcanic sequences formed at upper crustal levels. Volcanic rocks of the Iriri Group (1.89–1.87 Ga), however, are preserved farther north and host the Doze de Outubro deposit (~50 km northeast of Rosa de Maio), which is recognized as an epithermal system (Juliani et al., 2021). The erosion of such volcanic sequences, potentially linked to epithermal systems, may have contributed to the formation of placer deposits, including the Rosa de Maio *garimpo*, a process also proposed for other alluvial and colluvial deposits in the TMP (Juliani et al., 2005).

The spatial correlation between the deeper and shallower systems, together with similar trends in lithogeochemistry, comparable muscovite compositions from sericitic alteration, and overlapping $\delta^{34}S$ values of pyrite, suggests that the two systems are genetically linked. Thus, the Rosa de Maio

deposit likely represents the evolution of a deeper magmatic-hydrothermal system, associated with epizonal magmatism represented by the RMG, that is genetically linked to a shallower hydrothermal system at near-surface levels. This evolution reflects a fluid pathway from high-temperature, alkaline magmatic fluids to progressively cooler and more acidic fluids, with gold mineralization occurring in both systems.

5.5.3 Potential mechanism of gold precipitation and sulfur source

The strong spatial association between gold and pyrite in the Rosa de Maio deposit, supported by petrographic evidence (Fig. 5.8) and reflected in the positive correlation between Au and Fe_2O_3 in whole-rock data (Fig. 5.11), along with the low temperatures (<350 °C) estimated for the sericitic alteration in the deeper system, suggest that gold was transported as bisulfide complexes, such as $Au(HS)$ or $Au(HS)_2^-$ (Stefánsson and Seward, 2004; Williams-Jones et al., 2009). Gold precipitation was likely triggered by a decrease in the activity of HS^- in the fluid, which destabilized the gold-bisulfide complexes. This decrease in HS^- concentration may have been driven by the sulfidation of Fe-bearing minerals in the host rocks, predominantly magmatic biotite, which is Fe-rich (Mg# values between 22 and 36; Alves et al., 2025), and, to a lesser extent, hydrothermal biotite and chlorite formed during previous alteration stages. Sulfidation of these phases likely released Fe^{2+} into the fluid, which reacted with gold-bisulfide complexes, promoting the co-precipitation of pyrite and gold during sericitic alteration in the deeper system. A similar process likely occurred in the shallower system, where cooling may have further contributed to gold deposition in sericitized rocks and quartz veins. Nonetheless, more data are required to fully assess this proposed mechanism of precipitation.

The source of sulfur in the HS^- ligand responsible for gold transport can be constrained using sulfur isotope data. Pyrite from the deeper and shallower systems yields a restricted range of $\delta^{34}S$ values, between +0.5 and +1.3‰. These values are consistent with a magmatic sulfur source, as mantle-derived sulfur typically has $\delta^{34}S$ values clustering around 0‰, and granitic rocks with minimal assimilation of sedimentary rocks generally fall within the range of 1.0 ± 6.1 ‰ (Seal, 2006). Furthermore, the $\delta^{34}S$ values are within the typical range of

porphyry hydrothermal systems (1-8‰; Seal, 2006). Thus, the sulfur isotope data from pyrite support a dominantly magmatic origin for sulfur in the Rosa de Maio deposit.

5.5.4 Timing constraints on the age of gold mineralization

Geochronological data from Alves et al. (2025) and this study provide key constraints on the timing of magmatic-hydrothermal activity associated with primary gold mineralization in the Rosa de Maio deposit. Alves et al. (2025) reported weighted mean Pb-Pb dates of 1894 ± 9 Ma and 1889 ± 11 Ma for zircon, and 1886 ± 13 Ma for monazite, from unaltered biotite granites of the RMG. All these dates are interpreted as crystallization ages. Given the genetic association between gold mineralization and the RMG magmatism, these U-Pb crystallization ages (*ca.* 1890 Ma) are interpreted as the maximum age of mineralization for the Rosa de Maio deposit. In contrast, the $^{40}Ar/^{39}Ar$ plateau age of 1808.3 ± 7.1 Ma obtained in this study from muscovite in a quartz vein of the shallower hydrothermal system is interpreted as the minimum age of mineralization, as it is either coeval with or postdates the gold mineralization. However, considering that U-Pb dates of zircon and monazite typically record early magmatic crystallization, and that the $^{40}Ar/^{39}Ar$ date in muscovite could record the latest hydrothermal activity, the ~80 Myr gap between these dates is unrealistically long for the duration of a single deposit.

Instead, assuming that muscovite closure temperatures for the K-Ar system are typically between ~350-400 °C (Reiners et al., 2018; Harrison et al., 2009), the muscovite date could represent: a (i) cooling age, *i.e.*, a period between fully open-system and fully-closed system behavior in which radiogenic ^{40}Ar is only partially retained (Dodson, 1973, 1979); (ii) isotopic resetting during a post-mineralization thermal event; or (iii) a younger mineralizing event linked to a magmatism not yet recognized in the area. Option (i) would require the Rosa de Maio system to have remained above ~350–400 °C for ~80 Myr at shallow crustal levels before cooling below closure temperatures by 1808 ± 7 Ma, which is unrealistic. More plausibly, the muscovite date may reflect ^{40}Ar loss and isotopic reequilibration caused by reheating during emplacement of younger intrusions. Supporting this interpretation, two undated intrusions located ~8 km

northeast and southeast of the RMG, assigned to the Maloquinha Suite (1.87-1.86 Ga), might have provided sufficient heat to reset the isotopic system. Alternatively, the younger muscovite date could record a distinct mineralizing magmatism not yet documented due to limited geological mapping. In either case, it is noteworthy that in other gold deposits of the TMP, $^{40}Ar/^{39}Ar$ and Pb-Pb dates in muscovite and sulfides linked to ore stages are significantly younger than the crystallization ages of their associated magmatic rocks (*e.g.*, Echeverri-Misas, 2015; Silva Junior et al., 2015; Biondi et al., 2018; see Juliani et al., 2021).

We therefore suggest that gold mineralization at the Rosa de Maio deposit occurred either shortly after the emplacement of the RMG at *ca.* 1890 Ma or at *ca.* 1808 Ma. The younger $^{40}Ar/^{39}Ar$ age of 1808 ± 7 Ma is best explained as either isotopic resetting during a later thermal event, most likely associated with intrusions of the Maloquinha Suite, or a younger mineralizing magmatism not yet identified in the area.

5.5.5 Comparison with other Au-rich and Au-only deposit types

The Rosa de Maio gold deposit is essentially a magmatic-hydrothermal deposit, formed by the exsolution of hydrothermal fluids during the late stages of magmatic evolution, which initiated the hydrothermal system. While it shares some features with orogenic gold deposits, such as its occurrence in an accretionary orogen, and structurally controlled mineralization hosted in sulfide-rich quartz veins (Groves et al., 1998; Groves et al., 2003), it lacks important characteristics typical of orogenic gold systems. An important feature of the Rosa de Maio deposit is that the ore fluids and associated hydrothermal alteration are directly linked to a causative intrusion, consistent with its magmatic-hydrothermal origin. In contrast, orogenic gold deposits are commonly related to metamorphic fluids sourced from devolatilization of subducted slabs, which migrate along deep crustal faults/shear zones during prograde metamorphism (Groves et al., 1998; Groves et al., 2003; Goldfarb and Groves, 2015, Groves et al., 2020). These features commonly associated with orogenic gold systems are absent in the Rosa de Maio area.

The Rosa de Maio deposit also displays characteristics that overlap with those of IRGS (Thompson et al., 1999; Lang and Baker, 2001; Hart, 2007). Both

are genetically associated with granitic intrusions emplaced in post-collisional continental arc settings and are characterized by fracture-controlled gold mineralization (fissure veins) in cupola zones, typically with low Cu/Au ratios. However, the Rosa de Maio deposit does not display the characteristic Au-Bi-Te-W metal association of IRGS (Lang and Baker, 2001; Hart and Goldfarb, 2005; Hart, 2007). Although native bismuth occurs in sericitic alteration zones of the Rosa de Maio deposit and W ore contents average 170 ppm (reaching up to 1800 ppm; Appendix A), Bi concentrations are generally low (<60 ppm), and no scheelite or tellurium-bearing phases have been identified. Moreover, the metal zoning patterns typical of IRGS, such as those described in the Tintina Gold Province (Hart and Goldfarb, 2005; Hart, 2007), are absent in the Rosa de Maio deposit. The Tapajós Mineral Province also lacks a regional Au-W-Sn metallogenic association, which is frequently related to IRGS (Thompson et al., 1999; Hart, 2007). Most notably, IRGS are typically linked to reduced intrusions (Thompson et al., 1999; Lang and Baker, 2001; Hart and Goldfarb, 2005; Hart, 2007), whereas the Rosa de Maio deposit is associated with relatively oxidized magmas (Alves et al., 2025).

Alternatively, the Rosa de Maio deposit also shows several similarities with Au-rich porphyry deposits (Sillitoe, 2000; Kesler et al., 2002; Chiaradia, 2021). These deposits are generally related to oxidized, intermediate to felsic intrusions, and may be linked not only to calc-alkaline magmas but also to high-K calc-alkaline to alkaline magmas emplaced in post-collisional to extensional tectonic settings at shallow crustal levels (Chiaradia, 2021; Park et al., 2021). These characteristics are all compatible with the Rosa de Maio deposit. Moreover, in contrast to Cu-rich porphyry deposits, Au-rich porphyry deposits are commonly associated with magmatic rocks with low Sr/Y and La/Yb ratios (Chiaradia, 2021, 2022), which also characterize the RMG (Alves et al., 2025). Additional features consistent with Au-rich porphyry deposits include telescoped alteration zoning patterns, where shallower alteration (*e.g.*, sericitic) overprints deeper hydrothermal assemblages (*e.g.*, potassic), and a dominant magmatic origin for the mineralizing fluids (Sillitoe, 2000, 2010). Although the Rosa de Maio deposit lacks some classical features of porphyry systems, such as extensive propylitic alteration and gold mineralization associated with potassic zones (Sillitoe, 2000),

we interpret it to be more closely associated with Au-rich porphyry-style deposits. Moreover, the spatial association between the shallower and deeper hydrothermal systems, together with their magmatic fluid signatures (inferred from sulfur isotopes), suggests that the shallow system may represent remnants of an epithermal environment genetically related to the deeper porphyry-style hydrothermal system. Further investigation, however, is required to determine whether this potential epithermal overprint corresponds to a high-, intermediate-, or low-sulfidation subtype.

5.6 Conclusions

The Rosa de Maio deposit is an epizonal magmatic-hydrothermal gold deposit located in the northwestern Tapajós Mineral Province. It is genetically linked to the Rosa de Maio Granite (RMG, *ca.* 1890 Ma; Alves et al., 2025), which comprises high-K calc-alkaline and relatively oxidized biotite granites (Alves et al., 2025) associated with the late- to post-collisional Parauari magmatism (1.89-1.87 Ga).

Two distinct hydrothermal systems are recognized in the Rosa de Maio deposit: a deeper system and a shallower, near-surface system. The hydrothermal evolution of the deeper system is characterized by a sequence of four alteration types: sodic, potassic, propylitic, and sericitic alteration. Hydrothermal activity initiated with the exsolution of high-temperature, alkaline aqueous fluids during the late stages of magmatic evolution in the apical zones of the RMG. These fluids promoted pervasive Na metasomatism, followed by K metasomatism of the host biotite granite. Propylitic alteration subsequently overprinted previously formed hydrothermal assemblages in proximal zones of the intrusion center, marking the onset of sulfide precipitation (pyrrhotite ± chalcopyrite) from cooler hydrothermal fluids (~370-170 °C). This stage was followed by fissural to pervasive sericitic alteration, characterized by pyrite, quartz, and sericite formed from similarly low-temperature fluids (~325-160 °C). Sericitic alteration zones are marked by abundant sulfide precipitation, including pyrite, chalcopyrite, and galena, as well as minor native bismuth. The shallower hydrothermal system, genetically linked to the deeper one, is characterized by sericitic alteration and silicification, associated with the development of a

stockwork system composed of quartz and pyrite-quartz veins in the upper, distal portions of the intrusion center. Gold mineralization shows a strong spatial association with sulfides, predominantly pyrite, and is characterized by low Cu/Au ratios. It occurs in both systems within sericitic alteration zones and sulfide-rich quartz veins, present both as vein infill and disseminated in altered wallrock.

Gold was most likely transported as bisulfide complexes and precipitated mainly due to sulfidation of Fe-bearing minerals in the host rocks, causing the co-precipitation of gold and pyrite. Cooling further contributed to gold deposition in upper distal zones of the system. The source of sulfur and mineralizing fluids in the Rosa de Maio deposit is predominantly magmatic, although additional data are required to fully constrain precipitation mechanisms.

Gold mineralization occurred either shortly after emplacement of the RMG at *ca.* 1890 Ma or around 1808 Ma. The younger $^{40}Ar/^{39}Ar$ plateau age of 1808 ± 7 Ma, obtained from muscovite in a quartz vein of the shallower system, is interpreted as either the result of isotopic resetting during a younger thermal event (possibly linked to the Maloquinha magmatism, 1.87-1.86 Ga), or as evidence of a younger mineralizing magmatism not yet identified in the area.

Overall, the deeper hydrothermal system of Rosa de Maio shows a closer affinity to Au-rich porphyry-style deposits, whereas the genetically related shallower system likely represents remnants of an epithermal mineralization, now largely eroded. The Rosa de Maio deposit thus provides another example of a granite-hosted gold deposit in the Tapajós Mineral Province, sharing several similarities with other Au(–Cu) deposits such as Batalha, Palito, and São Jorge, including the timing and nature of the associated magmatism, hydrothermal evolution, and styles of mineralization.

5.7 Acknowledgements

This study was financially supported by the Brazilian Council for Scientific and Technological Development (CNPq, grants 555063/2006-2 and 313172/2020-0) and the Coordenação de Aperfeiçoamento de Pessoal de Nível Superior – Brazil (CAPES, Finance Code 001). This work was also made possible by a scholarship granted by CNPq (168366/2018-5) to Pedro Victor F. de S. Alves.

CAPÍTULO 6
CONCLUSÕES

6 CONCLUSÕES

Os resultados apresentados nesta tese indicam as seguintes conclusões:

1. As intrusões Rosa de Maio, Bandeirantes e Maués hospedam depósitos de ouro magmático-hidrotermais na porção noroeste da Província Mineral do Tapajós. As rochas magmáticas associadas são granitos de alta sílica, peraluminosos a fortemente peraluminosos, de afinidade cálcio-alcalina de alto K, ricos em Fe e relativamente oxidados;

2. Cristalização fracionada desempenhou um papel crucial na evolução magmática dessas intrusões, levando à seguinte sequência de diferenciação: de rochas tonalíticas/granodioríticas ricas em biotita para monzo-/sienogranitos com biotita, e finalmente para aplitos graníticos com muscovita de composição sienogranítica a álcali-feldspato granítica. Os magmas parentais que originaram o biotita granito e os aplitos ricos em muscovita possuem composições semelhantes às dos enclaves microgranitoides. Esses enclaves foram transportados para porções superiores da câmara magmática devido à convecção e/ou mistura caótica. A ocorrência de zonamento oscilatório em fenocristais de plagioclásio das rochas do Granito Rosa de Maio provavelmente resulta da injeção de novo magma nesse reservatório magmático dinâmico;

3. As condições de fugacidade de oxigênio durante a cristalização do biotita granito, a rocha mais abundante e de maior volume no Granito Rosa de Maio, são estimadas como estando acima do buffer NNO;

4. O magmatismo Parauari nesta região provavelmente persistiu por alguns milhões de anos, sendo representado pelo magmatismo cálcio-alcalino de alto K a shoshonítico das intrusões Bandeirantes e Rosa de Maio, que foram alojadas por volta de 1907 Ma e 1890 Ma, respectivamente, em um contexto tectônico tardi- a pós-colisional dentro da evolução tectônica da Província Mineral do Tapajós. Esse magmatismo sucedeu um período de magmatismo de arco controlado por subducção, representado pela sequência magmática mais antiga (*older magmatic sequence,* 2,0–1,95 Ga);

5. As fontes do Granito Rosa de Maio envolvem contribuições tanto de material juvenil quanto de rochas crustais da sequência magmática mais antiga,

semelhantes às do Grupo Jacareacanga (2,2–2,0 Ga) e do Complexo Cuiú-Cuiú (2,04–1,99 Ga). Isso é refletido nos xenocristais de zircão com idades em torno de 2120–2190 Ma e 2030 Ma;

6. Saturação magmática em sulfetos pode ter sido um fator de controle de primeira ordem sobre a fertilidade aurífera do depósito Rosa de Maio, embora sejam necessários mais dados para avaliar adequadamente essa hipótese;

7. Foram identificados dois sistemas hidrotermais distintos no depósito Rosa de Maio: um sistema mais profundo e outro mais raso, formado próximo à superfície. A evolução hidrotermal do sistema mais profundo é caracterizada por uma sequência de quatro alterações: alteração sódica, potássica, propilítica e sericítica. A atividade hidrotermal iniciou-se com a exsolução de fluidos aquosos alcalinos de alta temperatura durante os estágios finais da evolução magmática nas zonas apicais do Granito Rosa de Maio. Esses fluidos foram responsáveis por um metasomatismo sódico pervasivo, seguido por um metasomatismo potássico que afetou o biotita granito hospedeiro. A alteração propilítica subsequente sobrepôs-se, em zonas proximais do centro da intrusão, às alterações hidrotermais previamente formadas, marcando o início da precipitação de sulfetos (pirrotita ± calcopirita) a partir de fluidos hidrotermais mais frios (~370–170 °C). Esse estágio foi seguido por alteração sericítica fissural a pervasiva, caracterizada por pirita, quartzo e sericita formados a partir de fluidos igualmente de baixa temperatura (~325–160 °C). As zonas de alteração sericítica são marcadas pela abundante precipitação de sulfetos, incluindo pirita, calcopirita e galena, além de bismuto nativo subordinado.

O sistema hidrotermal mais raso, geneticamente relacionado ao mais profundo, é caracterizado por alteração sericítica e silicificação, esta associada ao desenvolvimento de um sistema *stockwork* composto por veios de quartzo e quartzo-pirita nas porções superiores e distais do centro da intrusão. A mineralização aurífera apresenta forte associação espacial com sulfetos, predominantemente pirita, e é caracterizada por baixos teores de Cu/Au. Ela ocorre em ambos os sistemas, hospedada em zonas de alteração sericítica e em veios de quartzo ricos em sulfetos, tanto como *infill* em veios quanto disseminada nas rochas encaixantes alteradas;

8. Nos sistemas hidrotermais do depósito Rosa de Maio, o ouro foi provavelmente transportado na forma de complexos sulfetados e precipitou principalmente devido à sulfetação de minerais portadores de Fe nas rochas hospedeiras, resultando na coprecipitação de ouro e pirita. O processo de resfriamento também contribuiu para a deposição de ouro em zonas distais superiores do sistema. Dados adicionais, no entanto, são necessários para uma melhor compreensão dos mecanismos de precipitação. A fonte de enxofre e dos fluidos mineralizantes no depósito Rosa de Maio é predominantemente magmática;

9. A mineralização aurífera ocorreu pouco após o alojamento do Granito Rosa de Maio, em *ca.* 1890 Ma, ou por volta de 1808 Ma. A idade de *plateau* $^{40}Ar/^{39}Ar$ mais jovem, de 1808 ± 7 Ma, obtida em muscovita de um veio de quartzo do sistema mais raso, é interpretada como resultado de reequilíbrio isotópico causado por um evento térmico posterior (possivelmente relacionado ao magmatismo Maloquinha, 1,87–1,86 Ga), ou, alternativamente, como evidência de um magmatismo mineralizante mais jovem ainda não identificado na área;

10. O sistema hidrotermal mais profundo do depósito Rosa de Maio apresenta maior afinidade com depósitos do tipo pórfiro ricos em Au, enquanto o sistema raso geneticamente relacionado provavelmente corresponde a remanescentes de uma mineralização epitermal, já parcialmente erodida. Dessa maneira, o depósito Rosa de Maio constitui mais um exemplo de depósito aurífero hospedado em granitos na Província Mineral do Tapajós, compartilhando diversas semelhanças com outros depósitos de Au(–Cu) da província, como o Batalha, Palito e São Jorge. Essas semelhanças incluem o tipo de magmatismo associado, assim como o *timing* de alojamento, a evolução hidrotermal e estilos de mineralização.

REFERÊNCIAS BIBLIOGRÁFICAS

Abdel-Rahman, A.-F.M. (1994). Nature of biotites from alkaline, calc-alkaline, and peraluminous magmas. Journal of Petrology, v. 35(2), 525-541. https://doi.org/10.1093/petrology/35.2.525

Aguja-Bocanegra, M.A. (2013). Mineralizações epitermal low-sulfidation e do tipo pórfiro superpostas associadas ao magmatismo félsico de 1,88 Ga na parte norte da Província Mineral do Tapajós (PA). Tese de Mestrado, Universidade de São Paulo, São Paulo, Brazil, 235 p.

Almeida, F.F.M., Nogueira Filho, J. V. 1959. Reconhecimento geológico no rio Aripuanã – Boletim Div. Geol. Mineral. Rio de Janeiro: DNPM, 1959, p. 1-43.

Alves, C. L., Rizzotto, G. J., Rios, F. S., & Barros, M. A. D. S. A. (2020). The Orosirian Cuiú-Cuiú magmatic arc in Peixoto de Azevedo domain, Southern of Amazonian craton. Journal of South American Earth Sciences, 102, 102648. https://doi.org/10.1016/j.jsames.2020.102648

Alves, P. V. F. S., Botelho, N. F., Souza, V. S., Cunha, L. M., Gonçalves, G., Coaquira, J. A. H., Cuadros, F. A. J., Yokoyama, E. (2025). Geochemistry, U-Pb geochronology, and Sm-Nd isotopes of the granitic rocks associated with the Rosa de Maio gold deposit in the Tapajós Mineral Province, Brazil: Magmatic evolution, source characterization, and implications for magma fertility. Precambrian Research, 427, 107883. https://doi.org/10.1016/j.precamres.2025.107883

Aquino L.B.M. (2013). Geologia e geocronologia do granito palito e de sua mineralização, depósito aurífero do palito, Província Aurífera do Tapajós, Itaituba-PA. Final Project, Faculdade de Geologia. Instituto de Geociência-UFPA, 70p.

Araújo Neto, H. 1996. Mineralizações de ouro: Tapajós-Amaná-Parauari-Abacaxis, (Pará/Amazonas). Brasília: CPRM, 203 p.

Assunção, R. F., & Klein, E. L. (2014). The Moreira Gomes deposit of the Cuiú-Cuiú goldfield: Fluid inclusions and stable isotope constraints and implications for the genesis of granite-hosted gold mineralization in the Tapajós Gold Province, Brazil. Journal of South American Earth Sciences, 49, 85-105. https://doi.org/10.1016/j.jsames.2013.11.004

Banks, D. A., Yardley, B. W. D., Campbell, A. R., & Jarvis, K. E. (1994). REE composition of an aqueous magmatic fluid: a fluid inclusion study from the Capitan Pluton, New Mexico, USA. Chemical Geology, 113(3-4), 259-272. https://doi.org/10.1016/0009-2541(94)90070-1

Bender, K. M., Bühn, B. M., Mota-e-Silva, J., Chaves, J. G. S. (2007). $^{32}S/^{34}S$ isotope analyses by laser ablation MC–ICPMS: method and application. In: VI South American Symposium on Isotope Geology, San Carlos de Bariloche [CD-ROM].

Biondi, J. C., Borgo, A., Chauvet, A., Monié, P., Bruguier, O., & Ocampo, R. (2018). Structural, mineralogical, geochemical and geochronological constraints on ore genesis of the gold-only Tocantinzinho deposit (Para State, Brazil). Ore Geology Reviews, 102, 154-194. https://doi.org/10.1016/j.oregeorev.2018.08.007

Bizinella, G.A., Santiago, A.F., Santos, A. dos, Borges, F.R., Souza, F.J.C., Godoy, H.K., Yamaguti, H.S., Oliveira, J.R. & Oliveira, R.L. 1980. Projeto Tapajós-Sucunduri. Relatório Final. Manaus: CPRM/DNPM , v.1B, 357-700.

Borges, R. M. K., Dall'Agnol, R., Lamarão, C. N., Figueiredo, M. A. B. M., Leite, A. A. D. S., Barros, C. E. D. M., & Costi, H. T. (2009). Petrografia, química mineral e processos hidrotermais associados ao depósito de ouro São Jorge, Província Aurífera do Tapajós, Cráton Amazônico.

Borgo, A., Biondi, J. C., Chauvet, A., Bruguier, O., Monie, P., Baker, T., Ocampo, R., Friedman, R., & Mortensen, J. (2017). Geochronological, geochemical and petrographic constraints on the Paleoproterozoic Tocantinzinho gold deposit (Tapajos Gold Province, Amazonian Craton-Brazil): Implications for timing, regional evolution and deformation style of its host rocks. Journal of South American Earth Sciences, 75, 92-115. https://doi.org/10.1016/j.jsames.2017.02.003

Carneiro, C. D. C., Juliani, C., Carreiro-Araujo, S. A., Monteiro, L. V. S., Crosta, A. P., & Fernandes, C. M. D. (2018). New crustal framework in the amazon craton based on geophysical data: evidences of deep east-west trending suture zones. IEEE Geoscience and Remote Sensing Letters, 16(1), 20-24. https://doi.org/10.1109/LGRS.2018.2867551

Cassini, L. V., Moyen, J. F., Cellier, G., de Freitas, B., Juliani, C., & Laurent, O. (2022). Towards the fertility trend: Unraveling the economic potential of igneous suites through whole-rock and zircon geochemistry (example from the Tapajós mineral Province, Northern Brazil). Ore Geology Reviews, 142, 104643. https://doi.org/10.1016/j.oregeorev.2021.104643

Cassini, L.V. (2016). Alteração hidrotermal e gênese da mineralização aurífera do Patrocínio, Província Mineral do Tapajós (PA). São Paulo: Dissertação de Mestrado, Instituto de Geociências, Universidade de São Paulo, 152 p.

Cassini, L.V., Moyen, J.F., Juliani, C. (2020). Orosirian magmatism in the Tapajós Mineral Province (Amazonian Craton): the missing link to understand the onset of Paleoproterozoic tectonics. Lithos, 356-357, 105350. https://doi.org/10.1016/j.lithos.2019.105350

Cathelineau, M. (1988). Cation site occupancy in chlorites and illites as a function of temperature. Clay minerals, 23(4), 471-485. https://doi.org/10.1180/claymin.1988.023.4.13

Cathelineau, M., & Nieva, D. (1985). A chlorite solid solution geothermometer the Los Azufres (Mexico) geothermal system. Contributions to Mineralogy and Petrology, 91, 235-244. https://doi.org/10.1007/BF00413350

Chiaradia, M. (2015). Crustal thickness control on Sr/Y signatures of recent arc magmas: an Earth scale perspective. Scientific reports, 5(1), 8115. https://doi.org/10.1038/srep08115

Chiaradia, M. (2020). Gold endowments of porphyry deposits controlled by precipitation efficiency. Nature Communications, 11(1), 248. https://doi.org/10.1038/s41467-019-14113-1

Chiaradia, M. (2021). Magmatic controls on metal endowments of porphyry Cu-Au deposits, in: Ali Sholeh, Rui Wang, Tectonomagmatic influences on metallogeny and hydrothermal ore deposits: A tribute to Jeremy P. Richards (Volume I). SEG Special Publications, 24, 1-16. https://doi.org/10.5382/SP.24.01

Chiaradia, M. (2022). Distinct magma evolution processes control the formation of porphyry Cu–Au deposits in thin and thick arcs. Earth and Planetary Science Letters, 599, 117864. https://doi.org/10.1016/j.epsl.2022.117864

Chiaradia, M., Ulianov, A., Kouzmanov, K., & Beate, B. (2012). Why large porphyry Cu deposits like high Sr/Y magmas?. Scientific reports, 2(1), 685. https://doi.org/10.1038/srep00685

Cordani, U.G. 2017. História geológica do Cráton Amazônico. Belém: Anais do 15º Simpósio de Geologia da Amazônia, SBG-NO, p. 11-17.

Costa, M. A., & Rios, F. J. (2022). The gold mining industry in Brazil: A historical overview. Ore Geology Reviews, 148, 105005. https://doi.org/10.1016/j.oregeorev.2022.105005

Coutinho, M.G.N. (Ed.). 2008. Província Mineral do Tapajós: geologia, metalogenia e mapa previsional para ouro em SIG. Rio de Janeiro: CPRM. v. 1. 375 p.

Dall'Agnol, R., Rämö, O. T., de Magalhães, M. S., & Macambira, M. J. B. (1999). Petrology of the anorogenic, oxidised Jamon and Musa granites, Amazonian Craton: implications for the genesis of Proterozoic A-type granites. Lithos, 46(3), 431-462. https://doi.org/10.1016/S0024-4937(98)00077-2

Dodson, M. H. (1973). Closure temperature in cooling geochronological and petrological systems. Contributions to Mineralogy and Petrology, 40(3), 259-274. https://doi.org/10.1007/BF00373790

Dodson, M. H. (1979). Theory of cooling ages. In Lectures in isotope geology (pp. 194-202). Berlin, Heidelberg: Springer Berlin Heidelberg. https://doi.org/10.1007/978-3-642-67161-6_14

Dyar, M. D. (2002). Optical and Mössbauer spectroscopy of iron in micas. Reviews in mineralogy and geochemistry, 46(1), 313-349. https://doi.org/10.2138/rmg.2002.46.06

Echeverri Misas, C.M., (2010). Evolução Magmática, Alteração Hidrotermal e Gênese da Mineralização de Ouro e Cobre do Palito, Província Aurífera Do Tapajós (PA). Unpublished M.Sc dissertation. University of São Paulo, Brazil, 235 p.

Echeverri Misas, C.M., (2015). Geologia e Alteração Hidrotermal nas Rochas Vulcânicas e Plutônicas Paleoproterozoicas na Porção Sul da Província Mineral do Tapajós (PA). Unpublished Ph.D thesis. University of São Paulo, Brazil 285 p.

El-Sharkawy, M. F. (2000). Talc mineralization of ultramafic affinity in the Eastern Desert of Egypt. Mineralium Deposita, 35, 346-363. https://doi.org/10.1007/s001260050246

Etoh, J., Izawa, E., Watanabe, K., Taguchi, S., & Sekine, R. (2002). Bladed quartz and its relationship to gold mineralization in the Hishikari low-sulfidation epithermal gold deposit, Japan. Economic Geology, 97(8), 1841-1851. https://doi.org/10.2113/gsecongeo.97.8.1841

Faraco, M.T.L., Carvalho, J.M.A., Klein, E.L. 1997. Carta metalogenética da Província Aurífera do Tapajós. In: Costa M.L.C., Angélica R.S. (eds.). Contribuições à Geologia da Amazônia. Belém: SBG, 1:423-437.

Fisher, C. M., Bauer, A. M., Luo, Y., Sarkar, C., Hanchar, J. M., Vervoort, J. D., Tapster, S. R., Horstwood, M., & Pearson, D. G. (2020). Laser ablation split-stream analysis of the Sm-Nd and U-Pb isotope compositions of monazite, titanite, and apatite–Improvements, potential reference materials, and application to the Archean Saglek

Block gneisses. Chemical Geology, 539, 119493. https://doi.org/10.1016/j.chemgeo.2020.119493

Frost, B.R., Frost, C.D. (2008). A geochemical classification for feldspathic igneous rocks. Journal of Petrology, 49(11):1955-1969. https://doi.org/10.1093/petrology/egn054

Georgatou, A. A., & Chiaradia, M. (2020). Magmatic sulfides in high-potassium calc-alkaline to shoshonitic and alkaline rocks. Solid Earth, 11(1), 1-21. https://doi.org/10.5194/se-11-1-2020

Gioia, S. M. C. L., & Pimentel, M. M. (2000). The Sm-Nd isotopic method in the geochronology laboratory of the University of Brasília. Anais da Academia Brasileira de Ciências, 72, 219-245. https://doi.org/10.1590/S0001-37652000000200009

Goldfarb, R. J., & Groves, D. I. (2015). Orogenic gold: Common or evolving fluid and metal sources through time. Lithos, 233, 2-26. https://doi.org/10.1016/j.lithos.2015.07.011

Goldfarb, R. J., & Pitcairn, I. (2023). Orogenic gold: is a genetic association with magmatism realistic?. Mineralium Deposita, 58(1), 5-35. https://doi.org/10.1007/s00126-022-01146-8

Gonçalves, G. O., Lana, C., Scholz, R., Buick, I. S., Gerdes, A., Kamo, S. L., Corfu, F., Marinho, M. M., Chaves, A. O., Valeriano, C., & Nalini Jr, H. A. (2016). An assessment of monazite from the Itambé pegmatite district for use as U–Pb isotope reference material for microanalysis and implications for the origin of the "Moacyr" monazite. Chemical Geology, 424, 30-50. https://doi.org/10.1016/j.chemgeo.2015.12.019

Groves, D. I., Goldfarb, R. J., Gebre-Mariam, M., Hagemann, S. G., & Robert, F. (1998). Orogenic gold deposits: a proposed classification in the context of their crustal distribution and relationship to other gold deposit types. Ore geology reviews, 13(1-5), 7-27. https://doi.org/10.1016/S0169-1368(97)00012-7

Groves, D. I., Goldfarb, R. J., Robert, F., & Hart, C. J. (2003). Gold deposits in metamorphic belts: overview of current understanding, outstanding problems, future research, and exploration significance. Economic geology, 98(1), 1-29. https://doi.org/10.2113/gsecongeo.98.1.1

Groves, D. I., Santosh, M., Deng, J., Wang, Q., Yang, L., & Zhang, L. (2020). A holistic model for the origin of orogenic gold deposits and its implications for exploration. Mineralium Deposita, 55, 275-292. https://doi.org/10.1007/s00126-019-00877-5

Guimaraes, S. B., & Klein, E. L. (2020). Geochemical and isotopic constraints on the host rocks of the magmatic-hydrothermal Coringa gold-silver (Cu–Pb–Zn) deposit of the Tapajós mineral province, amazonian craton, Brazil. Journal of South American Earth Sciences, 103, 102726. https://doi.org/10.1016/j.jsames.2020.102726

Guimarães, S. B., Klein, E. L., Harris, C., & Costa, I. S. L. (2021). Metallogenesis of the orosirian epithermal coringa gold-silver (Cu-Pb-Zn) deposit, southeastern Tapajós mineral Province, Amazonian craton, Brazil. Ore Geology Reviews, 128, 103908. https://doi.org/10.1016/j.oregeorev.2020.103908

Hao, H., Park, J. W., & Campbell, I. H. (2022). Role of magma differentiation depth in controlling the Au grade of giant porphyry deposits. Earth and Planetary Science Letters, 593, 117640. https://doi.org/10.1016/j.epsl.2022.117640

Harrison, T. M., Célérier, J., Aikman, A. B., Hermann, J., & Heizler, M. T. (2009). Diffusion of ^{40}Ar in muscovite. Geochimica et Cosmochimica Acta, 73(4), 1039-1051. https://doi.org/10.1016/j.gca.2008.09.038

Hart, C. J. (2007). Reduced intrusion-related gold systems. Mineral Deposits of Canada: A synthesis of Major deposit types, district metallogeny, the Evolution of geological provinces, and exploration methods: Geological Association of Canada, Mineral Deposits Division, Special Publication, 5, 95-112.

Hart, C. J. R., & Goldfarb, R. J. (2005). Distinguishing intrusion-related from orogenic gold systems. In New Zealand Minerals Conference Proceedings (Vol. 2005, pp. 125-133).

Hedenquist, J. W., Arribas R., A., & Gonzalez-Urien, E. (2000). Exploration for epithermal gold deposits. SEG Reviews Vol. 13, 245-277. https://doi.org/10.5382/Rev.13.07

Ishihara, S. (1977). The magnetite-series and ilmenite-series granitic rocks. Mining geology, 27(145), 293-305. https://doi.org/10.11456/shigenchishitsu1951.27.293

Ishihara, S. (1981). The Granitoid Series and Mineralization. Economic Geology Anniversary, 75, 458-484.

Jackson, S.E., Pearson, N.J., Griffin, W.L., Belousova, E.A. (2004). The application of laser ablation inductively coupled plasma-mass spectrometry to in situ U–Pb zircon geochronology. Chemical Geology, 211, 47-69. https://doi.org/10.1016/j.chemgeo.2004.06.017

Jayananda, M., Gireesh, R. V., Sekhamo, K. U., & Miyazaki, T. (2014). Coeval felsic and Mafic Magmas in neoarchean calc-alkaline magmatic arcs, Dharwar craton, Southern India: Field and petrographic evidence from mafic to Hybrid magmatic enclaves and synplutonic Mafic dykes. Journal of the Geological Society of India, 84, 5-28. https://doi.org/10.1007/s12594-014-0106-2

Juliani, C., Corrêa-Silva, R.H., Monteiro, L.V.S., Bettencourt, J.S., Nunes, C.M.D. (2002). The Batalha Au-granite system – Tapajós Gold Province, Amazonian craton, Brazil: hydrothermal alteration and regional implications. Precambrian Research 119, 225-256. https://doi.org/10.1016/S0301-9268(02)00124-9

Juliani, C., Rodrigues de Assis, R., Virgínia Soares Monteiro, L., Marcello Dias Fernandes, C., Eduardo Zimmermann da Silva Martins, J., & Ricardo Costa e Costa, J. (2021). Gold in Paleoproterozoic (2.1 to 1.77 Ga) continental magmatic arcs at the Tapajós and Juruena Mineral Provinces (Amazonian Craton, Brazil): a new frontier for the exploration of epithermal–porphyry and related deposits. Minerals, 11(7), 714. https://doi.org/10.3390/min11070714

Juliani, C., Rye, R.O., Nunes, C.M.D., Snee, L.W., Corrêa Silva, R.H., Monteiro, L.V.S., Bettencourt, J.S., Neumann, R., Neto, A.A. (2005). Paleoproterozoic high-sulfidation mineralization in the Tapajós gold province, Amazonian Craton, Brazil: geology, mineralogy, alunite argon age, and stable-isotope constraints. Chemical Geology 215, 95-125. https://doi.org/10.1016/j.chemgeo.2004.06.035

Kavalieris, I., Walshe, J. L., Halley, S., & Harrold, B. P. (1990). Dome-related gold mineralization in the Pani volcanic complex, North Sulawesi, Indonesia; a study of geologic relations, fluid inclusions, and chlorite compositions. Economic Geology, 85(6), 1208-1225. https://doi.org/10.2113/gsecongeo.85.6.1208

Kesler, S. E., Chryssoulis, S. L., & Simon, G. (2002). Gold in porphyry copper deposits: its abundance and fate. Ore Geology Reviews, 21(1-2), 103-124. https://doi.org/10.1016/S0169-1368(02)00084-7

Klein, E.L., Almeida, M.E., Vasquez, M.L., Bahia, R.B.C., Quadros, M.L. do E.S., Ferreira, A.L. (2001). PROMIN - Tapajós. Geologia e Recursos Minerais da Província Mineral do Tapajós. Estados do Pará e do Amazonas. Escala 1:500.000. Nota Explicativa. Belém: CPRM, 104 p.

Kranidiotis, P., & MacLean, W. H. (1987). Systematics of chlorite alteration at the Phelps Dodge massive sulfide deposit, Matagami, Quebec. Economic geology, 82(7), 1898-1911. https://doi.org/10.2113/gsecongeo.82.7.1898

Lamarão, C.N., Dall'Agnol, R., Lafon, J.M., Lima, E.F. (2002). Geology, geochemistry, and Pb-Pb zircon geochronology of the Paleoproterozoic magmatism of Vila Riozinho, Tapajós Gold Province, Amazonian craton, Brazil. Precambrian Research, 119:189-223. https://doi.org/10.1016/S0301-9268(02)00123-7

Lang, J., & Baker, T. (2001). Intrusion-related gold systems: the present level of understanding. Mineralium deposita, 36, 477-489. https://doi.org/10.1007/s001260100184

Li, Y., & Audétat, A. (2012). Partitioning of V, Mn, Co, Ni, Cu, Zn, As, Mo, Ag, Sn, Sb, W, Au, Pb, and Bi between sulfide phases and hydrous basanite melt at upper mantle conditions. Earth and Planetary Science Letters, 355, 327-340. https://doi.org/10.1016/j.epsl.2012.08.008

Li, Y., & Audétat, A. (2013). Gold solubility and partitioning between sulfide liquid, monosulfide solid solution and hydrous mantle melts: Implications for the formation of Au-rich magmas and crust–mantle differentiation. Geochimica et Cosmochimica Acta, 118, 247-262. https://doi.org/10.1016/j.gca.2013.05.014

Li, Y., & Audétat, A. (2015). Effects of temperature, silicate melt composition, and oxygen fugacity on the partitioning of V, Mn, Co, Ni, Cu, Zn, As, Mo, Ag, Sn, Sb, W, Au, Pb, and Bi between sulfide phases and silicate melt. Geochimica et Cosmochimica Acta, 162, 25-45. https://doi.org/10.1016/j.gca.2015.04.036

Li, Y., Audétat, A., Liu, Z., & Wang, F. (2021). Chalcophile element partitioning between Cu-rich sulfide phases and silicate melt and implications for the formation of Earth's continental crust. Geochimica et Cosmochimica Acta, 302, 61-82. https://doi.org/10.1016/j.gca.2021.03.020

Lopes, A. A. C., & Moura, M. A. (2019). The Tocantinzinho Paleoproterozoic porphyry-style gold deposit, Tapajós Mineral Province (Brazil): Geology, petrology and fluid inclusion evidence for ore-forming processes. Minerals, 9(1), 29. https://doi.org/10.3390/min9010029

Lugmair, G. W., & Marti, K. (1978). Lunar initial 143Nd/144Nd: differential evolution of the lunar crust and mantle. Earth and Planetary Science Letters, 39(3), 349-357. https://doi.org/10.1016/0012-821X(78)90021-3

Migdisov, A. A., & Williams-Jones, A. E. (2014). Hydrothermal transport and deposition of the rare earth elements by fluorine-bearing aqueous liquids. Mineralium Deposita, 49, 987-997. https://doi.org/10.1007/s00126-014-0554-z

Migdisov, A., Williams-Jones, A. E., Brugger, J., & Caporuscio, F. A. (2016). Hydrothermal transport, deposition, and fractionation of the REE: Experimental data and

thermodynamic calculations. Chemical Geology, 439, 13-42. https://doi.org/10.1016/j.chemgeo.2016.06.005

Miller, C. F., Stoddard, E. F., Bradfish, L. J., & Dollase, W. A. (1981). Composition of plutonic muscovite; genetic implications. The Canadian Mineralogist, 19(1), 25-34.

Moreira, I. C. (2019). Petrogênese dos granitoides do Depósito Paraíba, Peixoto de Azevedo, Província Aurífera de Alta Floresta, Cráton Amazonas. Dissertação de Mestrado, Universidade Estadual de Campinas, Campinas, Brasil, 89 p.

Murakami, H., Seo, J. H., & Heinrich, C. A. (2010). The relation between Cu/Au ratio and formation depth of porphyry-style Cu–Au±Mo deposits. Mineralium Deposita, 45, 11-21. https://doi.org/10.1007/s00126-009-0255-1

Nachit H., Ibhi A., Abia E. H. and Ben Ohod M. (2005). Discrimination between primary magmatic biotites, re-equilibrated biotites and neoformed biotites. Geoscience, 337, 1415-1420. https://doi.org/10.1016/j.crte.2005.09.002

Norman, D. K., Parry, W. T., & Bowman, J. R. (1991). Petrology and geochemistry of propylitic alteration at Southwest Tintic, Utah. Economic Geology, 86(1), 13-28. https://doi.org/10.2113/gsecongeo.86.1.13

Park, J. W., Campbell, I. H., Chiaradia, M., Hao, H., & Lee, C. T. (2021). Crustal magmatic controls on the formation of porphyry copper deposits. Nature Reviews Earth & Environment, 2(8), 542-557. https://doi.org/10.1038/s43017-021-00182-8

Park, J. W., Campbell, I. H., Malaviarachchi, S. P., Cocker, H., Hao, H., & Kay, S. M. (2019). Chalcophile element fertility and the formation of porphyry Cu±Au deposits. Mineralium Deposita, 54, 657-670. https://doi.org/10.1007/s00126-018-0834-0

Paton, C., Hellstrom, J., Paul, B., Woodhead, J., & Hergt, J. (2011). Iolite: Freeware for the visualisation and processing of mass spectrometric data. Journal of Analytical Atomic Spectrometry, 26(12), 2508-2518. https://doi.org/10.1039/C1JA10172B

Pearce, J. A., Harris, N. W. & Tindle, A. G. (1984). Trace element discrimination diagrams for the tectonic interpretation of granitic rocks. Journal of Petrology 25, 956–983. https://doi.org/10.1093/petrology/25.4.956

Pearce, J.A., (1996). Source and settings of granitic rocks. Episodes 19,120–125. https://doi.org/10.18814/epiiugs/1996/v19i4/005

Peccerillo, A. Taylor, S. R. (1976). Geochemistry of Eocene calc-alkaline volcanic rocks from the Kastamonu area, Northern Turkey. Contributions to Mineralogy and Petrology 58, 63–81. https://doi.org/10.1007/BF00384745

Petrus, J. A., & Kamber, B. S. (2012). VizualAge: A novel approach to laser ablation ICP-MS U-Pb geochronology data reduction. Geostandards and Geoanalytical Research, 36(3), 247-270. https://doi.org/10.1111/j.1751-908X.2012.00158.x

Reiners, P. W., Carlson, R. W., Renne, P. R., Cooper, K. M., Granger, D. E., McLean, N. M., & Schoene, B. (2017). The K-Ar and $^{40}Ar/^{39}Ar$ systems, in: Geochronology and thermochronology. John Wiley & Sons, 231-257. DOI:10.1002/9781118455876

Renne, P. R., Balco, G., Ludwig, K. R., Mundil, R., & Min, K. (2011). Response to the comment by WH Schwarz et al. on “Joint determination of 40K decay constants and 40Ar∗/40K for the Fish Canyon sanidine standard, and improved accuracy for 40Ar/39Ar geochronology” by PR Renne et al. (2010). Geochimica et Cosmochimica Acta, 75(17), 5097-5100. doi:10.1016/j.gca.2011.06.021

Roddick, J. C. (1983). High precision intercalibration of ^{40}Ar-^{39}Ar standards. Geochimica et Cosmochimica Acta, 47(5), 887-898. https://doi.org/10.1016/0016-7037(83)90154-0

Rodrigues, R.M., Mascarenhas, A.F.S., Ichihara, A.H., Souza, T.M.C., Bidone, E.D., Bellia, V., Hacon, S., Silva, A.R.B., Braga, J.B.P., Stilianidi Filho, B. 1994. Estudos dos impactos ambientais decorrentes do extrativismo mineral e poluição mercurial no Tapajós: pré-diagnóstico. Rio de Janeiro: CETEM/MCT, Série Tecnologia Ambiental, 04, 119 p.

Rottier, B., Audétat, A., Koděra, P., & Lexa, J. (2020). Magmatic evolution of the mineralized Štiavnica volcano (Central Slovakia): Evidence from thermobarometry, melt inclusions, and sulfide inclusions. Journal of Volcanology and Geothermal Research, 401, 106967. https://doi.org/10.1016/j.jvolgeores.2020.106967

Santos J.O.S., Hartmann L.A., Faria M.S.G., Riker S.R., Souza M.M., Almeida M.E., McNaughton N.J. (2006). A compartimentação do Cráton Amazonas em províncias: avanços ocorridos no período 2000-2006. In: SBG-NO, Simpósio de Geologia da Amazônia, 9, Belém, CD-ROM.

Santos, D.B. dos, Fernandes, P.E.C.A., Dreher, A.M., Cunha, F.M. B.da, Basei, M.A.S., Teixeira, W. 1975. Geologia. Folha SB. 21 Tapajós. *In*: BRASIL. DNPM. Projeto RADAM. Rio de Janeiro, (Levantamentos de Recursos Minerais, 7).

Santos, J.O.S., Breemen, O.B.V., Groves, D.I., Hartmann, L.A., Almeida, M.E., McNaughton, N.J., Fletcher, I.R. (2004). Timing and evolution of multiple Paleoproterozoic magmatic arcs in the Tapajós Domain, Amazon Craton: constraints from SHRIMP and TIMS zircon, baddeleyite and titanite U-Pb geochronology. Precambrian Research 131, 73-109. https://doi.org/10.1016/j.precamres.2004.01.002

Santos, J.O.S., Groves, D.I., Hartmann, L.A., Moura, M.A., McNaughton, N.J. (2001). Gold deposits of the Tapajós and Alta Floresta domains, Tapajós-Parima orogenic belt, Amazon Craton, Brazil. Mineralium Deposita, 36:278-299. https://doi.org/10.1007/s001260100172

Santos, J.O.S., Hartmann, L.A., Gaudette, E,H.E., Groves, D.I., McNaughton, N.J., Fletcher, I.R. (2000). New understanding of the province of the Amazon craton based on integration of field mapping and U-Pb and Sm-Nd geochronology. *Gondwana Research, v. 3, n. 4, 453-488.* https://doi.org/10.1016/S1342-937X(05)70755-3

Santosh, M., & Groves, D. I. (2022). Global metallogeny in relation to secular evolution of the Earth and supercontinent cycles. Gondwana Research, 107, 395-422. https://doi.org/10.1016/j.gr.2022.04.007

Seal, R. R. (2006). Sulfur isotope geochemistry of sulfide minerals. Reviews in mineralogy and geochemistry, 61(1), 633-677. https://doi.org/10.2138/rmg.2006.61.12

Shand, S. J. (1927). On the relations between silica, alumina, and the bases in eruptive rocks, considered as a means of classification. Geological Magazine, 64(10), 446-449. https://doi.org/10.1017/S0016756800103760

Sillitoe, R.H. (2000). Gold-rich porphyry deposits: descriptive and genetic models and their role in exploration and discovery, in: Steffen G Hagemann, Philip E. Brown, Gold in 2000. SEG Reviews, 13, 315-345. https://doi.org/10.5382/Rev.13.09

Sillitoe, R.H. (2010). Porphyry copper systems. Economic Geology, 105(1), 3-41. https://doi.org/10.2113/gsecongeo.105.1.3

Silva Junior, C. A. S.; Klein, E. L.; Galarza, M. A.; Borges, R. M. K.; Queiroz, J. D. S.; Assunção, R. F. S.; Araújo, A. C. S.; Moore, D. J. (2015). Zircon geochronology and Pb isotope systematics in sulfides: implications for the genesis of gold mineralization in the Cuiú-Cuiú Goldfield, Tapajós Gold Province, Amazonian Craton, Brazil. In: Contribuições à Geologia da Amazônia; Gorayaeb, P. S. S., Lima, A. M. M., Eds.; SBG-Núcleo Norte: Belém; 453–465.

Silva, M.L.T. (2017). Geologia, petrologia e metalogenia do depósito de ouro Santa Helena, Mato Grosso. Dissertação de mestrado, Universidade de Brasília, Brasília, Brasil, 115 p.

Simmons, S. F., & Browne, P. R. (1990). Mineralogic, alteration and fluid-inclusion studies of epithermal gold-bearing veins at the Mt. Muro Prospect, Central Kalimantan (Borneo), Indonesia. Journal of Geochemical Exploration, 35(1-3), 63-103. https://doi.org/10.1016/0375-6742(90)90036-A

Sláma, J., Košler, J., Condon, D. J., Crowley, J. L., Gerdes, A., Hanchar, J. M., Horstwoord, M. S. A., Morris, G. A., Nasdala, L., Norberg, N., Schaltegger, U., Schoene, B., Tubrett, M. N., & Whitehouse, M. J. (2008). Plešovice zircon—a new natural reference material for U–Pb and Hf isotopic microanalysis. Chemical Geology, 249(1-2), 1-35. https://doi.org/10.1016/j.chemgeo.2007.11.005

Stefánsson, A., & Seward, T. M. (2004). Gold (I) complexing in aqueous sulphide solutions to 500 C at 500 bar. Geochimica et Cosmochimica Acta, 68(20), 4121-4143. https://doi.org/10.1016/j.gca.2004.04.006

Sun, S.S., McDonough, W.F. (1989). Chemical and isotopic systematics of oceanic basalts: implications for mantle compositions and processes. In: Saunders, A.D., Norry, M.J. (Eds.), Magmatism in Ocean Basins, vol. 42. Geological Society of London, 313–345, Special Pub. https://doi.org/10.1144/GSL.SP.1989.042.01.19

Sylvester, P. J. (1998). Post-collisional strongly peraluminous granites. Lithos, 45(1-4), 29-44. https://doi.org/10.1016/S0024-4937(98)00024-3

Tassinari, C. C. G., Macambira, M. J. B. 2004. A evolução tectônica do Cráton Amazônico. *In*: Geologia do continente sul-americano: evolução da obra de Fernando Flávio Marques de Almeida. São Paulo: Beca, p. 471-485.

Tassinari, C. C., & Macambira, M. J. (1999). Geochronological provinces of the Amazonian Craton. Episodes Journal of International Geoscience, 22(3), 174-182. https://doi.org/10.18814/epiiugs/1999/v22i3/004

Thompson, J. F. H., Sillitoe, R. H., Baker, T., Lang, J. R., & Mortensen, J. K. (1999). Intrusion-related gold deposits associated with tungsten-tin provinces. Mineralium Deposita, 34, 323-334. https://doi.org/10.1007/s001260050207

Tischendorf, G., Förster, H.J., Gottesmann, B., Rieder, M. (2007). True and brittle micas: composition and solid-solution series. Mineralogical Magazine, 71(3), 285-320. https://doi.org/10.1180/minmag.2007.071.3.285

Turner, G., Huneke, J. C., Podosek, F. A., & Wasserburg, G. J. (1971). ^{40}Ar-^{39}Ar ages and cosmic ray exposure ages of Apollo 14 samples. Earth and Planetary Science Letters, 12(1), 19-35. https://doi.org/10.1016/0012-821X(71)90051-3

Vermeesch, P. (2018). IsoplotR: A free and open toolbox for geochronology. Geoscience Frontiers, 9(5), 1479-1493. https://doi.org/10.1016/j.gsf.2018.04.001

Vernon, R. H., & Paterson, S. R. (2006). Mesoscopic structures resulting from crystal accumulation and melt movement in granites. Earth and Environmental Science Transactions of the Royal Society of Edinburgh, 97(4), 369-381. https://doi.org/10.1017/S0263593300001516

Villas, R. N. N., Santiago, É. S. B., & Castilho, M. P. (2013). Contexto geológico, estudos isotópicos (C, O e Pb) e associação metálica do depósito aurífero Tocantinzinho, domínio Tapajós, Província Tapajós-Parima.

Weinberg, R. F., Vernon, R. H., & Schmeling, H. (2021). Processes in mushes and their role in the differentiation of granitic rocks. Earth-Science Reviews, 220, 103665. https://doi.org/10.1016/j.earscirev.2021.103665

Whitney, D. L., & Evans, B. W. (2010). Abbreviations for names of rock-forming minerals. American mineralogist, 95(1), 185-187. https://doi.org/10.2138/am.2010.3371

Wiedenbeck, M. A. P. C., Alle, P., Corfu, F. Y., Griffin, W. L., Meier, M., Oberli, F. V., Von Quadt, A., Roddick, J. C., & Spiegel, W. (1995). Three natural zircon standards for U-Th-Pb, Lu-Hf, trace element and REE analyses. Geostandards newsletter, 19(1), 1-23. https://doi.org/10.1111/j.1751-908X.1995.tb00147.x

Wiewióra, A., & Weiss, Z. (1990). Crystallochemical classifications of phyllosilicates based on the unified system of projection of chemical composition: II. The chlorite group. Clay Minerals, 25(1), 83-92. https://doi.org/10.1180/claymin.1990.025.1.09

Williams-Jones, A. E., Bowell, R. J., & Migdisov, A. A. (2009). Gold in solution. Elements, 5(5), 281-287. https://doi.org/10.2113/gselements.5.5.281

Wones, D. R., & Eugster, H. P. (1965). Stability of biotite: experiment, theory, and application. The American Mineralogist, 50, 1228-1272.

Wood, S. A. (1990). The aqueous geochemistry of the rare-earth elements and yttrium: 2. Theoretical predictions of speciation in hydrothermal solutions to 350 C at saturation water vapor pressure. Chemical Geology, 88(1-2), 99-125. https://doi.org/10.1016/0009-2541(90)90106-H

Yavuz, F., Kumral, M., Karakaya, N., Karakaya, M. Ç., & Yıldırım, D. K. (2015). A Windows program for chlorite calculation and classification. Computers & Geosciences, 81, 101-113. https://doi.org/10.1016/j.cageo.2015.04.011

Zane, A., & Weiss, Z. (1998). A procedure for classifying rock-forming chlorites based on microprobe data; Una procedura per la classificazione delle cloriti sulla base di dati microchimici. Atti della Accademia Nazionale dei Lincei. Rendiconti. Scienze Fisiche e Naturali, 9, 51-56.

Zang, W., & Fyfe, W. S. (1995). Chloritization of the hydrothermally altered bedrock at the Igarapé Bahia gold deposit, Carajás, Brazil. Mineralium Deposita, 30, 30-38. https://doi.org/10.1007/BF00208874

Zhang, D., & Audétat, A. (2017). What caused the formation of the giant Bingham Canyon porphyry Cu-Mo-Au deposit? Insights from melt inclusions and magmatic sulfides. Economic Geology, 112(2), 221-244. https://doi.org/10.2113/econgeo.112.2.221